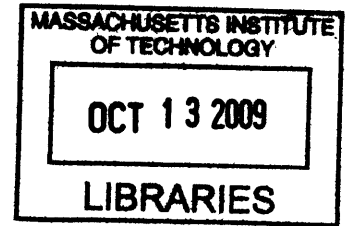# Emission of Whistler Waves from an Ionospheric Tether

by

Yu Takiguchi

Bachelor of Engineering
The University of Tokyo, 2006

Submitted to the Department of Aeronautics and Astronautics
in partial fulfillment of the requirements for the degree of

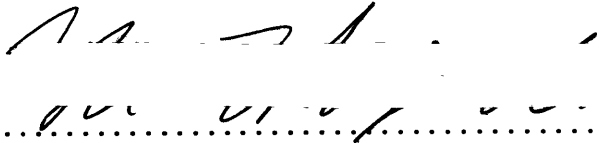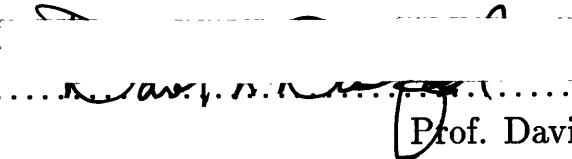Master of Science in Aeronautics and Astronautics

at the

MASSACHUSETTS INSTITUTE OF TECHNOLOGY

September 2009

Author..
Department of Aeronautics and Astronautics
August 19, 2009

Certified by..
Prof. Manuel Martínez-Sánchez
Professor
Thesis Supervisor

Accepted by..
Prof. David L. Darmofal
Associate Department Head
Chair, Committee on Graduate Students

Emission of Whistler Waves from an Ionospheric Tether

by

Yu Takiguchi

Submitted to the Department of Aeronautics and Astronautics
on August 19, 2009, in partial fulfillment of the
requirements for the degree of
Master of Science in Aeronautics and Astronautics

Abstract

In this thesis, we analyze how electromagnetic waves propagate in ionosphere around the earth which is magnetized plasma. We calculate the electromagnetic wave field made by a dipole antenna at an arbitrary observation point far from the antenna using the Stationary Phase Method. With this wave field, wave energy flux is calculated, and by integrating this wave energy flux on the sphere around the antenna, the radiation resistance of this antenna is computed. We compare the results with some past analytical and experimental works. We also analyze the wave propagation characteristics. The wave propagation ways are different for different wave frequencies. We precisely analyze this different wave propagation ways by analyzing the group velocity and $\vec{k}$ surface of the wave. There are intense radiation directions. We discuss the nature of these intense radiation directions and compare the characteristics with the past works. There are spatial oscillations of wave fields and wave energy flux. We also discuss the reason of this oscillation and compare with the past works.

Thesis Supervisor: Prof. Manuel Martínez-Sánchez
Title: Professor

Acknowledgments

I would like to sincerely thank my advisor Professor Manuel Martínez-Sánchez for giving me this amazing chance to work on this research and helpful guidance throughout three years. Without his support, I could not complete this thesis. He gave me a lot of great advises and suggestions.

I would also like to thank Prof. Paulo Lozano and Dr. Oleg Batishchev for suggestions and insights which helped me a lot. I enjoyed talking with Oleg. We both love cameras.

I'm very lucky to have great office mates. Members in SPL helped me a lot academically and as friends. I enjoy the life at MIT and even the office without a window because of everyone in SPL.

My life in Boston/Cambridge was very exciting because of Wasabis. We played music, ate and drank together and talked through the night. It was so fun, and I matured as a person through the discussions with the members of Wasabis. Japanese Association of MIT and other Japanese friends made my life interesting. I never forget this wonderful life in Boston.

I could continue my study at MIT because of the support of my family. I thank my Father, Mother and my sister Ryoko and the other relatives. They have always encouraged me over the past three years.

Finally, I would like to thank my fiancée Sayaka Moue. She always supports and encourages me. My life in Boston is very comfortable because of her help. There is no other person who can give me so much happiness.

Contents

List of Figures

13

List of Tables

Chapter 1

Introduction

1.1 The Van Allen Radiation Belt

The region of the space between about 700km to 10,000km altitude is called the inner belt of the Van Allen radiation belts. In the Van Allen radiation belts, many high-energy electrons and ions are trapped by the magnetic field of the earth. High-energy electrons and ions gyrate around the magnetic field of the earth and move back and forth in its magnetic bottle. The smaller the angle of the particle velocity with to earth magnetic field, the farther can the particle go along the magnetic field line. These high-energy particles are mainly from the sun, but also a high altitude nuclear explosion can be a source of these particles[3]. Some of the trapped particles enter the loss cone by being scattered by a variety of natural mechanisms, such as Coulomb collisions, Cerenkov radiation from cosmic ray particles, and, most significantly, the interaction with a family of low frequency plasma waves, called Whistler waves, and escape from the earth magnetic field. Those escaping particles penetrate low enough and lose their energy through collisions with the upper atmosphere. Whistler waves are produced in nature by the magnetoplasma instabilities and by lightning strikes around the world[4, 5].

1.2 Motivations for Radiation Belt Remediation

Radiation from these high-energy particles is harmful for devices in artificial satellites[6, 7]. For example, the Hubble Space Telescope must turn off its sensors when passing through intense radiation to maintain reliable operation[8]. This radiation would be an obstacle to the use of electric propulsion to raise the orbit of satellites, because the satellites would be in the intense radiation zone for a long time. Radiation is also harmful for humans in that area. For these reasons, we need these high-energy electrons and ions to be decreased in order to use artificial satellites and for humans to travel in that area. It has been suggested that Whistler waves can be injected artificially into the magnetosphere by antennas on the ground or in space, and the artificially injected Whistler waves could strongly contribute to the loss of high-energy particles. This particle cleaning method is the leading candidate for the so-called Radiation Belt Remediation. The mechanism of Radiation Belt Remediation is as follows.

1. Emit low frequency waves (Whistler wave) from an antenna

2. The wave changes the velocity direction of high-energy particles

3. Some high-energy particles go into the loss cone and can escape from the earth magnetic field

4. These particles penetrate to the upper atmosphere and lose their energy

1.3 Whistler Wave

The Whistler wave is one kind of low frequency electromagnetic wave propagating in a magnetized plasma. The frequency of Whistler wave is below the electron cyclotron frequency of the plasma, but above the lower hybrid frequency. Whistler waves have the property that they propagate strongly along the magnetic field, so if this wave is injected to the magnetosphere by a lightning somewhere on the earth, it mainly
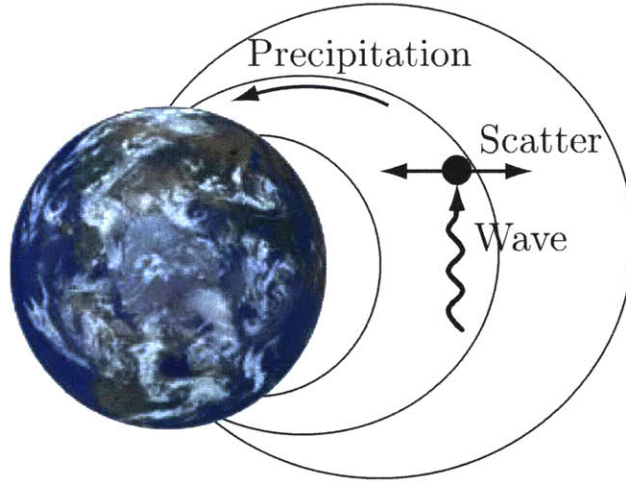
Figure 1-1: Mechanism of Radiation Belt Remediation

propagates along the magnetic field and reaches the magnetic conjugate point on the earth.

To change the velocity of high-energy electrons efficiently, the frequency of the electromagnetic wave should be near to electron cyclotron frequency for the component of $\vec{B}$ along the wave propagation direction. Also, the field of the electromagnetic wave should rotate in the same sense as the electron gyration to produce a resonance and scatter electrons efficiently. However, a right-handed polarized wave whose field rotates in the same sense as the electron gyration does not propagate in the magnetized plasma if the frequency is higher than the electron cyclotron frequency. For these reasons, Whistler waves should be used in Radiation Belt Remediation.

1.4 On-ground Antenna and Spaceborne Antenna

Some experiments of Radiation Belt Remediation using ELF/VLF high power antennas all over the world have been reported in the last few years[9, 10, 11]. They have shown that the Whistler waves injected into the magnetic field from the antennas on the ground contribute to the loss of high-energy particles. However, in order to use on-the-ground antennas for Radiation Belt Remediation huge power levels are necessary, because about 95% of the low frequency wave is reflected by the ionosphere when

injecting a wave to the magnetosphere from the ground. If we use a spaceborne antenna, we need less power to emit Whistler wave into the magnetosphere. Therefore, we choose investigate the direct way, Radiation Belt Remediation with a spaceborne antenna. Given the very long wavelength involved, magnetic dipole antennas are difficult to implement, so a linear dipole antenna is a logical choice. Beyond some 100m in length, rigid antenna structures become unfeasible, so we postulate the use of very long flexible cables (orbiting tethers), with length from 1 to 10km or more. If the lower frequency EMIC band were targeted in order to scatter ions, the length would be even more, to perhaps 100km.

1.5   Wave Propagation Analysis and Wave-Particle Interaction Analysis

The analysis of the Radiation Belt Remediation using a spaceborne antenna can be divided into two parts. One is the analysis of wave propagation in the magnetized ambient plasma from an antenna. There are many high-energy particles in the radiation belt, but there are many more low-energy particles there. When considering the wave propagation in the magnetosphere from an antenna, the analysis needs to consider propagation in the low-energy magnetized plasma. The other element is the analysis of wave-particle interaction. Using wave propagation analysis, the wave field and energy from an antenna in the magnetosphere can be calculated. From these values, the pitch-angle diffusion rate of high-energy particles by the electromagnetic wave can be estimated. Some previous works have presented the diffusion rate by assuming the wave field intensity from an antenna [12, 13, 1].

Much work on wave propagation calculation has been done previously. In this earlier work, the spatially averaged radiation pattern has been calculated. However, more detailed analysis can be done. For example, calculating electric and magnetic field with analysis using the stationary phase method, more detailed spatial property of the wave field can be obtained. Most previous work avoids the Poynting's vector

calculation in favor of a direct calculation of the radiated power via Parseval's theorem. This thesis is a preliminary research for Radiaition Belt Remediation, and we aim to develop a flexible and usable tool to analyze wave propagation in the magnetosphere for broader study in the future. For example, this basic analysis is useful to compare with the results of more advanced model calculations involving nonlinearities and inhomogeneities to see whether the physics is correct or not.

This analysis can also be used to estimate the particle diffusion with wave-particle interaction analysis. This thesis presents the detailed analysis on wave propagation in magnetospheric plasma with a simple model.

1.6   Thesis Outline

This thesis presents analyses about low frequency electromagnetic wave propagation in magnetized plasma from an antenna in space. Chapter 2 gives the explanation of the calculation method used in this research. The stationary phase method which is used in this calculation, and analysis about group velocity of the electromagnetic wave are discussed in chapter 3. The wave radiation pattern from the antenna in magnetospheric plasma has an interesting shape. There are some intense radiation cones around the antenna. The analysis about this intense radiation cones is discussed in chapter 4. Chapter 5 shows the results and comparison with previous works. Chapter 6 concludes this research and suggests some possible future works.

Chapter 2

Calculation Method

2.1 Equations

The propagation of an electromagnetic wave in plasma is formulated by application of Maxwell's equations and the equations of motion of the particles. In our problem, we use Maxwell's equations and the electron equation of motion. We neglect the ion motion because the frequencies of interest are above the lower hybrid frequency. Maxwell's equations (neglecting displacement current):

$$\nabla \times \vec{E}_{(\vec{r})} = -\frac{\partial \vec{B}_{(\vec{r})}}{\partial t} \tag{2.1}$$

$$\nabla \times \vec{B}_{(\vec{r})} = \mu_0 \vec{j}_{(\vec{r})} = \mu_0 \left(\vec{j}_s - e n_e \vec{v_e} \right) \tag{2.2}$$

where $\vec{j}_s$ is the current iin the antenna wire, shile $-e n_e \vec{v_e}$ is the current due to the motion of electrons. Linearized electron equation of motion:

$$m_e \frac{\partial \vec{v_e}}{\partial t} = -e(\vec{E}_{(\vec{r})} + \vec{v_e} \times \vec{B}_{0(\vec{r})}) - m_e \nu_e \vec{v_e} \quad (\ \nu_e : \text{collision frequency}) \tag{2.3}$$

From Eq.(2.1) andEq.(2.2),

$$\nabla^2 \vec{E}_{(\vec{r})} - \nabla(\nabla \cdot \vec{E}_{(\vec{r})}) = -\mu_0 e n_{e0} \frac{\partial \vec{v_e}}{\partial t} + \mu_0 \frac{\partial \vec{j}_s}{\partial t} \tag{2.4}$$

2.2 Fourier Transformation

We can solve those equations using Fourier transformation. In this problem, we analyse the wave propagation with fixed frequency ω.

One of the space-time Fourier components can be expressed as

$$\vec{E}_{(\vec{r})} = \vec{E}_{(\omega,\vec{k})} \exp i(\omega t - \vec{k} \cdot \vec{x}) \tag{2.5}$$

From Eq.(2.4),

$$-k^2\vec{E} + \vec{k}(\vec{k} \cdot \vec{E}) = -i\mu_0 e n_{e0}\omega\vec{v}_e + i\mu_0\omega\vec{j}_s \tag{2.6}$$

From Eq.(2.3),

$$m_e(i\omega + \nu_e)\vec{v}_e = -e(\vec{E} + \vec{v}_e \times \vec{B}_0) \tag{2.7}$$

Then, from Eq.(2.6) and Eq.(2.7),

$$\vec{E}\left[1 - \frac{ik^2}{\mu_0\omega}\frac{m_e(i\omega + \nu_e)}{e^2 n_{e0}}\right] - \frac{ik^2}{\mu_0 n_{e0}\omega e}\vec{E} \times \vec{B}_0 + (\vec{k} \cdot \vec{E})i\left[\frac{\vec{k}}{\mu_0\omega}\frac{m_e(i\omega + \nu_e)}{e^2 n_{e0}} + \frac{\vec{k} \times \vec{B}_0}{\mu_0 e n_{e0}\omega}\right]$$
$$= \frac{-m_e(i\omega + \nu_e)}{e^2 n_{e0}}\vec{j}_s - \frac{\vec{j}_s \times \vec{B}_0}{e n_{e0}} \tag{2.8}$$

Define

$$\vec{b}_0 = \vec{B}_0/B_0 \tag{2.9}$$

$$\delta = \frac{\nu_e}{\omega_{ce}} \tag{2.10}$$

$$\nu = \frac{\omega}{\omega_{ce}} \tag{2.11}$$

$$l = \sqrt{\frac{m_e}{e^2 n_{e0}\mu_0}} \tag{2.12}$$

$$K = kl \tag{2.13}$$

$$\sigma_{ce} = \frac{e^2 n_{e0}}{m_e\omega_{ce}} \tag{2.14}$$

Assuming that $B_0 = 10^{-5}$ Tesla and electron temperature is 1 eV, the plasma skin depth l,σ_{ce} and δ for $n = 10^{10}$ [/m^3] and $n = 10^8$ [/m^3] are estimated as shown in

Table 2.2. ($\omega_{ce} \sim 1.7 \times 10^6$ [rad/sec])

Table 2.1: Estimated l, σ_{ce} and δ

n [/m^3]	l [m]	σ_{ce} [Si/m]	δ
10^{10}	50	1.6×10^{-4}	4×10^{-8}
10^8	500	1.6×10^{-6}	4×10^{-10}

Then,Eq.(2.8) becomes

$$\vec{E}\left(1 + K^2 - i\frac{K^2\delta}{\nu}\right) - i\frac{K^2}{\nu}\vec{E} \times \vec{b_0} + \left(\vec{K} \cdot \vec{E}\right)\left(-\vec{K} + i\frac{\vec{K} \times \vec{b_0}}{\nu} + i\frac{\delta}{\nu}\vec{K}\right)$$

$$= -\frac{(i\nu + \delta)\vec{j_s} + \vec{j_s} \times \vec{b_0}}{\sigma_{ce}} \tag{2.15}$$

The configuration is such that $\vec{k}$ is along the x-axis,and $\vec{B_0}$ makes an angle θ to $\vec{k}$ and is in the x-y plane (Fig.(2-1)).
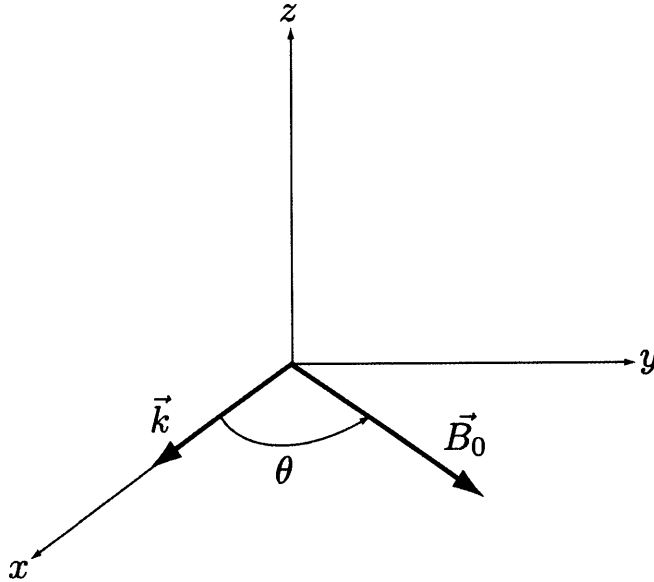
Figure 2-1: $\vec{k}$ and $\vec{B_0}$ configuration

25

Then,

$$\vec{b_0} = \cos\theta\hat{x} + \sin\theta\hat{y}$$

$$\vec{E} \times \vec{b_0} = -\sin\theta\hat{E}_z\hat{x} + \cos\theta\hat{E}_z\hat{y} + \left(\sin\theta\hat{E}_x - \cos\theta\hat{E}_y\right)\hat{z}$$

$$\vec{K} \times \vec{b_0} = K\sin\theta\hat{z}$$

$$\vec{j_s} = -\sin\theta\hat{j}_{sz}\hat{x} + \cos\theta\hat{j}_{sz}\hat{y} + \left(\sin\theta\hat{j}_{sx} - \cos\theta\hat{j}_{sy}\right)$$

$(\hat{x}, \hat{y}, \hat{z}$: unit vectors on x, y, z axes)

Thus, Eq.(2.15) becomes the system

$$\hat{E}_x + i\frac{K^2}{\nu}\sin\theta\hat{E}_z = -\frac{(i\nu + \delta)\hat{j}_{sx} - \sin\theta\hat{j}_{sz}}{\sigma_{ce}} \qquad (2.16)$$

$$\left(1 + K^2 - i\frac{K^2\delta}{\nu}\right)\hat{E}_y - i\frac{K^2}{\nu}\cos\theta\hat{E}_z = -\frac{(i\nu + \delta)\hat{j}_{sy} - \cos\theta\hat{j}_{sz}}{\sigma_{ce}} \qquad (2.17)$$

$$i\frac{K^2}{\nu}\cos\theta\hat{E}_y + \left(1 + K^2 - i\frac{K^2\delta}{\nu}\right)\hat{E}_z = -\frac{(i\nu + \delta)\hat{j}_{sz} + \sin\theta\hat{j}_{sx} - \cos\theta\hat{j}_{sy}}{\sigma_{ce}} \qquad (2.18)$$

$\hat{E}_y$ and $\hat{E}_z$ are decoupled from $\hat{E}_x$ (along $\vec{k}$), but $\hat{E}_x$ is tied to $\hat{E}_z$ by Eq.(2.16). For the medium to support free oscillation (i.e., with no source, hence a homogenous set of equations) the determinant of Eq.(2.16), Eq.(2.17) and Eq.(2.18) must be zero.

2.3   Dispersion relation

The determinant of Eq.(2.16),(2.17),(2.18) is same as the determinant of Eq.(2.17),(2.18). For a valid $\hat{E}_x, \hat{E}_y, \hat{E}_z$, we need this determinant to be zero.

$$\left(1 + K^2 - i\frac{K^2\delta}{\nu}\right)^2 - \frac{K^4}{\nu^2}\cos^2\theta = 0 \qquad (2.19)$$

And the roots are

$$K_u = \pm\sqrt{\frac{\nu}{\cos\theta - \nu + i\delta}} \qquad (2.20)$$

$$K_d = \pm i \sqrt{\frac{\nu}{\cos\theta + \nu - i\delta}} = \pm \sqrt{\frac{\nu}{\cos(\pi - \theta) - \nu + i\delta}} \tag{2.21}$$

These are the dispersion relations. As in Fig.(2-2), for $\theta < \cos^{-1}\nu$, K_u represents slightly damped waves, and K_d represents heavily damped waves. For $\cos^{-1}\nu < \theta < \pi - \cos^{-1}\nu$, K_u and K_d represent heavily damped waves. For $\theta > \pi - \cos^{-1}\nu$, K_u represents heavily damped waves, and K_d represents slightly damped waves. So, the K_u wave propagates when $\theta < \cos^{-1}\nu$, and the K_d wave propagates when $\theta > \pi - \cos^{-1}\nu$.
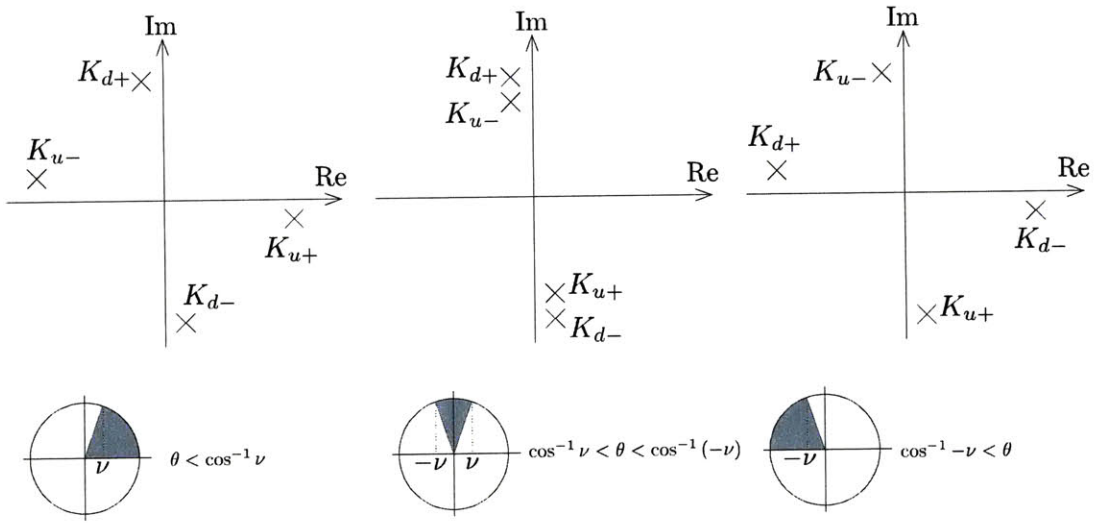
Figure 2-2: K_u and K_d pole position

2.3.1 Wave Polarization

For a free wave $\left(\vec{l}_s = 0\right)$, with no collisions ($\delta = 0$), the dispersion relation Eq.(2.20) gives

$$K^2 = \frac{\nu}{\cos\theta - \nu} \tag{2.22}$$

and then both Eq.(2.17) and Eq.(2.18) reduce to

$$\hat{E}_y = i\hat{E}_z \tag{2.23}$$

27

while Eq.(2.16) reduce to

$$\hat{E}_x = -i\frac{\sin\theta}{\cos\theta - \nu}\hat{E}_y \qquad (2.24)$$

The relation in Eq.(2.23) means that the $\vec{E}$ vector projection on the y-z plane (perpendicular to $\vec{K}$) rotates with constant magnitude about $\vec{K}$. It can be verified that this rotation, at angular velocity ω, is in the Right-hand sense, the same as the gyrorotation of an electron under the influence of the projection of $\vec{B}_0$ on $\vec{K}$. The relationship in Eq.(2.24) then implies that both $|\hat{E}_y|$ and $|\hat{E}_z|$ become much smaller than $|\hat{E}_x|$ when $\cos\theta \rightarrow \nu$, while at the same time, from Eq.(2.20), $K \rightarrow \infty$. Thus, at this Resonance condition, the vector $\vec{E}$ is along $\vec{K}$, which implies $\vec{K} \times \vec{E} = 0$, or $\vec{B} = 0$. The wave approaches in this limit a purely electrostatic wave, with only a longitudinal electric field, and no magnetic field.

For any other allowed direction of propagation ($\cos\theta > 0$), the wave is of a mixed nature, with an Electromagnetic component (the rotating (E_y, E_z) set, with its associated (B_y, B_z), as in a natural EM wave), plus a longitudinal $\vec{E}_x$ oscillation.

Notice finally that the Resonance condition $\cos\theta = \nu$ implies

$$\omega_{ce}\cos\theta = \omega \qquad (2.25)$$

or

$$\omega = \frac{eB_0\cos\theta}{m_e} \qquad (2.26)$$

This means the wave frequency is then the same as the gyrofrequency of electrons under the projection $B_0\cos\theta$ of $\vec{B}_0$ on $\vec{K}$; since, as we saw, the sense of the rotation of (E_y, E_z) about $\vec{K}$ is the same as the sense of the gyromotion, a mechanical resonance occurs, and the wave pumps energy into the electron gyration.

28

2.4 Matrix form of Ohm's law

Eq.(2.16),(2.17),(2.18) can be solved for the wave's electric field as follows

$$\vec{E} = \begin{bmatrix} \hat{E}_x \\ \hat{E}_y \\ \hat{E}_z \end{bmatrix} = Z\vec{\hat{j}}_s = Z \begin{bmatrix} \hat{j}_{sx} \\ \hat{j}_{sy} \\ \hat{j}_{sz} \end{bmatrix} \tag{2.27}$$

$$Z = -\frac{1}{\sigma_{ce}\Delta} \begin{bmatrix} i\nu\left(1+K^2\right)^2 - i\frac{K^2}{\nu}\left(K^2 + \sin^2\theta\right) & i\frac{K^2}{\nu}\sin\theta\cos\theta & -\left(1+K^2\right)\sin\theta \\ i\frac{K^2}{\nu}\sin\theta\cos\theta & i\nu\left(1+K^2\right) - i\frac{K^2}{\nu}\left(\cos^2\theta\right) & \cos\theta \\ \left(1+K^2\right)\sin\theta & -\cos\theta & i\nu\left(1+K^2\right) - i\frac{K^2}{\nu}\left(\cos^2\theta\right) \end{bmatrix} \tag{2.28}$$

$$\Delta = \left(1 + K^2 - i\frac{K^2\delta}{\nu}\right)^2 - \frac{K^4}{\nu^2}\cos^2\theta \tag{2.29}$$

2.5 Antenna related axes

For the computation of the inverse Fourier transformation, we will need to vary $\vec{k}$ in all possible ways. Thus, it is better to change the coordinates to ones which do not change in the inverse Fourier transformation process. Now, $\vec{k}$ is on the x-axis. We will change the coordinates by defining axes(X_B, Y_B, Z_B) such that $\vec{B}_0$ is on the z-axis (B-frame) as in Fig.(2-3). The antenna is in the $X_B - Z_B$ plane and has an angle α to $\vec{B}_0$. $\vec{k}$ is oriented according to the polar angles (θ, ϕ).

Any vector can be expressed in the old coordinates $\vec{V} = (V_x, V_y, V_z)$ and in the new coordinates $\vec{V}_B = (V_{xB}, V_{yB}, V_{zB})$ and the two representations are related as

$$\vec{V}_B = R\vec{V} \tag{2.30}$$

29

R is a rotation matrix and has components as follows

$$R = \begin{bmatrix} \sin\theta\cos\phi & -\cos\theta\cos\phi & \sin\phi \\ \sin\theta\sin\phi & -\cos\theta\sin\phi & -\cos\phi \\ \cos\theta & \sin\theta & 0 \end{bmatrix} \tag{2.31}$$

$R^{-1} = R^T$, so $\vec{V} = R^T\vec{V_B}$.
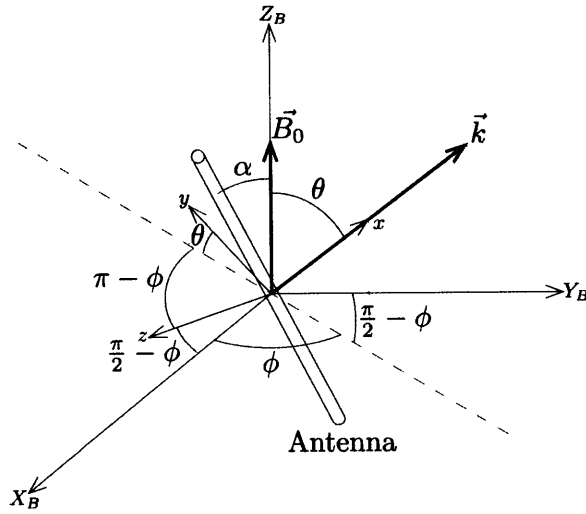
Figure 2-3: Antenna Related Axes

From Eq.(2.27), the current to field relationship is $\vec{E} = Z\vec{j_s}$. Transforming to the B-frame gives

$$RZ\vec{j_s} = R\vec{E} = \vec{E_B} = Z_B\vec{j_{sB}} = Z_B R\vec{j_s} \tag{2.32}$$

and, therefore

$$Z_B = RZR^T \tag{2.33}$$

30

Explicitly, Z_B has components as follows

$$Z_B = -\frac{1}{\sigma_{ce}\Delta} \begin{bmatrix} -p + K^2 \sin^2\theta \left(-p\cos^2\phi + \frac{i}{\nu}\sin^2\phi\right) \\ -\left(1 + K^2\sin^2\theta\right) - iK^2\left(1 + K^2\right)\left(\frac{1}{\nu} - \nu\right)\sin^2\theta\sin\phi\cos\phi \\ -K^2\left(p\cos\phi + \sin\phi\right)\sin\theta\cos\theta \\[1em] -\left(1 + K^2\sin^2\theta\right) - iK^2\left(1 + K^2\right)\left(\frac{1}{\nu} - \nu\right)\sin^2\theta\sin\phi\cos\phi \\ -\left(p - i\frac{K^2}{\nu}\sin^2\theta\right)\cos^2\phi - p\left(1 + K^2\sin^2\theta\right)\sin^2\phi \\ K^2\left(-p\sin\phi + \cos\phi\right)\sin\theta\cos\theta \\[1em] K^2\sin\theta\cos\theta\left(\sin\phi - p\cos\phi\right) \\ -K^2\sin\theta\cos\theta\left(p\sin\phi + \cos\phi\right) \\ -pK^2\cos^2\theta + i\nu\left(1 + K^2\right) \end{bmatrix} \tag{2.34}$$

where

$$p = i\frac{K^2}{\nu} - i\nu\left(1 + K^2\right) \tag{2.35}$$

2.6 The antenna model

For an antenna source current distribution $\vec{j}_s(\vec{x})$, the Fourier transformation is

$$\vec{J}_s(\vec{x}) = \frac{1}{(2\pi)^3} \int\int\int \vec{j}_s(\vec{x})e^{i\vec{k}\cdot\vec{x}}d^3x \tag{2.36}$$

and,

$$\vec{j}_s(\vec{x}) = \begin{cases} \frac{I_s(z_a)}{\pi a^2}\vec{1a} & \text{inside wire} \\ 0 & \text{outside wire} \end{cases} \tag{2.37}$$

a is the radius of the antenna, $\vec{1a}$ is the unit vector along the antenna, I_s is the current, z_a is distance along the antenna. So, if I_0 is $I_s\left(z_a = 0\right)$, Eq.(2.36) becomes

$$\vec{j}_s(\vec{x}) = \frac{1}{(2\pi)^3}\frac{I_0}{\pi a^2}\vec{1a} \int\int\int_{\text{antenna}} \frac{I_s\left(z_a\right)}{I_0}e^{i\vec{k}\cdot\vec{x}}d^3x \tag{2.38}$$

Let $\vec{k_\perp}$ be the projection of $\vec{k}$ on the plane perpendicular to the antenna, and $\vec{k_\parallel}$ be the projection of $\vec{k}$ on the antenna. Then if $\vec{k_\perp}$ makes an angle χ to the x_a axis (which

31
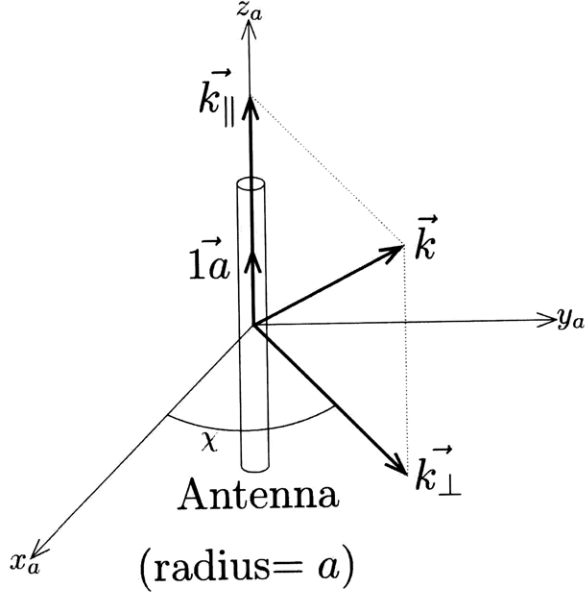
Figure 2-4: Antenna and $\vec{k}$

is on the $X_B Y_B$ plane), and $\vec{x}$ has cylindrical components (R, ψ, z_a) in (x_a, y_a, z_a),

$$\vec{k} \cdot \vec{x} = k_\perp R \cos\left(\psi - \chi\right) + k_{\parallel} z_a \tag{2.39}$$

The integration volume element is $d^3 x = R \, dR \, d\psi \, dz_a$. Using Bessel functions

$$J_{n(x)} = \frac{1}{2\pi} \int_{-\pi}^{\pi} e^{ix \sin\theta - in\theta} \, d\theta \tag{2.40}$$

, the integral on ψ is

$$\int_0^{2\pi} e^{ik_\perp R \cos(\psi - \chi)} \, d\psi = 2\pi J_0\left(k_\perp R\right) \tag{2.41}$$

and the integral on R is,

$$\int_0^a 2\pi J_0\left(k_\perp R\right) R \, dR = \frac{2\pi}{k_\perp^2} \left(a k_\perp\right) J_1(a k_\perp) \tag{2.42}$$

32

Then, we can get

$$\vec{j_s}\left(\vec{k}\right) = \frac{1}{(2\pi)^3}\frac{I_0}{\pi a^2}\vec{1a}\frac{2\pi a}{k_\perp}J_1(ak_\perp)\int_{-L/2}^{L/2}\frac{I_s(z_a)}{I_0}e^{ik_{||}z_a}dz_a \qquad (2.43)$$

Integrate by parts and assume $I_s(z_a = \pm L/2) = 0$, and $I_{s(z_a)} = I_{s(-z_a)}$

$$\int_{-L/2}^{L/2}\frac{I_s(z_a)}{I_0}e^{ik_{||}z_a}dz_a = -\frac{2}{k_{||}}\int_0^{L/2}\sin\left(k_{||}z_a\right)\frac{d}{dz_a}\left(\frac{I_s}{I_0}\right)dz_a \qquad (2.44)$$

We next assume a triangular current distribution for $I_s(z_a)$:

$$\frac{I_s}{I_0} = 1 - \frac{2|z_a|}{L} \qquad (2.45)$$

T.F. Bell, U. S. Inan and T. Chevalier showed that the antenna current distribution in magnetized plasma can be approximated by a triangular current distribution if the antenna is short compared to c/ω_0 where ω_0 is the local angular plasma frequency.[14] Then,

$$\int_{-L/2}^{L/2}\frac{I_s(z_a)}{I_0}e^{ik_{||}z_a}dz_a = \frac{4}{k_{||}^2 L}\left(1 - \cos\left(k_{||}\frac{L}{2}\right)\right) \qquad (2.46)$$

Substituting this in Eq.(2.43),

$$\vec{j_s}\left(\vec{k}\right) = \frac{8aI_0J_1(ak_\perp)}{(2\pi)^3 La^2 k_\perp k_{||}^2}\left(1 - \cos\left(k_{||}\frac{L}{2}\right)\right)\vec{1a} \qquad (2.47)$$

In general, $ak_\perp \ll 1$, so $J_1(ak_\perp) \simeq \frac{1}{2}ak_\perp$, and then

$$\vec{j_s}\left(\vec{k}\right) = \frac{4I_0L}{(2\pi)^3}\frac{1 - \cos\left(k_{||}L/2\right)}{k_{||}^2 L^2}\vec{1a} \qquad (2.48)$$

For long waves $\left(\frac{k_{||}L}{2} \ll 1\right)$

$$\vec{j_s}\left(\vec{k}\right) = \frac{1}{2}\frac{I_0L}{(2\pi)^3}\vec{1a} \qquad (2.49)$$

This is the Fourier transform of a delta function at the origin with strength $\frac{1}{2}I_0L$ (an elementary dipole).

33

2.7 Inverse Fourier Transformation

We now have explicit expressions for Z and $\vec{j}_s$, and the Fourier transformed $\vec{E}$ field is $\vec{E} = Z_B \vec{j}_s$. Then, the inverse Fourier transformation is

$$\vec{E}(\vec{x}) = \int \int \int \vec{E}\left(\vec{k}\right) e^{-i\vec{k}\cdot\vec{x}} d^3\vec{k} \tag{2.50}$$

$$\vec{E} = Z_B A_\alpha \vec{j}_s \text{ with } A_\alpha = \begin{bmatrix} \sin\alpha \\ 0 \\ \cos\alpha \end{bmatrix} \tag{2.51}$$

Z_B is shown in Eq.(2.34)

$$d^3\vec{k} = k^2 dk \sin\theta d\theta d\phi$$

The process for integration is as follows.

1. Fix θ, ϕ, and integrate on k from 0 to ∞. Integration on k is effected in the complex k plane.

2. For θ and ϕ integration, we will use the stationary phase method (explanation in [3.2 Stationary point method]). After k integration, for large kr (far field) identify the values (θ, ϕ) that make the phase $(\vec{k} \cdot \vec{x})$ stationary for each observation point $\vec{x}$.

3. We can carry out the θ, ϕ integration by covering the vicinity of the stationary points only. At the stationary point, (θ_s, ϕ_s), we can take the $\vec{E}\left(\vec{k}\right)$ term out of the integral and also we can expand $(\vec{k} \cdot \vec{x})$ to quadratic order in $\theta - \theta_s$ and $\phi - \phi_s$.

4. Perform the integration of $e^{-i\vec{k}\cdot\vec{x}}$ ($\vec{k} \cdot \vec{x}$ has only zeroth and second order terms now). This completes the process for most observation points $\vec{x}$.

5. For certain observation points $\vec{x}$ where the second derivative of $\vec{k} \cdot \vec{x}$ is zero, the expansion must be carried out to the next order.

   For observation points along $\vec{B}$, we need another treatment for the integration

34

because the ϕ derivative of $\vec{k} \cdot \vec{x}$ is zero at that point.

Integration region is all over $\vec{k}$ space. Usually we use $k : 0$ to ∞, $\theta : 0$ to π, $\phi : 0$ to 2π as the integration region. However, for k integration, it is better to integrate from $k = -\infty$ to $k = \infty$. For this reason, we use $k : -\infty$ to ∞, $\theta : 0$ to $\frac{\pi}{2}$, $\phi : 0$ to 2π as the integration region. Inverse Fourier transforms with these integration regions are mathematically identical.
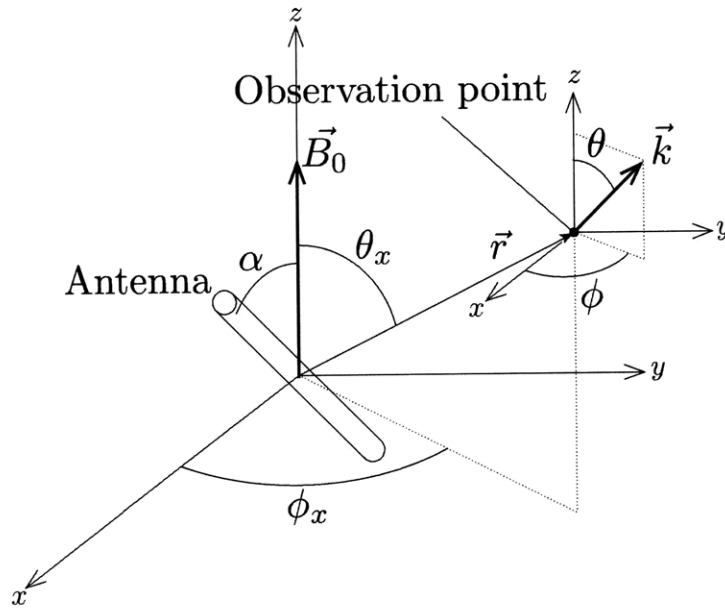

Figure 2-5: Antenna, observation point and $\vec{k}$

35

Chapter 3

Inverse Fourier Transformation

3.1 K integration

As a first step in computing the inverse Fourier transform (Eq.(2.50)), we fix the observation point $\vec{x}(r, \theta_x, \phi_x)$ and the wave direction (θ, ϕ) of $\vec{k} = \vec{K}/l$, then perform the k integration. Now, allow K to be a complex variable and perform complex integration using the residue theorem, although the K integration is in principle along the real axis. In order to use the residue theorem, we need to close the path of integration around some of the poles of $\vec{E}(K)$, which are $K_{u\pm}$ and $K_{d\pm}$ as given by Eq.(2.20) and Eq.(2.21). However, $K_{u\pm}$ is a heavily damped wave when $\cos^{-1} \nu \leq \theta$ and $K_{d\pm}$ is a heavily damped wave when $\cos^{-1}(-\nu) \geq \theta$ as in Section 2.3. Now the integration region is $k : -\infty$ to ∞, $\theta : 0$ to $\frac{\pi}{2}$, $\phi : 0$ to 2π (Section 2.7). In this integration region, $K_{d\pm}$ waves are heavily damped and cannot propagate well. Then, only $K_{u\pm}$ waves can propagate and are included as valid poles.

This closure should be done in the half plane in which the $e^{-i\vec{k}\cdot\vec{x}}$ does not diverge. Thus the imaginary part of $\vec{k} \cdot \vec{x}$ should be negative in this closure.

Now

$$\vec{k} \cdot \vec{x} = \frac{r}{l} K \left[\sin\theta \sin\theta_x \cos(\phi - \phi_x) + \cos\theta \cos\theta_x \right] \tag{3.1}$$

$$\equiv \frac{r}{l} K \cos\gamma \tag{3.2}$$

γ is the angle between $\vec{k}$ and $\vec{x}$, and $\cos\gamma$ is the bracket in Eq.(3.1). Thus, when $\cos\gamma > 0$, we must have $\text{Im}(K) < 0$, and vice versa.

The angle between $\vec{k}$ and $\vec{x}$ is always less than $90°$ (from the $\vec{k}$ tip graphs in Section 3.3). Therefore, $\cos\gamma$ is always positive. Then, the integration path and the valid pole (K_{u+}) are shown circled in Fig.(3-1). With the residue theorem, the inverse
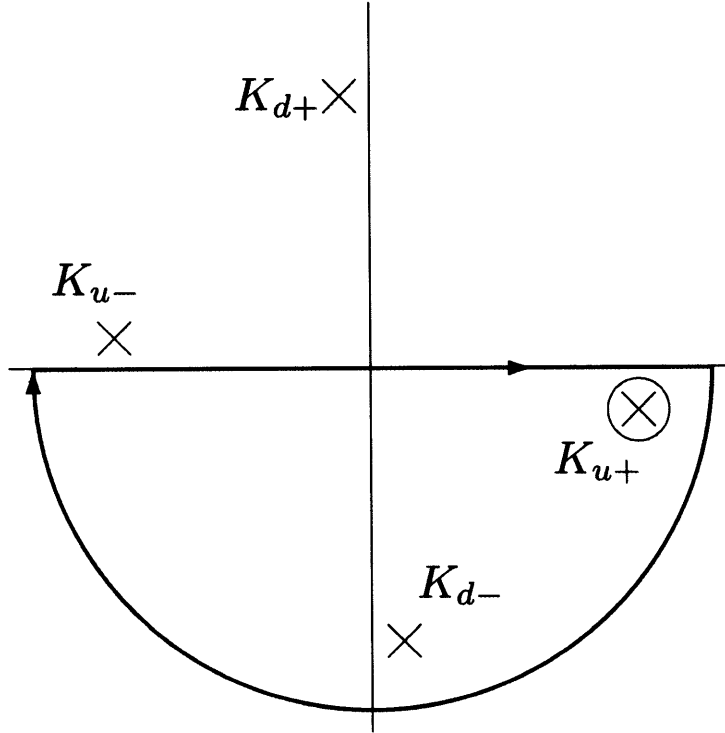
Figure 3-1: K and integration path

Fourier transform is now reduced to a double integral as follows.

$$\vec{E}_{(\vec{r})} = \int_\theta \int_\phi 2\pi i \text{Res}\left[k^2 \vec{E}_{(\vec{k})} e^{-i\vec{k}\cdot\vec{x}} @\text{pole} K_{u+}\right] \frac{\sin\theta}{l} d\theta d\phi \qquad (3.3)$$

Poles are from $\frac{1}{\Delta}$ in Eq.(2.34)($K_{u\pm}$ and $K_{d\pm}$ are the roots of $\Delta = 0$). Thus, the residue of $\frac{1}{\Delta}$ is

$$\text{Res}\left(\frac{1}{\Delta}\right) = \left.\frac{K - K_{u+}}{-\frac{\cos^2\theta - \nu^2}{\nu^2}\left(K^2 - K_d^2\right)\left(K^2 - K_u^2\right)}\right|_{K=K_{u+}} = -\frac{\sqrt{\nu\left(\cos\theta - \nu\right)}}{4\cos\theta} \qquad (3.4)$$

38

We can get Res $\left[\vec{E}_{(\vec{k})}e^{-i\vec{k}\cdot\vec{x}}@poleK_{u+}\right]$ using Eq.(3.4), and substituting K_{u+} into Eq.(2.50) and Eq.(2.51). Then, considering the direction of the integration paths, the integration is

$$\vec{E}_{(\vec{x})} = \int_\theta \int_\phi 2\pi i \, Z_B|_{K_{u+}} \, A_\alpha \vec{j_s} e^{-i\frac{r}{l}\sqrt{\nu}\Phi_{(\theta,\phi,\theta_x,\phi_x)}} \frac{\sin\theta}{l} d\theta d\phi \qquad (3.5)$$

$$A_\alpha = \begin{bmatrix} \sin\alpha \\ 0 \\ \cos\alpha \end{bmatrix} \qquad (3.6)$$

$$\Phi_{(\theta,\phi,\theta_x,\phi_x)} = \frac{\sin\theta\sin\theta_x\cos(\phi-\phi_x) + \cos\theta\cos\theta_x}{\sqrt{\cos\theta-\nu}} \qquad (3.7)$$

$Z_{B(K_{u+})}$

$$= -\frac{\sqrt{\nu(\cos\theta-\nu)}}{4\sigma_{ce}\cos\theta} \left[\begin{array}{c} -p + K^2\sin^2\theta\left(-p\cos^2\phi + \frac{i}{\nu}\sin^2\phi\right) \\ -\left(1+K^2\sin^2\theta\right) - iK^2\left(1+K^2\right)\left(\frac{1}{\nu}-\nu\right)\sin^2\theta\sin\phi\cos\phi \\ -K^2\left(p\cos\phi+\sin\phi\right)\sin\theta\cos\theta \end{array} \right.$$

$$-\left(1+K^2\sin^2\theta\right) - iK^2\left(1+K^2\right)\left(\frac{1}{\nu}-\nu\right)\sin^2\theta\sin\phi\cos\phi$$

$$-\left(p-i\frac{K^2}{\nu}\sin^2\theta\right)\cos^2\phi - p\left(1+K^2\sin^2\theta\right)\sin^2\phi$$

$$K^2\left(-p\sin\phi+\cos\phi\right)\sin\theta\cos\theta$$

$$\left. \begin{array}{c} K^2\sin\theta\cos\theta\left(\sin\phi - p\cos\phi\right) \\ -K^2\sin\theta\cos\theta\left(p\sin\phi+\cos\phi\right) \\ -pK^2\cos^2\theta + i\nu\left(1+K^2\right) \end{array} \right]_{K=K_{u+}} \qquad (3.8)$$

3.2 The Stationary Phase Method

For the θ and ϕ integrations, we will use the stationary phase method. For the integration of Eq.(3.5), if $\frac{r}{l}$ is large, which means the observation point is far from the antenna, the exponential term $e^{-i\frac{r}{l}\sqrt{\nu}\Phi_{(\theta,\phi,\theta_x,\phi_x)}}$ oscillates much more rapidly than the other terms $\left(2\pi i Z_{(K_u)}A\vec{j_s}\sin\theta\right)$. However, at some points where $\frac{\partial\Phi}{\partial\theta} = \frac{\partial\Phi}{\partial\phi} = 0$, the exponential term does not vary rapidly. These points are called stationary points. For

39

example, Fig.(3-2) is the real part of the integrand (x component) with $r = 1000$km. There are two stationary points in this graph (red dots). For wave orientation (θ, ϕ)
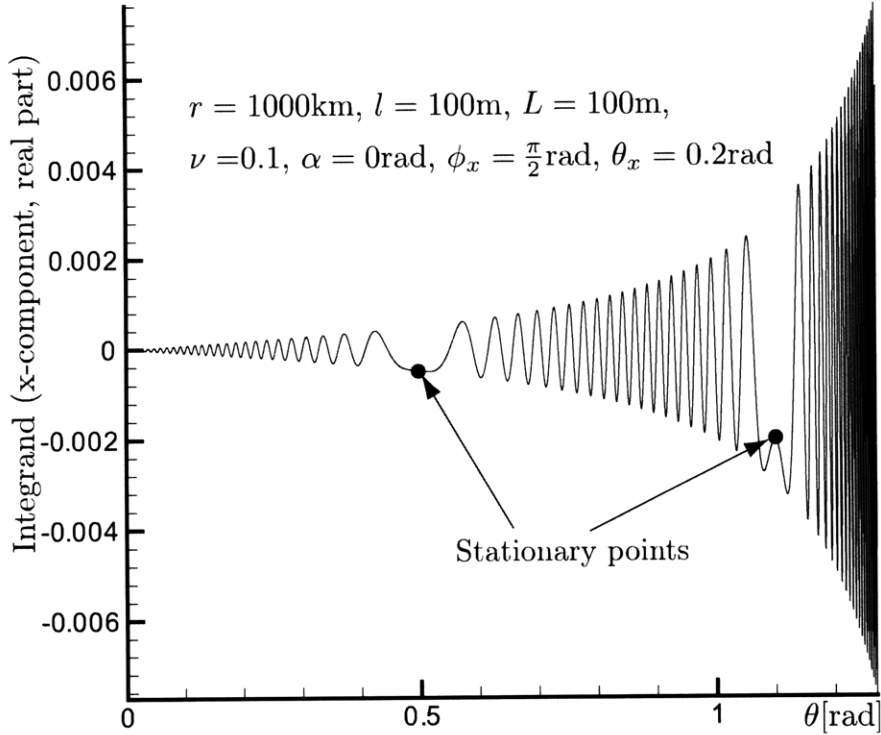

Figure 3-2: Integrand and stationary points

not near these stationary points, the integrand $\left(\vec{\tilde{E}} \left(\vec{k} \right) e^{-i\vec{k}\cdot\vec{x}} \right)$ contribution to the integration is small, because $e^{-i\vec{k}\cdot\vec{x}}$ term oscillates rapidly around zero, and cancellations occur in the integration.

Near the stationary point (θ_s, ϕ_s), we can take the $\left(2\pi i Z_{(K_{u,d})} A \vec{\tilde{j}}_s \sin \theta \right)$ terms out of the integral and we only have to integrate the exponential term. In addition, since only the vicinity of (θ_s, ϕ_s) contributes, the exponent can be expanded in a Taylor series about this point, where the first derivatives are zero, and terms higher than second order in $(\theta - \theta_s)$, $(\phi - \phi_s)$ can be neglected.

As in Section 2.7 and Section 3.1, we only include K_{u+} wave in the Inverse Fourier Transform calculation. Stationary points can be calculated as follows.

The phase Φ can be written as in Eq.(3.7). The stationary point for ϕ $(\frac{\partial \Phi}{\partial \phi} = 0)$ can

be calculated from this equation.

$$\frac{\partial \Phi}{\partial \phi} = -\frac{\sin \theta \sin \theta_x}{\sqrt{\cos \theta - \nu}} \sin (\phi - \phi_x) = 0 \tag{3.9}$$

Then,

$$\phi = \phi_x \quad \text{or} \quad \phi_x + \pi \tag{3.10}$$

Stationary points for θ $\left(\frac{\partial \Phi}{\partial \theta} = 0\right)$ for each stationary point for ϕ can be also calculated from Eq.(3.7).

$$\frac{\partial \Phi}{\partial \theta} = \frac{\frac{1}{2}\sin \theta \cos (\phi \pm \phi_x) - (\cos \theta - \nu) \sin (\theta \pm \theta_x)}{(\cos \theta - \nu)^{3/2}} = 0 \qquad \left(\begin{array}{l} + : \ \phi = \phi_x + \pi \\ - : \ \phi = \phi_x \end{array} \right. \tag{3.11}$$

Fig.(3-3) and Fig.(3-4) are plots of the stationary points $\left(\frac{\partial \Phi}{\partial \theta} = \frac{\partial \Phi}{\partial \phi} = 0\right)$ for changing observation direction θ_x $(\phi_x = 0)$ and for $\nu = 0.1$ and $\nu = 0.8$. For $\nu < 0.5$, there is a point where $\frac{\partial^2 \Phi}{\partial \theta^2} = 0$ on the stationary points line, for $\nu \geq 0.5$, there is not a point where $\frac{\partial^2 \Phi}{\partial \theta^2} = 0$ on the stationary points line. This point follows from

$$\frac{\partial^2 \Phi}{\partial \theta^2} = \frac{\cos \theta_x}{2(\cos \theta - \nu)^{3/2}} - \frac{\cos (\theta - \theta_x)}{\sqrt{\cos \theta - \nu}} = 0 \tag{3.12}$$

Therefore, from Eq.(3.11) and Eq.(3.12), the second derivative of Φ is zero when

$$\cos \theta = \nu + \sqrt{\frac{1 - \nu^2}{3}} \tag{3.13}$$

In the stationary phase method, the waves which do not propagate to the observation point are cancelled mathematically, and only the waves which propagate to the observation point (they are stationary points) contribute to the integration. Therefore, the wave field is the sum of the integrands at the stationary points and contributions from the vicinity of the stationary points. Terms other than the exponential term can be moved out of the integral at and in the vicinity of the stationary points. Then, we can integrate the exponential term by expanding Φ in a Taylor series about the stationary points. Only the integrand in the vicinity of the stationary point con-
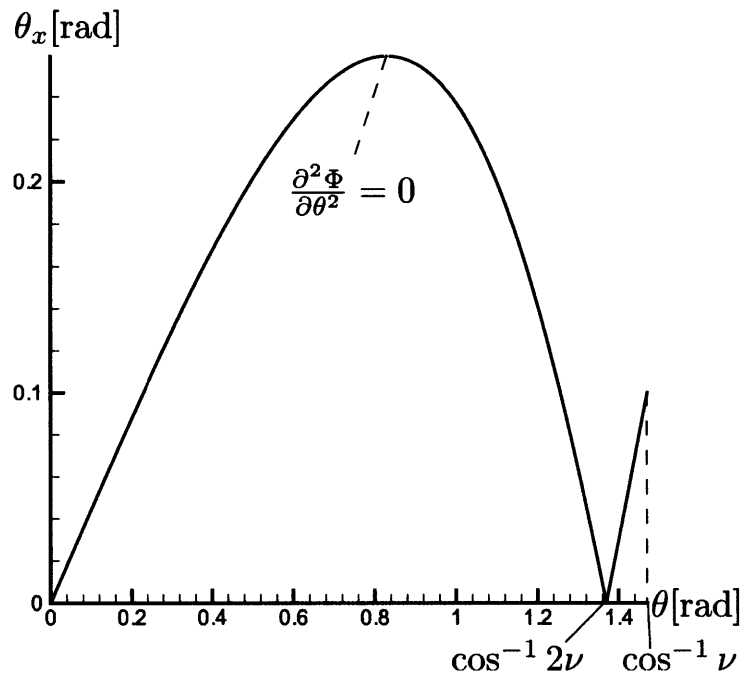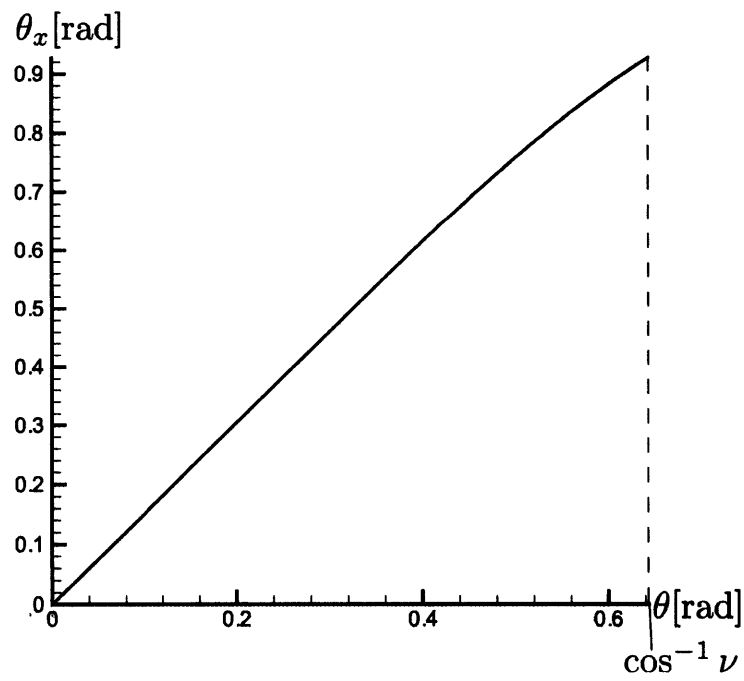
Figure 3-3: Stationary points ($\nu = 0.1$)

Figure 3-4: Stationary points ($\nu = 0.8$)

42

tributes, so we can set the integration region from $-\infty$ to ∞. The integration of the exponential term can be calculated as follows.

$$
\int_{\theta=0}^{\frac{\pi}{2}} \int_{\phi=0}^{2\pi} e^{-i\frac{r}{l}\sqrt{\nu}\Phi} d\theta d\phi
$$

$$
= \int_{\theta} \int_{\phi} \exp\left[-i\frac{r}{l}\sqrt{\nu}\left\{ \Phi|_{\theta_s,\ \phi_s} + \frac{1}{2}\left.\frac{\partial^2\Phi}{\partial\theta^2}\right|_{\theta_s,\ \phi_s}(\theta-\theta_s)^2 + \frac{1}{2}\left.\frac{\partial^2\Phi}{\partial\phi^2}\right|_{\theta_s,\ \phi_s}(\phi-\phi_s)^2 \right\} \right] d\theta d\phi
$$

$$
= e^{-i\frac{r}{l}\sqrt{\nu}\Phi(\theta_s,\ \phi_s)} \frac{\pi}{i\frac{r}{l}\frac{\sqrt{\nu}}{2}\sqrt{\left.\frac{\partial^2\Phi}{\partial\theta^2}\right|_{\theta_s,\ \phi_s} \left.\frac{\partial^2\Phi}{\partial\phi^2}\right|_{\theta_s,\ \phi_s}}} \tag{3.14}
$$

As a result of complex integration for the $\vec{k}$ integration and the stationary phase method, the electric field made by the wave can be written as

$$
\vec{E}(\vec{r}) = \sum_{\text{Stationary Points}} -2\pi i \frac{4I_0 L}{(2\pi)^3} \frac{1-\cos\left(\frac{k_\parallel L}{2}\right)}{k_\parallel^2 L^2} e^{-i\frac{r}{l}\sqrt{\nu}\Phi(\theta_s,\ \phi_s)}
$$

$$
\frac{\pi}{i\frac{r}{l}\frac{\sqrt{\nu}}{2}\sqrt{\left.\frac{\partial^2\Phi}{\partial\theta^2}\right|_{\theta_s,\ \phi_s} \left.\frac{\partial^2\Phi}{\partial\phi^2}\right|_{\theta_s,\ \phi_s}}} \frac{K_u^2}{l^2} \frac{\sin\theta_s}{l} Z_B|_{\theta_s,\ \phi_s} \begin{bmatrix} \sin\alpha \\ 0 \\ \cos\alpha \end{bmatrix} \tag{3.15}
$$

Also, from Maxwell's equations Eq.(2.1) and Eq.(2.2),

$$
\vec{B} = \frac{\vec{k} \times \vec{E}}{\omega} \tag{3.16}
$$

Therefore, the magnetic field made by the wave can be written in the same way as Eq.(3.15).

$$
\vec{B}(\vec{r}) = \sum_{\text{Stationary Points}} -2\pi i \frac{4I_0 L}{(2\pi)^3} \frac{1-\cos\left(\frac{k_\parallel L}{2}\right)}{k_\parallel^2 L^2} e^{-i\frac{r}{l}\sqrt{\nu}\Phi(\theta_s,\ \phi_s)} \tag{3.17}
$$

$$
\frac{\pi}{i\frac{r}{l}\frac{\sqrt{\nu}}{2}\sqrt{\left.\frac{\partial^2\Phi}{\partial\theta^2}\right|_{\theta_s,\ \phi_s} \left.\frac{\partial^2\Phi}{\partial\phi^2}\right|_{\theta_s,\ \phi_s}}} \frac{K_u^2}{l^2} \frac{\sin\theta_s}{l} \frac{1}{\nu\omega_{ce}} \vec{k} \times \left\{ Z_B|_{\theta_s,\ \phi_s} \begin{bmatrix} \sin\alpha \\ 0 \\ \cos\alpha \end{bmatrix} \right\}
$$

3.3 Group Velocity Analysis

When integrating over $\vec{k}$ in the inverse Fourier transformation, the frequency ω must vary with $\vec{k}$ to satidfy the Dispersion Relation. Let us examine the vicinity of one $\vec{k}$ vector; vary $\vec{k}$ by $\delta\vec{k}$, calculate $\delta\omega = \frac{\partial\omega}{\partial\vec{k}}\cdot\delta\vec{k}$ and then calculate the variation of the phase $\phi = -\omega t + \vec{k}\cdot\vec{x}$ (given t, $\vec{x}$):

$$\delta\phi = -\frac{\partial\omega}{\partial\vec{k}}\cdot\delta\vec{k}t + \delta\vec{k}\cdot\vec{x} = \left(\vec{x} - \frac{\partial\omega}{\partial\vec{k}}t\right)\cdot\delta\vec{k} \tag{3.18}$$

When $\vec{x} = \frac{\partial\omega}{\partial\vec{k}}t$ (i.e., moving at the velocity $\vec{v_G} = \frac{\partial\omega}{\partial\vec{k}}$), the phase does not change, and so the Fourier components ad up directly. For other velocities (at this $\vec{k}$, $\vec{x}$, t) the phase varies rapidly, and the net effect is small. Thus, information and energy propagates at $\vec{v_G}$ (the group velocity), not at the $\vec{v_\phi} = \frac{\omega}{k}\frac{\vec{k}}{k}$ phase velocity of each partial wave.

$$\vec{v_G} = \frac{\partial\omega}{\partial\vec{k}} \tag{3.19}$$

We define polar angles

θ, ϕ :polar angle of $\vec{k}$

θ_x, ϕ_x :polar angles of the vector $\vec{x}$ to the observation point

θ_G, ϕ_G :polar angles of $\vec{v_G}$

The direction of $\vec{v_G}$ should be same as the direction of the observation point $\vec{x}$. So, for the waves to be observed from (θ_x, ϕ_x),

$$\theta_G = \theta_x, \phi_G = \phi_x \tag{3.20}$$

should be satisfied. For very small damping ($\delta \ll \nu$), the dispersion relations (Eq.(2.20) become

$$K_u^2 = \frac{\nu}{\cos\theta - \nu}\left(\text{or } \nu = \frac{K_u^2\cos\theta}{1 + K_u^2}\right) \tag{3.21}$$

So, we define

$$K_u = \sqrt{\frac{\nu}{\cos\theta - \nu}}$$

44

K_u propagates only for $\theta < \cos^{-1} \nu$, K_d propagates only for $\theta > \pi - \cos^{-1} \nu$, where $\nu = \frac{\omega}{\omega_{ce}}$. Using $K_x = K \sin \theta \cos \phi$, $K_y = K \sin \theta \sin \phi$, $K_z = K \cos \theta$, so for K_u wave,

$$
\begin{aligned}
V_{Gxu} &= \frac{v_{Gx}}{\omega_{ce}l} = \frac{\partial \omega}{\partial K_x} \frac{1}{\omega_{ce}l} = K_z \frac{1 - K^2}{(1 + K^2)^2} \frac{K_x}{K} \\
V_{Gyu} &= \frac{v_{Gy}}{\omega_{ce}l} = \frac{\partial \omega}{\partial K_y} \frac{1}{\omega_{ce}l} = K_z \frac{1 - K^2}{(1 + K^2)^2} \frac{K_y}{K} \\
V_{Gzu} &= \frac{v_{Gz}}{\omega_{ce}l} = \frac{\partial \omega}{\partial K_z} \frac{1}{\omega_{ce}l} = \frac{K}{1 + K^2} \left(1 + \frac{1 - K^2}{1 + K^2} \cos^2 \theta \right)
\end{aligned}
\tag{3.22}
$$

From Eq.(3.22),

$$
\begin{aligned}
\cos \theta_{Gu+} &= \frac{2 \cos \theta \left(\cos \theta - \nu \right) + \sin^2 \theta}{\sqrt{4 \left(\cos \theta - \nu \right)^2 + \sin^2 \theta}} \\
\cos \theta_{Gu-} &= -\frac{2 \cos \theta \left(\cos \theta - \nu \right) + \sin^2 \theta}{\sqrt{4 \left(\cos \theta - \nu \right)^2 + \sin^2 \theta}}
\end{aligned}
\tag{3.23}
$$

As in Section 2.7 and Section 3.1, we only include the K_{u+} wave in the Inverse Fourier Transform calculation.

There are three methods to visualize the wave propagation:

1. The $\vec{V_G}$ graph

2. The $\vec{k}$ tip graph

3. The θ vs θ_x graph

The $\vec{V_G}$ graph is a locus of the components of $\vec{V_G}$ along $\vec{B_0}$ and perpendicular to $\vec{B_0}$, with the $\vec{k}$ direction θ as a running parameter. Fig.(3-5) is a $\vec{V_G}$ graph for $\nu = 0.1$. For the K_{u+} wave, $\vec{V_G}$ is on the $\hat{z}$ axis for $\theta = 0$, then θ_G increases until it reaches its local maximum value, then it decreases to zero at $\theta = \cos^{-1}(2\nu)$ and goes to negative. When $\theta = \cos^{-1} \nu$, the K_u wave is resonant. The K_u wave doesn't propagate for $\theta > \cos^{-1} \nu$, so that branch ends at this point.
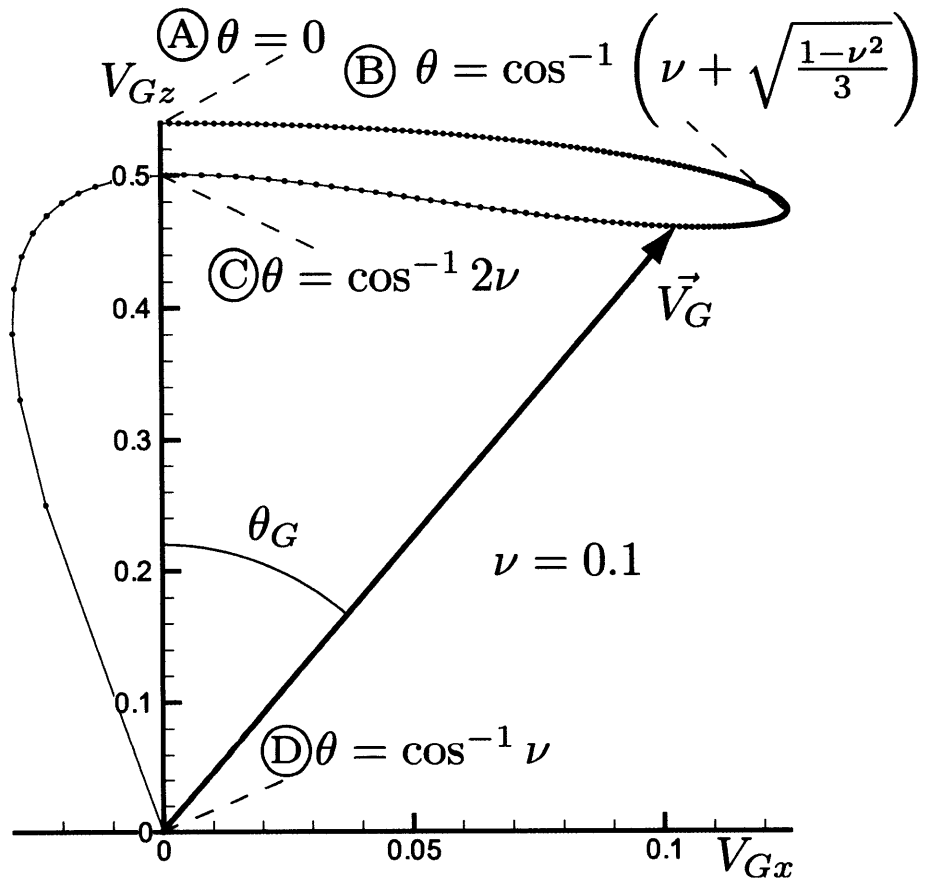
Figure 3-5: $\vec{V}_G$ graph

The $\vec{k}$ tip graph is a locus of $\vec{k}$ with θ as a running parameter. $\vec{V_G}$ is perpendicular to the locus of $\vec{k}$ at each point. Fig.(3-6) is a $\vec{k}$ tip graph for $\nu = 0.1$. For the K_u wave, θ cannot be larger than $\cos^{-1} \nu$, so the $\vec{k}$ tip curve for K_u goes to the asymptote $\theta = \cos^{-1} \nu$.
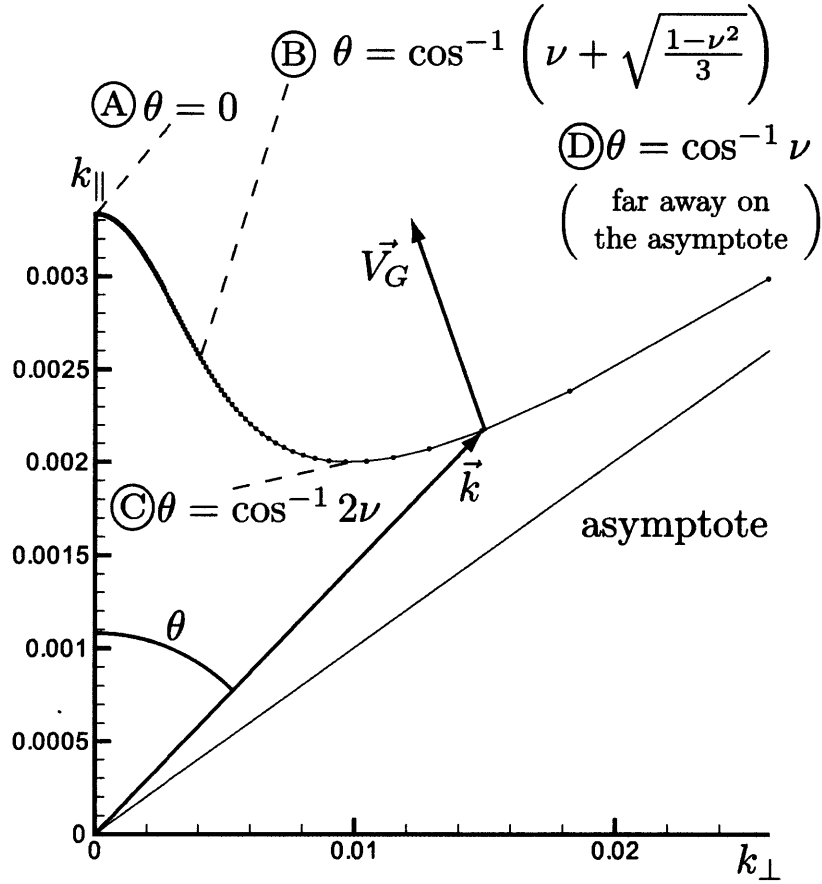

Figure 3-6: $\vec{k}$ tip graph

Using Eq.(3.23), we can draw the θ vs θ_x graph. For the wave to propagate, θ_x should be equal to θ_G. Fig.(3-7) is a θ vs θ_x graph for $\nu = 0.1$. For one observation point with θ_x, only the waves with θ on those curves in the graph can propagate. In Fig.(3-5), Fig.(3-6) and Fig.(3-7), Ⓐ, Ⓑ, Ⓒ and Ⓓ correspond to

Ⓐ:$\theta = 0$, Ⓑ:$\theta = \cos^{-1}\left(\nu + \sqrt{\frac{1-\nu^2}{3}}\right)$ max, Ⓒ:$\theta = \cos^{-1} 2\nu$, Ⓓ:$\theta = \cos^{-1} \nu$
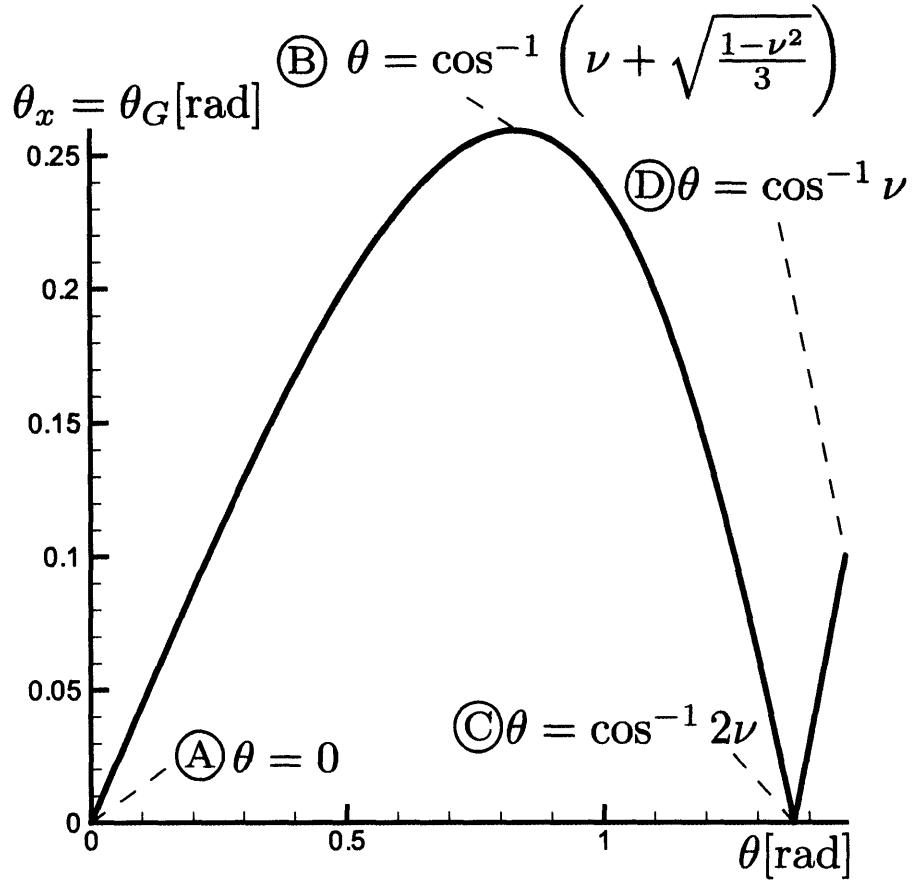
Figure 3-7: θ vs θ_x graph

This relation between θ_x and θ is just as same as the relation between θ_x and θ_s in the Stationary Phase Method(Section 3.2). Fig.(3-3) and Fig.(3-7) show the same relation between θ_x and θ. Also, the equations in the Stationary Phase Method and Group Velocity Analysis are mathematically the same. Therefore, in the same way as in the Stationary Phase Method, Group Velocity analysis shows that electromagnetic wave propagating to one observation point is the sum of $\vec{k}$ waves whose group velocity is in the direction to that observation point and the waves in the vicinity of those $\vec{k}$ waves. The Stationary Phase Method is a mathematical treatment, but the Group Velocity analysis shows the physical meaning of it.

The shape of the graph and the wave propagation pattern varies with ν. There are three distinct ranges of ν.

Range 1: $\nu \leq \sqrt{\frac{1}{28}}$

Range 2: $\sqrt{\frac{1}{28}} \leq \nu \leq 0.5$

Range 3: $\nu \geq 0.5$

In Range 1 (Fig.(3-8), Fig.(3-9), Fig.(3-10), $\nu = 0.1$), θ_G does not reach its maximum on the resonance point. θ_G reaches its maximum when $\vec{k}$ has $\cos\theta = \nu + \sqrt{\frac{1-\nu^2}{3}}$ (inflection point) and θ_G at the resonance point is smaller than θ_G at the inflection point. In Range 2 (Fig.(3-11), Fig.(3-12), Fig.(3-13), $\nu = 0.25$), θ_G at the resonance point is larger than θ_G at the inflection point. In Range 3 (Fig.(3-14), Fig.(3-15), Fig.(3-16), $\nu = 0.8$), the first branch ($\theta \leq \cos^{-1} 2\nu$) disapears and θ_G simply increases to the resonance point. When $\nu = \sqrt{\frac{1}{28}}$ (Fig.(3-17), Fig.(3-18), Fig.(3-19), $\nu = \sqrt{\frac{1}{28}}$), θ_G on the resonance point has the same value as θ_G on the inflection point (namely, 10.893°). When $\nu = 0.5$ (Fig.(3-20), Fig.(3-21), Fig.(3-22), $\nu = 0.5$), the first branch just dissapears.
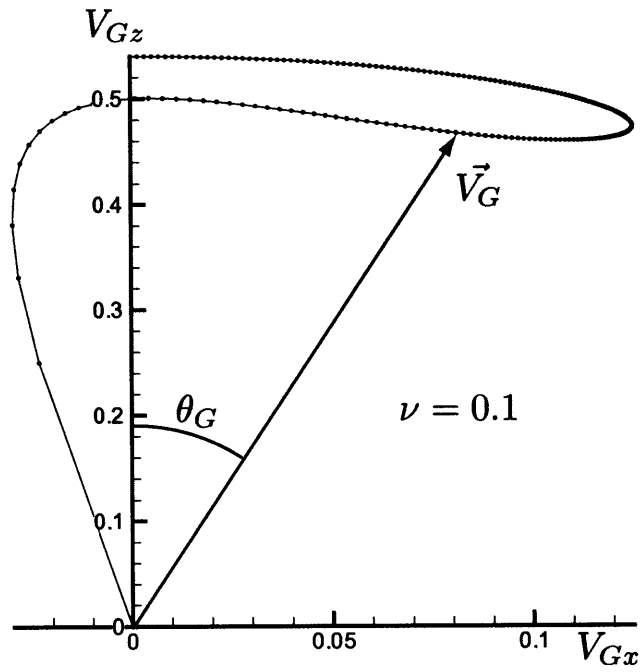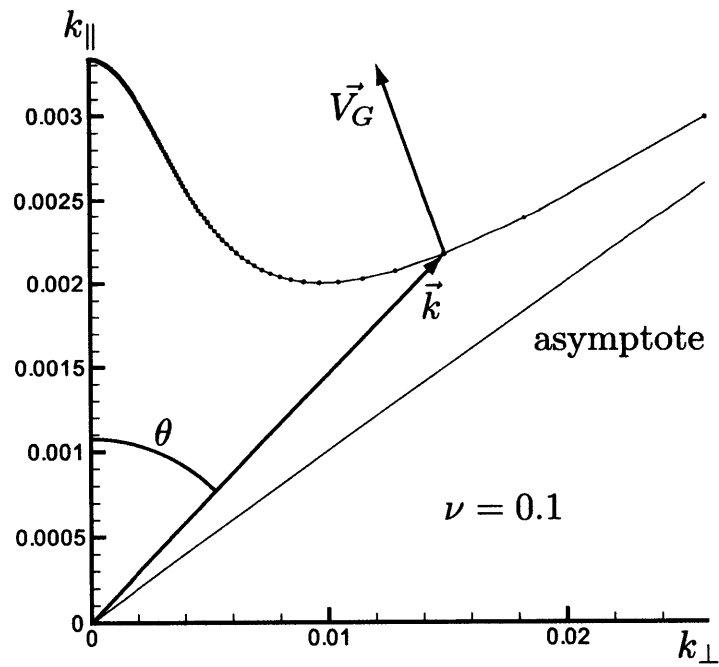
49

Figure 3-8: $\vec{V_G}$ graph ($\nu = 0.1$)
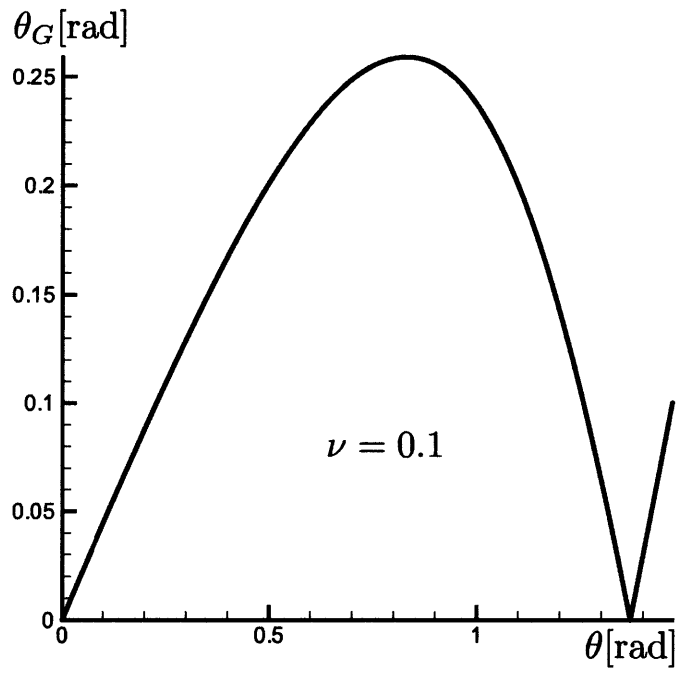

Figure 3-9: $\vec{k}$ tip graph ($\nu = 0.1$)

Figure 3-10: θ vs θ_x graph ($\nu = 0.1$)
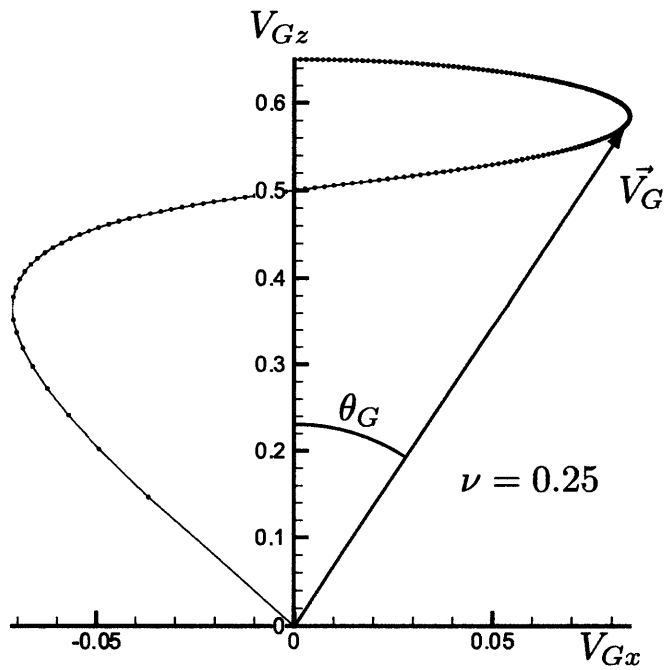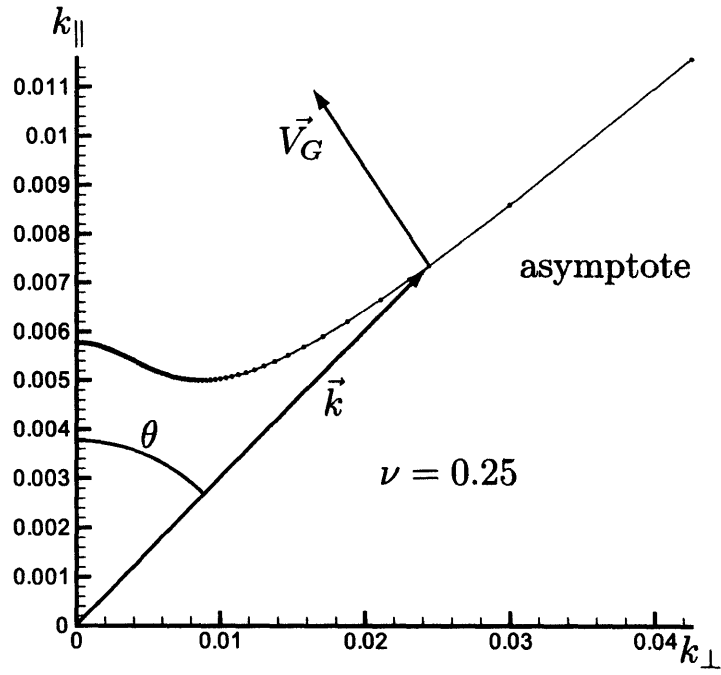

Figure 3-11: $\vec{V}_G$ graph ($\nu = 0.25$)

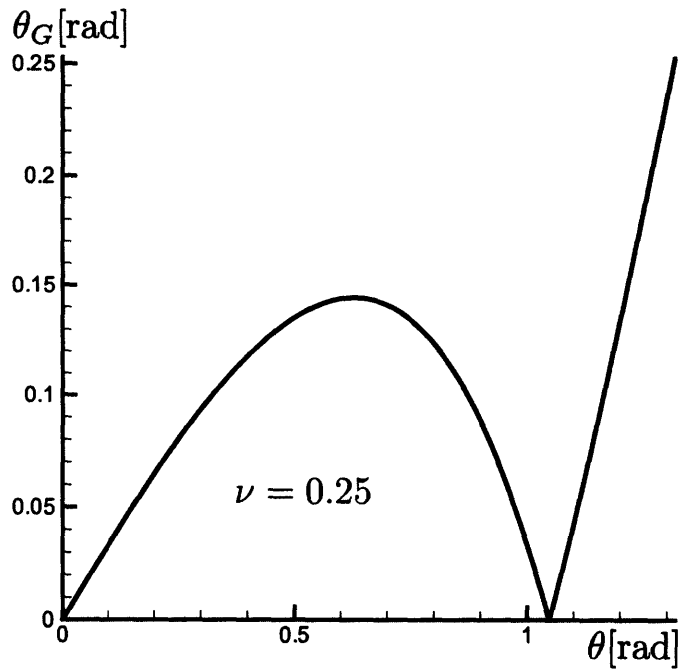Figure 3-12: $\vec{k}$ tip graph ($\nu = 0.25$)

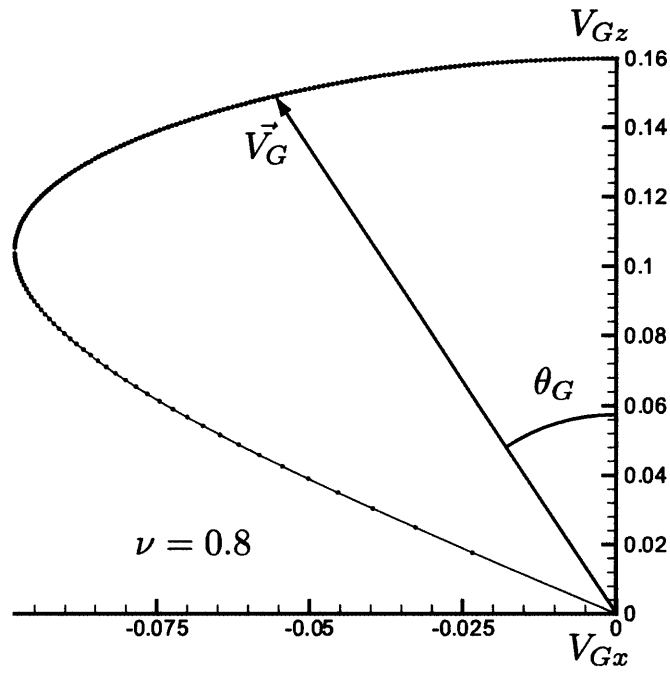
Figure 3-13: θ vs θ_x graph ($\nu = 0.25$)

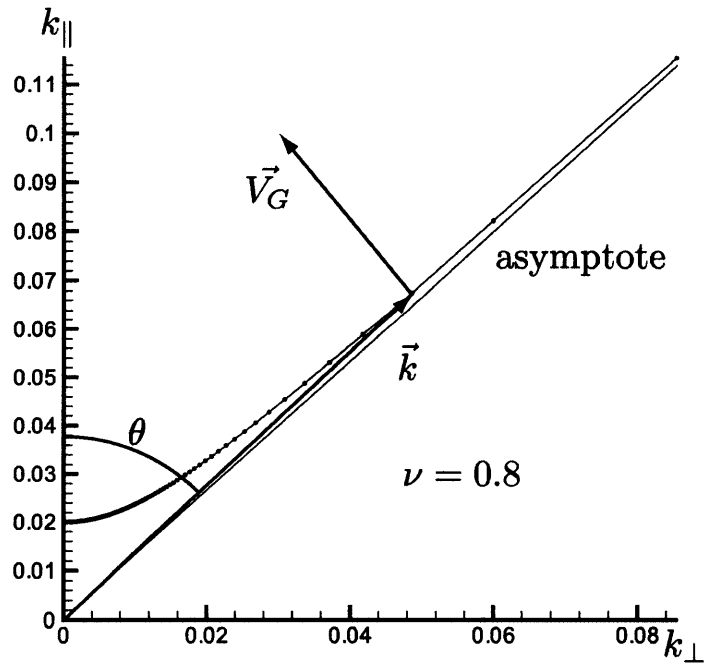Figure 3-14: $\vec{V}_G$ graph ($\nu = 0.8$)
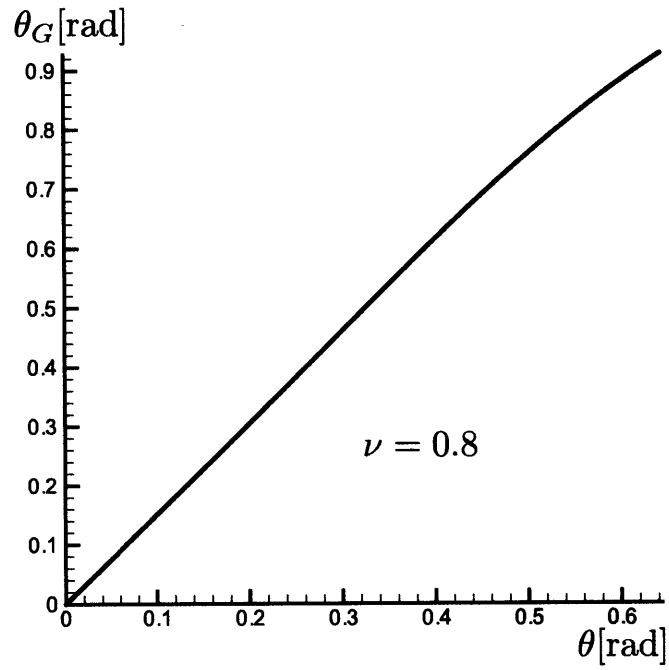

Figure 3-15: $\vec{k}$ tip graph ($\nu = 0.8$)
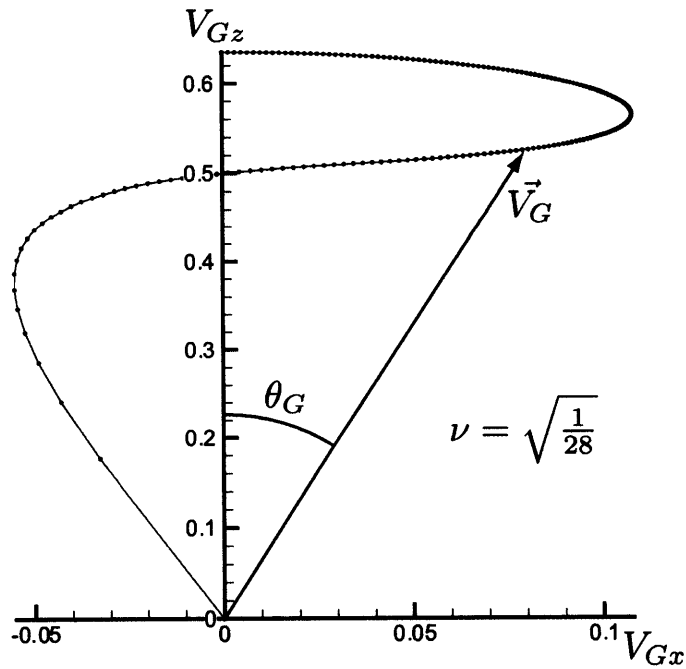
Figure 3-16: θ vs θ_x graph ($\nu = 0.8$)

Figure 3-17: $\vec{V_G}$ graph ($\nu = \sqrt{\frac{1}{28}}$)
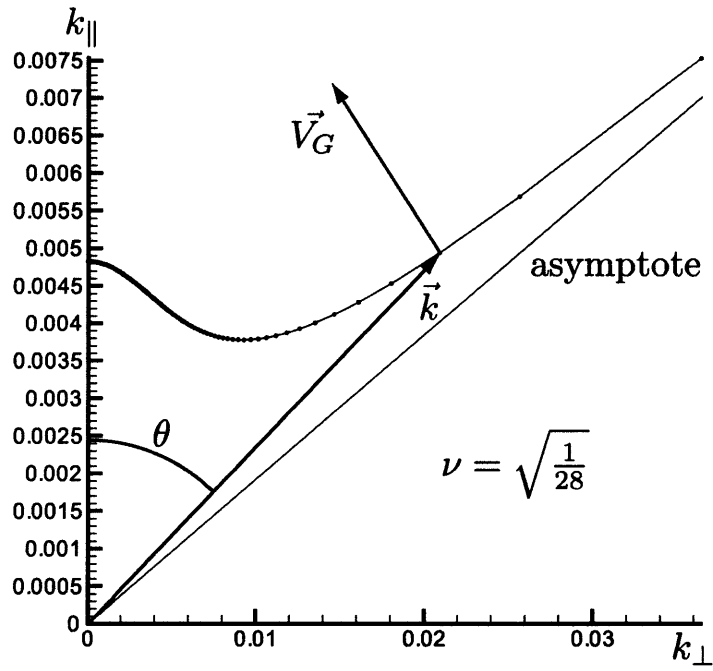
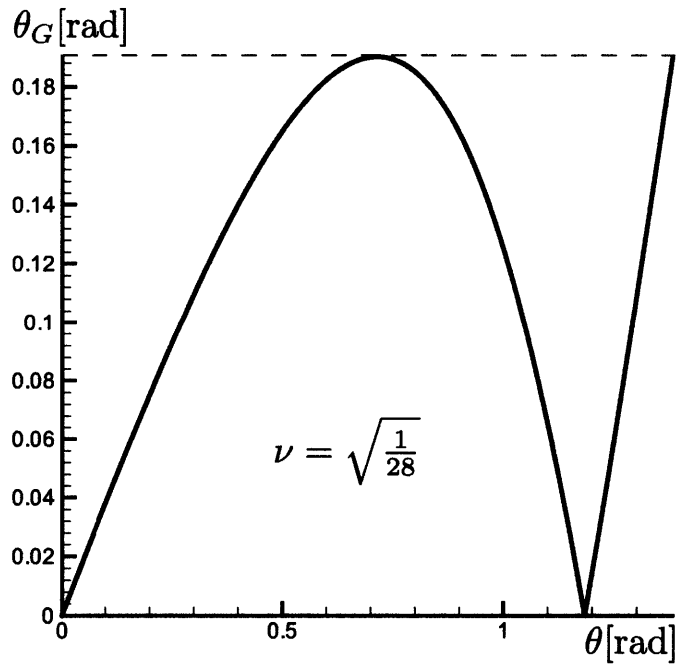Figure 3-18: $\vec{k}$ tip graph $(\nu = \sqrt{\frac{1}{28}})$

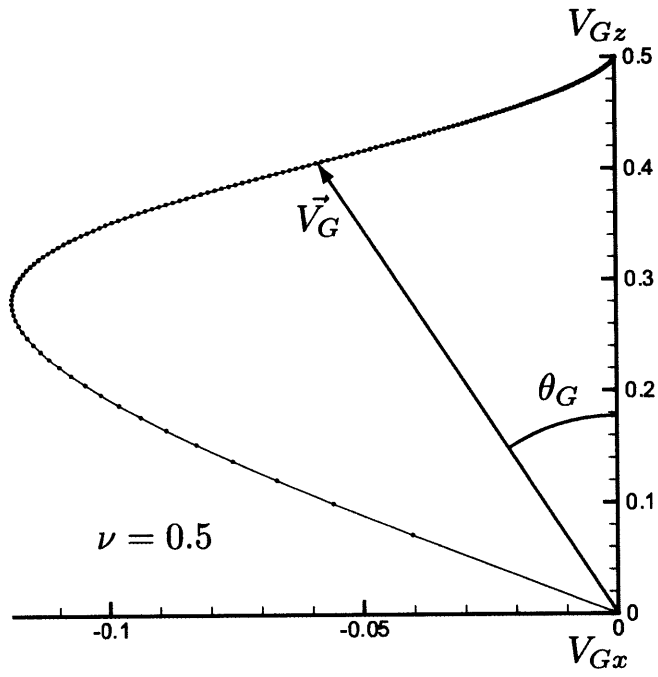Figure 3-19: θ vs θ_x graph $(\nu = \sqrt{\frac{1}{28}})$

Figure 3-20: $\vec{V}_G$ graph ($\nu = 0.5$)
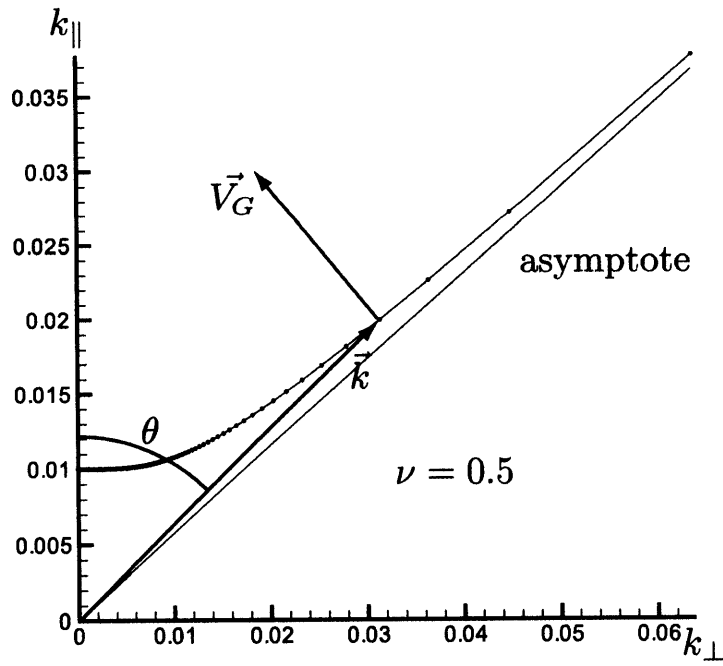

Figure 3-21: $\vec{k}$ tip graph ($\nu = 0.5$)

Figure 3-22: θ vs θ_x graph ($\nu = 0.5$)
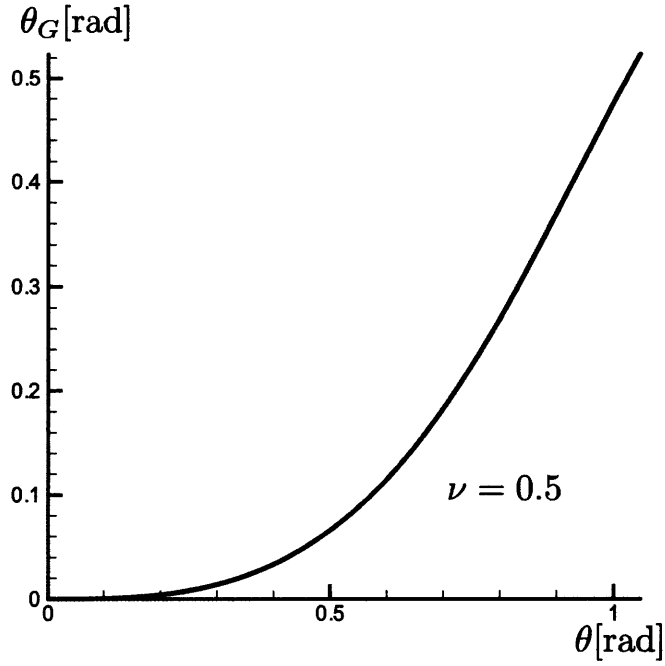
3.3.1 Range 1: $\nu \leq \sqrt{\frac{1}{28}}$

The branch that is observed, as well as the particular $\vec{k}$ within that branch, changes as the observation point angle θ_x changes. Now, consider the wave propagation in Range 1 ($\nu \leq \sqrt{\frac{1}{28}}$). First, if the observation point is on the $\hat{z}$ axis, which means $\theta_x = 0$, two waves propagate as in Fig.(3-23), Fig.(3-24), and Fig.(3-25) at $\phi = \phi_x$.
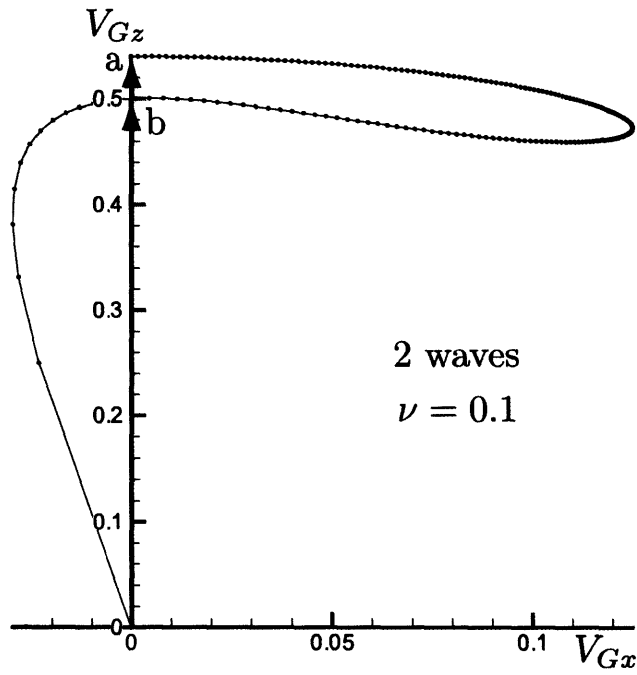
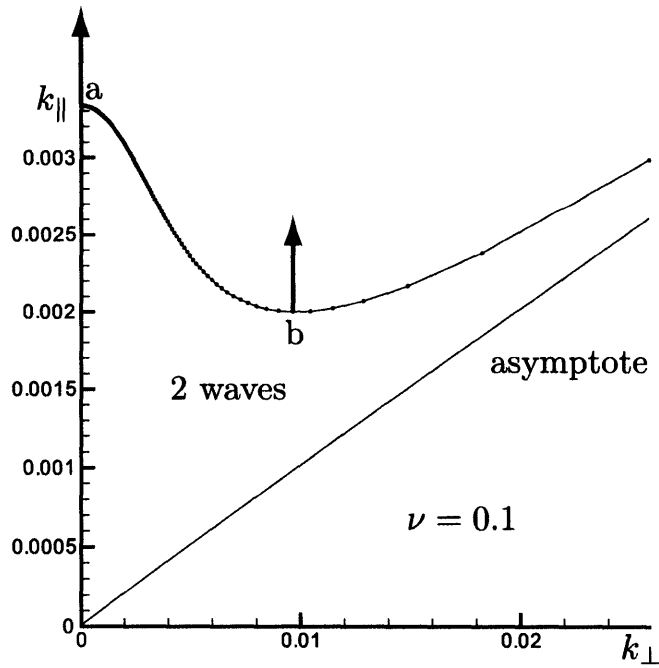Figure 3-23: Region 1 $\vec{V}_G$ graph, $\nu = 0.1$ (Propagation along $\vec{B}_0$)

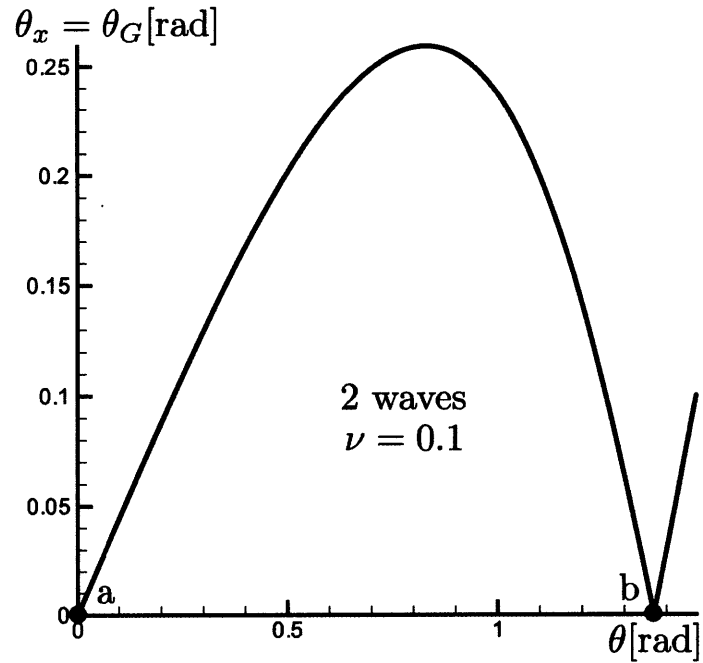Figure 3-24: Region 1 $\vec{k}$ tip graph, $\nu = 0.1$ (Propagation along $\vec{B}_0$)

Figure 3-25: Region 1 θ vs θ_x graph, $\nu = 0.1$ (Propagation along $\vec{B}_0$)

In region 2, when $0 < \theta_x < \sin^{-1}\nu$, three waves propagate as in Fig.(3-26), Fig.(3-27), and Fig.(3-28). Two waves have $\phi = \phi_x$ and one wave has $\phi = \pi + \phi_x$, but these three waves have $\theta = \theta_G = \theta_x$.
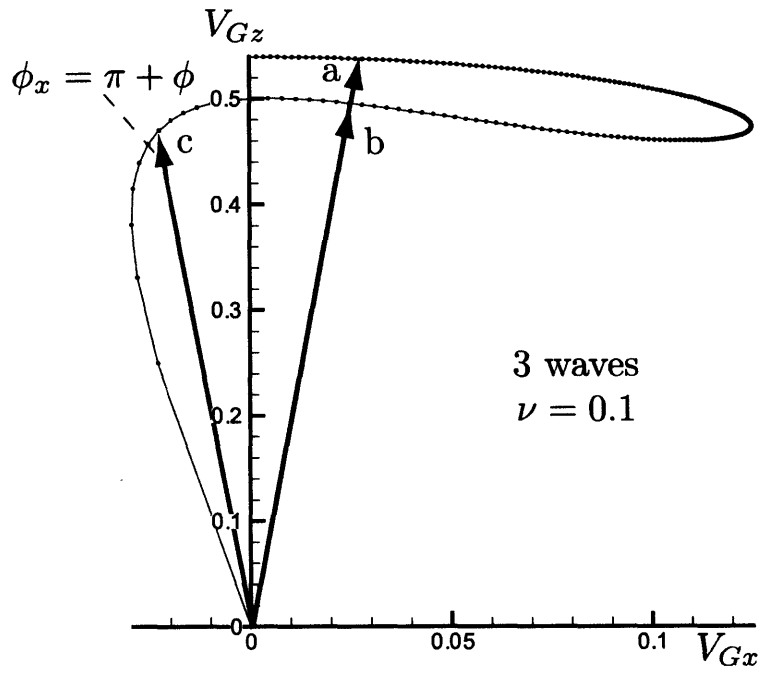
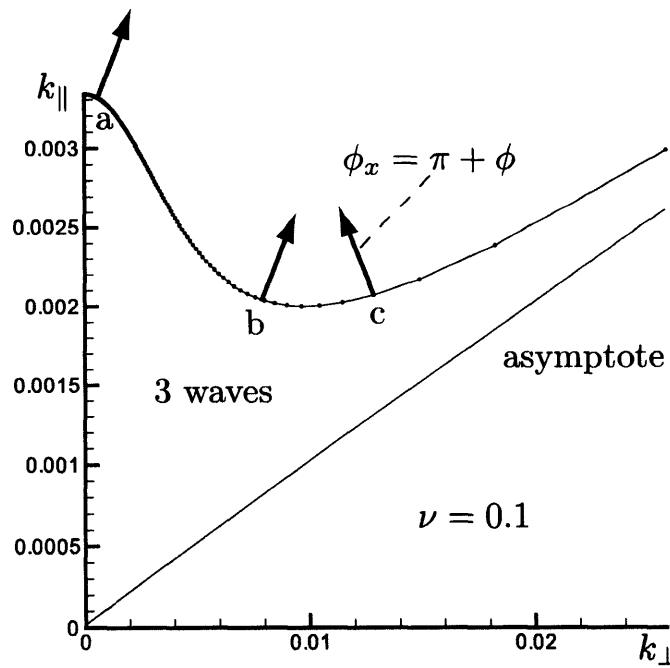Figure 3-26: Region 2 $\vec{V_G}$ graph, $\nu = 0.1$ (very near $\vec{B_0}$)

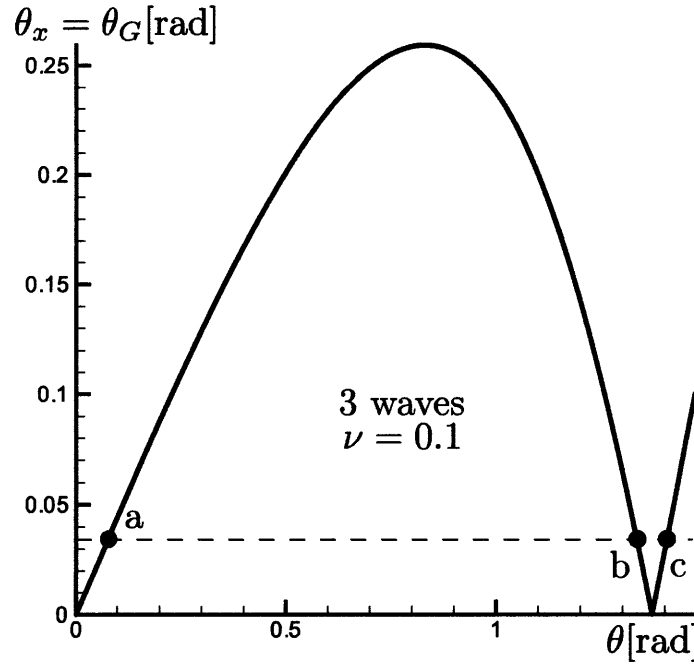Figure 3-27: Region 2 $\vec{k}$ tip graph, $\nu = 0.1$ (very near $\vec{B_0}$)

Figure 3-28: Region 2 θ vs θ_x graph, $\nu = 0.1$ (very near $\vec{B_0}$)

On the point where $\theta_x = \sin^{-1} \nu$, three waves propagate. One of these waves is resonant as in Fig.(3-29), Fig.(3-30), and Fig.(3-31). From Fig.(3-30), we can easily see that θ_x at the resonant point is $\theta_x = \frac{\pi}{2} - \cos^{-1} \nu = \sin^{-1} \nu$
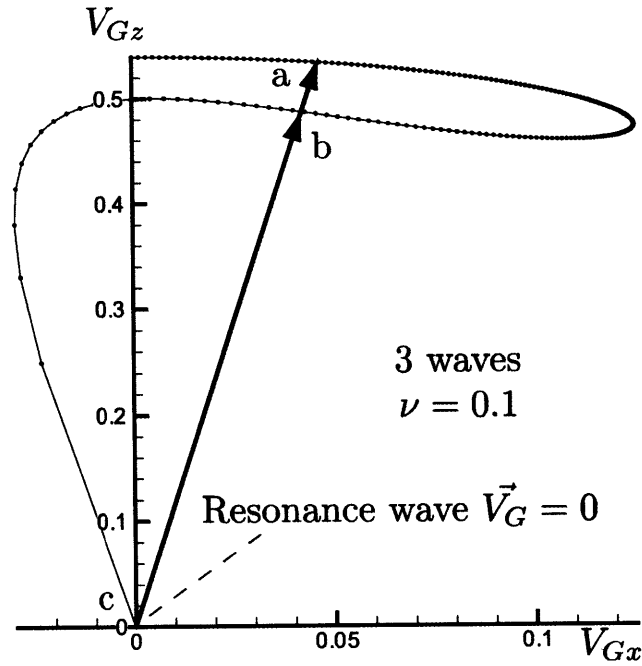
Figure 3-29: Region 3 $\vec{V_G}$ graph, $\nu = 0.1$ (on the resonance cone)

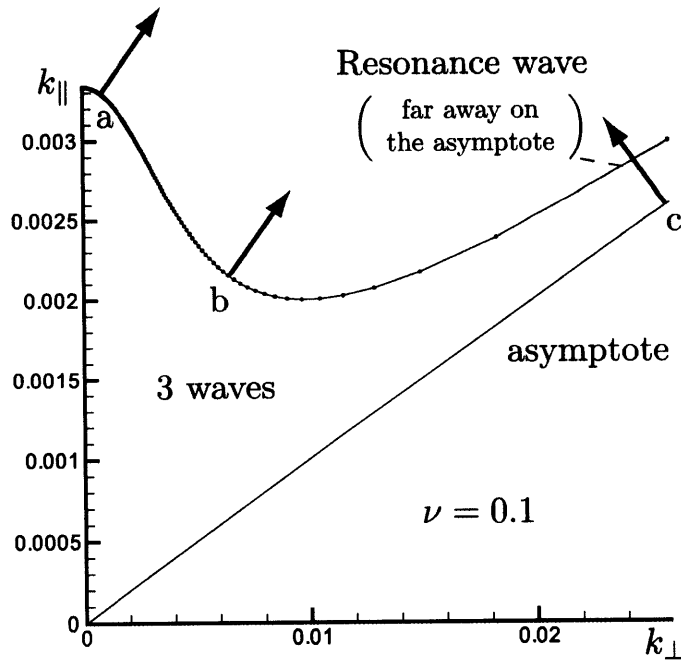Figure 3-30: Region 3 $\vec{k}$ tip graph, $\nu = 0.1$ (on the resonance cone)
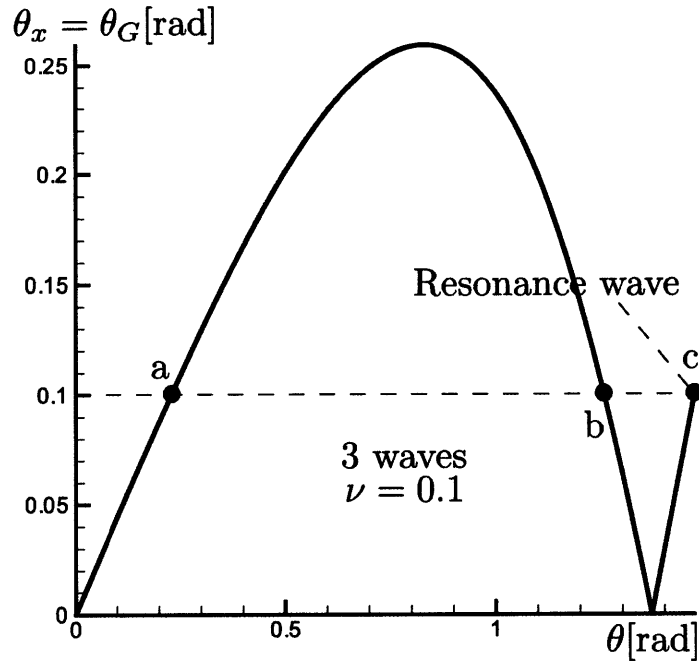
Figure 3-31: Region 3 θ vs θ_x graph, $\nu = 0.1$ (on the resonance cone)

In region 4, where $\sin^{-1} \nu < \theta_x < \cos^{-1} \dfrac{4\left(1-\nu^2\right)}{3\sqrt{2(1-\nu^2)-2\nu\sqrt{\frac{1-\nu^2}{3}}}}$, two waves propagate as in Fig.(3-32), Fig.(3-33), and Fig.(3-34). These waves have $\phi = \phi_x$.
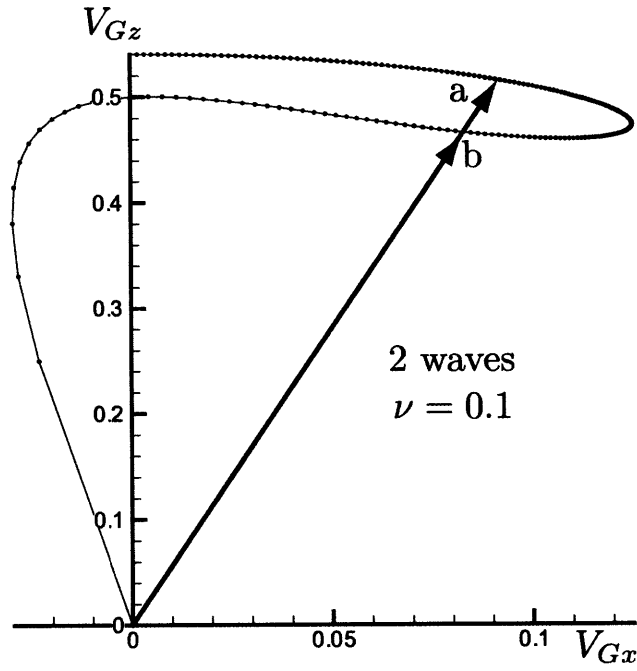
Figure 3-32: Region 4 $\vec{V_G}$ graph, $\nu = 0.1$ (outside resonance cone, but within propagation cone)
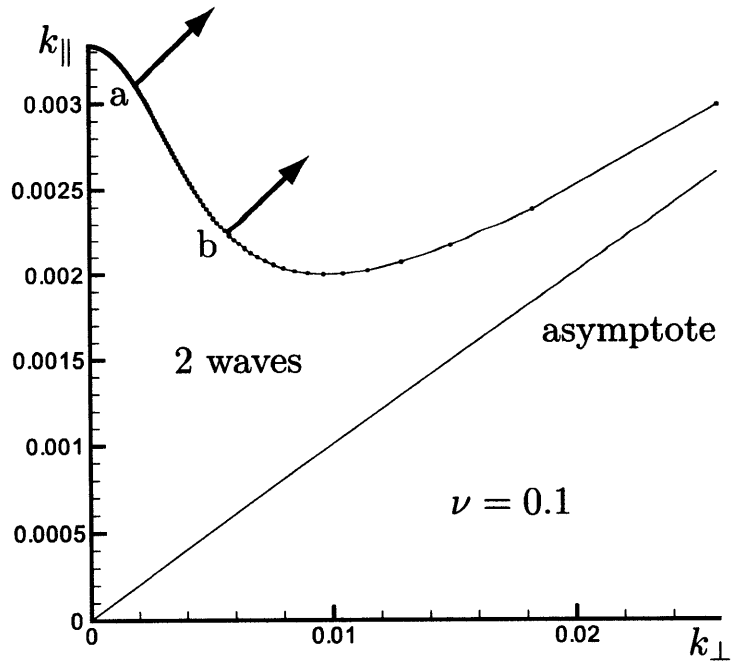
Figure 3-33: Region 4 $\vec{k}$ tip graph, $\nu = 0.1$ (outside resonance cone, but within propagation cone)
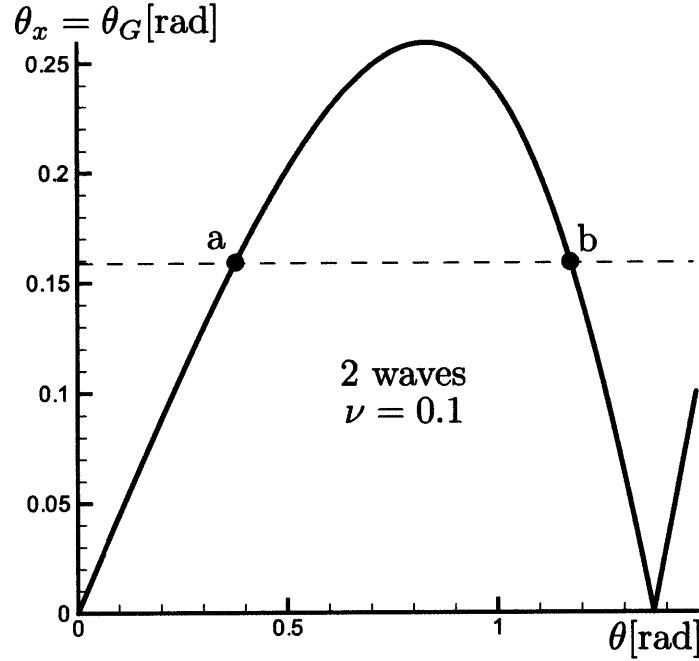
Figure 3-34: Region 4 θ vs θ_x graph, $\nu = 0.1$ (outside resonance cone, but within propagation cone)

On the cone where $\theta_x = \theta_{x\text{MAX}}$, only one wave propagates as in Fig.(3-35), Fig.(3-36), and Fig.(3-37). θ_G reaches its maximum and no wave can propagate in the region where $\theta_x > \theta_{x\text{MAX}}$. From Fig.(3-37), $\frac{\partial^2 \Phi}{\partial \theta^2} = 0$ on this point. From Eq.(3.13), this corresponds to

$$\cos \theta = \nu + \sqrt{\frac{1 - \nu^2}{3}} \tag{3.24}$$

From Eq.(3.23),

$$\theta_G = \cos^{-1} \frac{4(1 - \nu^2)}{3\sqrt{2(1 - \nu^2) - 2\nu\sqrt{\frac{1-\nu^2}{3}}}}$$

$$\xrightarrow[\nu \to 0]{} \cos^{-1} \frac{2\sqrt{2}}{3} = 0.3398 \text{rad} = 19.47° \tag{3.25}$$

65
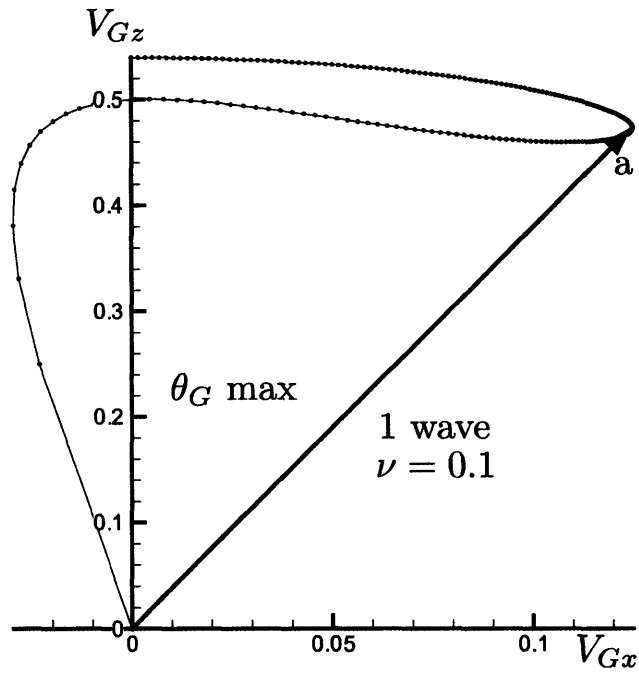
Figure 3-35: Region 5 $\vec{V}_G$ graph, $\nu = 0.1$ (on the edge of the propagation cone)
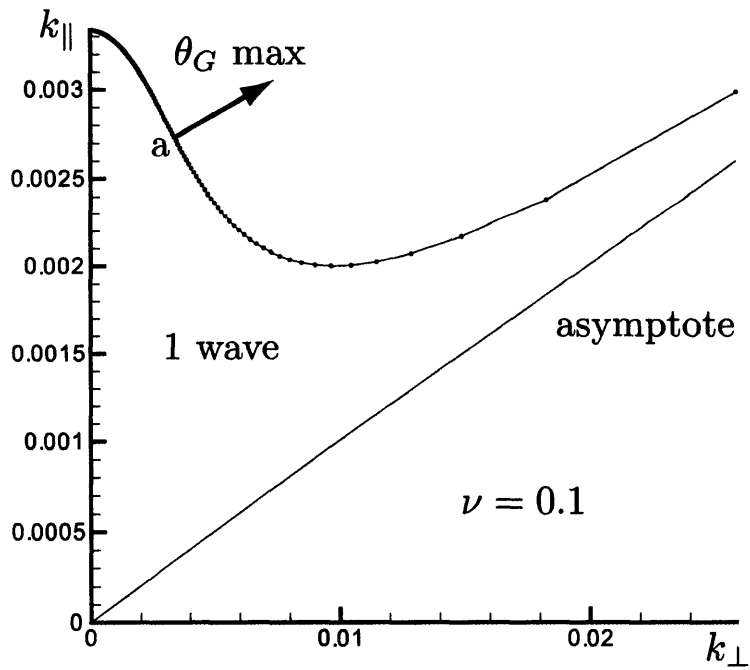
Figure 3-36: Region 5 $\vec{k}$ tip graph, $\nu = 0.1$ (on the edge of the propagation cone)
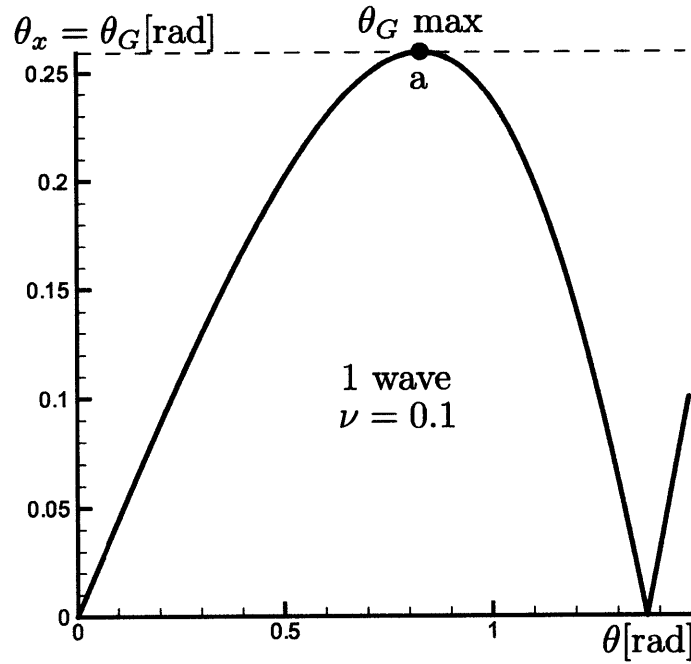
Figure 3-37: Region 5 θ vs θ_x graph, $\nu = 0.1$ (on the edge of the propagation cone)

3.3.2 Range 2: $\sqrt{\frac{1}{28}} \leq \nu \leq 0.5$

Now, consider the wave propagation in Range 2 ($\sqrt{\frac{1}{28}} \leq \nu \leq 0.5$). First, if the observation point is on the $\hat{z}$ axis, which means $\theta_x = 0$, two waves propagate as in Fig.(3-38), Fig.(3-39), and Fig.(3-40) at $\phi = \phi_x$. This is just the same propagation as in Range 1.
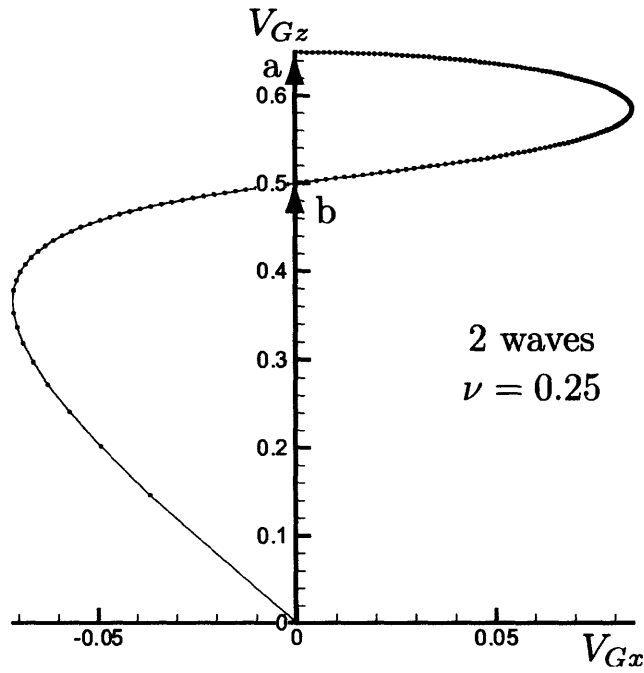
Figure 3-38: Region 1 $\vec{V}_G$ graph, $\nu = 0.25$ (Propagation along $\vec{B}_0$)
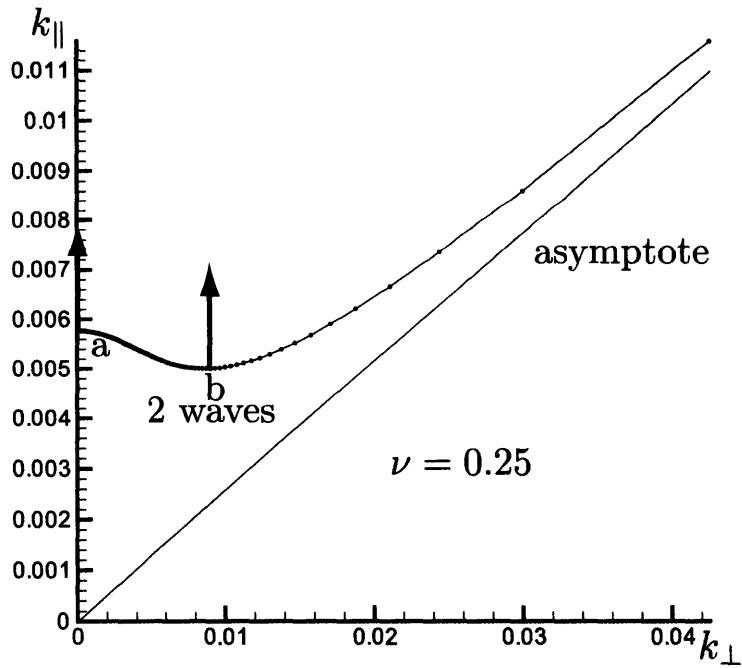
Figure 3-39: Region 1 $\vec{k}$ tip graph, $\nu = 0.25$ (Propagation along $\vec{B}_0$)
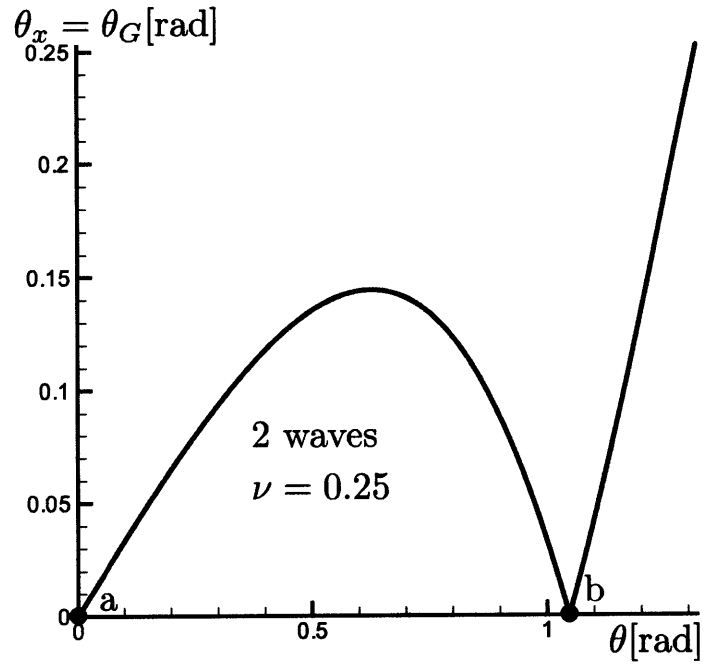
Figure 3-40: Region 1 θ vs θ_x graph, $\nu = 0.25$ (Propagation along $\vec{B_0}$)

In region 2, where $0 < \theta_x < \theta_{xMAX}$, in the same way as in Range 1 again, three waves propagate as in Fig.(3-41), Fig.(3-42), and Fig.(3-43). Two waves have $\phi = \phi_x$ and one wave has $\phi = \pi + \phi_x$, but these three waves have $\theta = \theta_G = \theta_x$.
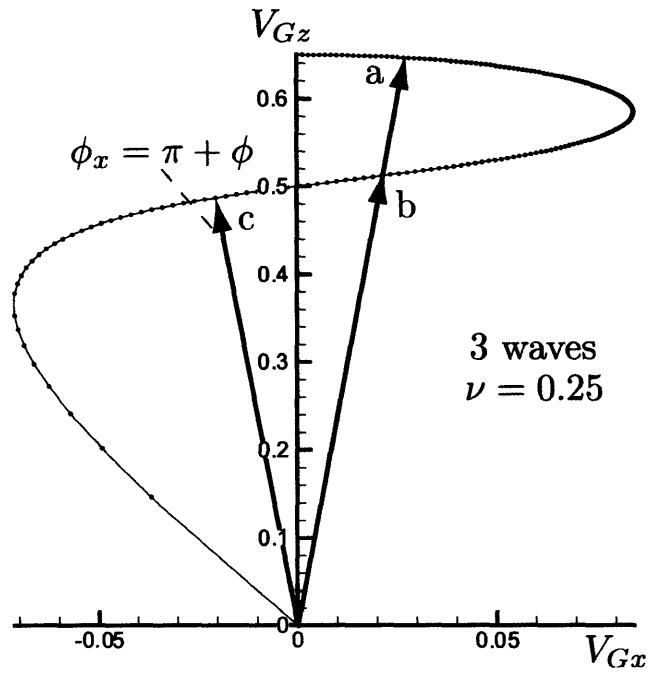
Figure 3-41: Region 2 $\vec{V_G}$ graph, $\nu = 0.25$ (very near $\vec{B_0}$)
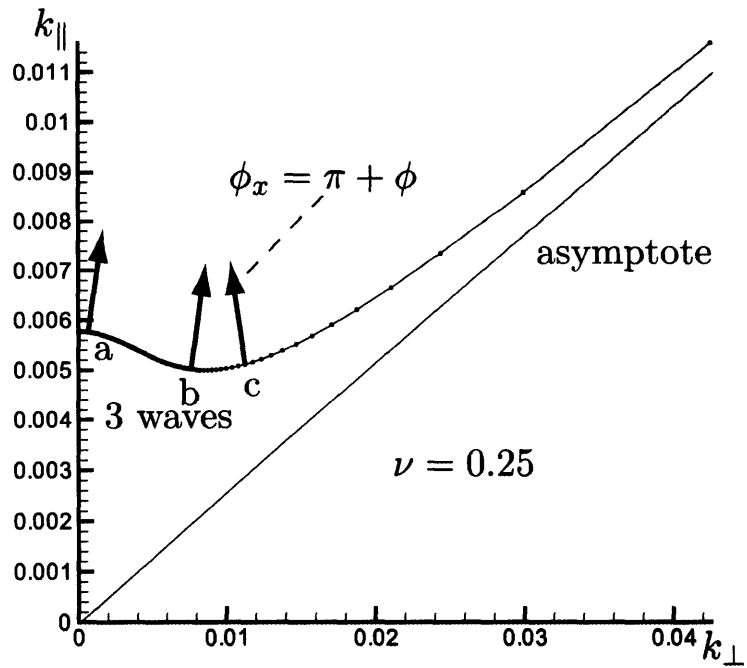
Figure 3-42: Region 2 $\vec{k}$ tip graph, $\nu = 0.25$ (very near $\vec{B_0}$)
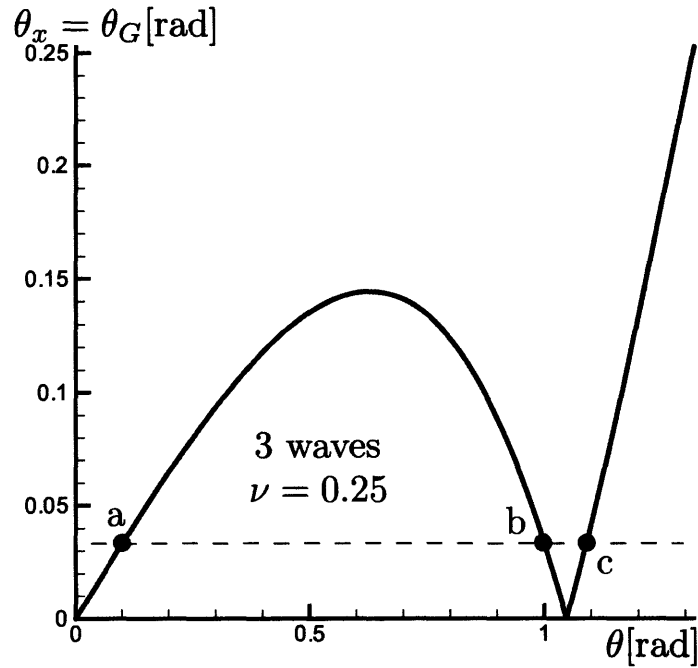
Figure 3-43: Region 2 θ vs θ_x graph, $\nu = 0.25$ (very near $\vec{B}_0$)

On the point where $\theta_x = \theta_{xMAX}$, two waves propagate. One of these waves is on the inflection point as in Fig.(3-44), Fig.(3-45), and Fig.(3-46). θ_x on the inflection point is smaller than θ_x on the resonance point. Only one wave can propagate outside of this inflection point θ_x.
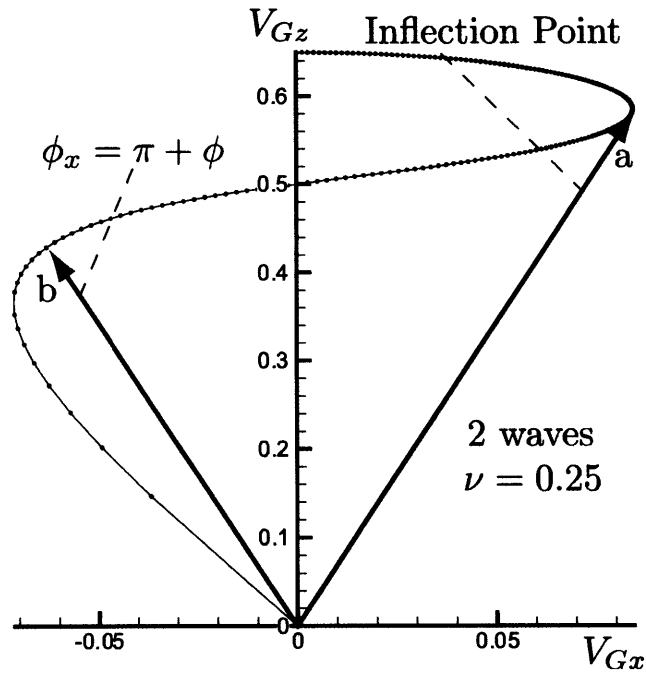
Figure 3-44: Region 3 $\vec{V}_G$ graph, $\nu = 0.25$ (on the resonance cone)
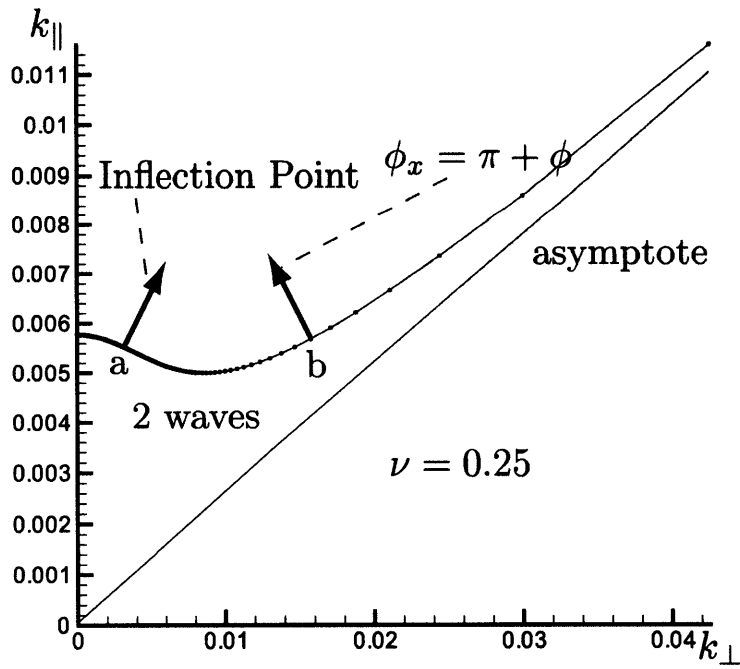
Figure 3-45: Region 3 $\vec{k}$ tip graph, $\nu = 0.25$ (on the resonance cone)

72
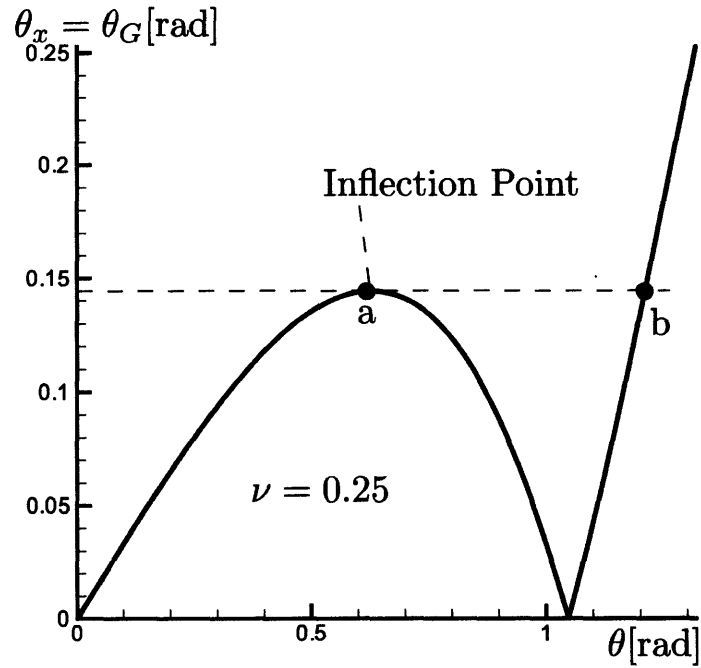
Figure 3-46: Region 3 θ vs θ_x graph, $\nu = 0.25$ (on the resonance cone)

In region 4, where $\theta_{xMAX} < \theta_x < \sin^{-1}\nu$, only one wave propagates as in Fig.(3-47), Fig.(3-48), and Fig.(3-49). This wave has $\phi = \pi + \phi_x$.
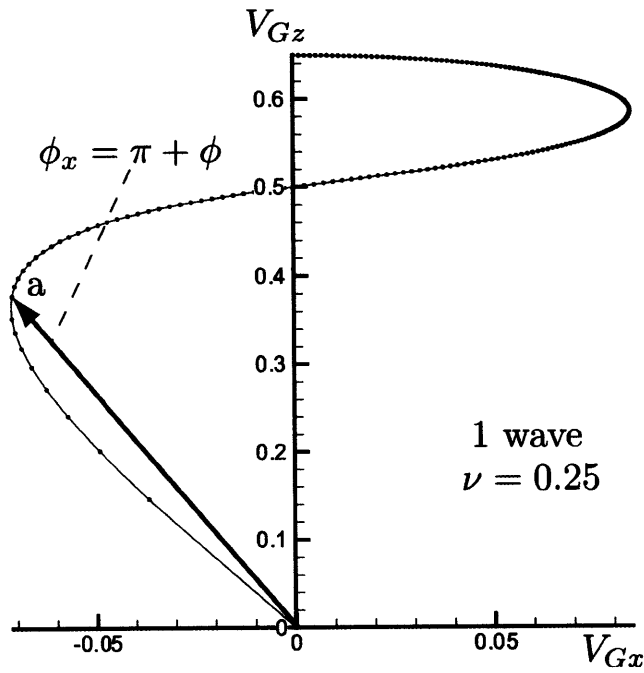
Figure 3-47: Region 4 $\vec{V}_G$ graph, $\nu = 0.25$ (inside the resonance cone)
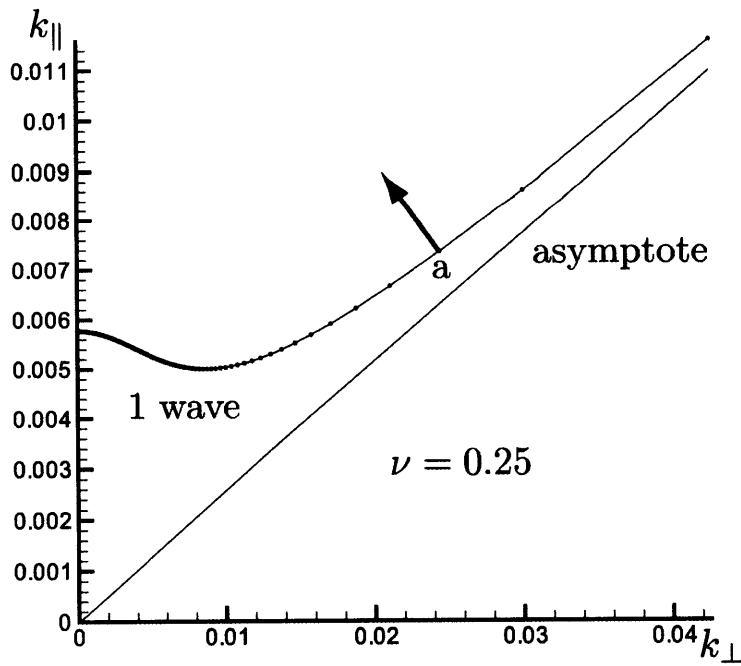
Figure 3-48: Region 4 $\vec{k}$ tip graph, $\nu = 0.25$ (inside resonance cone)
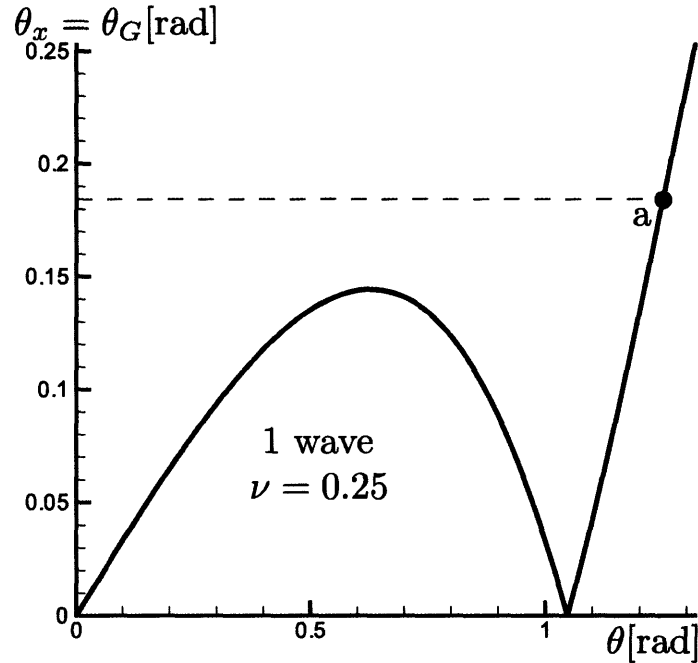
Figure 3-49: Region 4 θ vs θ_x graph, $\nu = 0.25$ (inside resonance cone)

On the cone where $\theta_x = \sin^{-1} \nu$, there is only one wave as in Fig.(3-50), Fig.(3-51), and Fig.(3-52) and this wave is the resonance wave.

3.3.3   Range 3: $\nu \geq 0.5$

For Range 3($\nu \geq 0.5$), only one wave propagates as in Fig.(3-53), Fig.(3-54), and Fig.(3-55). On the point where $\theta_x = \sin^{-1} \nu$, the wave becomes resonant wave as in Fig.(3-56), Fig.(3-57), and Fig.(3-58).
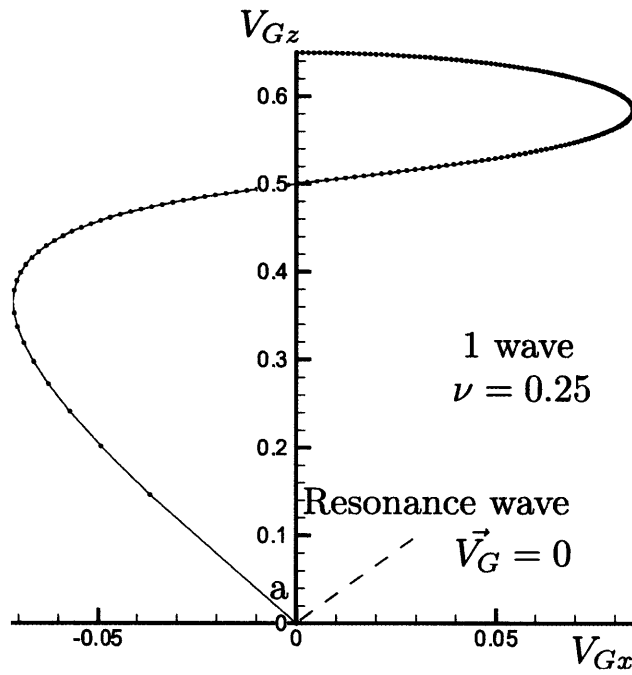
Figure 3-50: Region 5 $\vec{V_G}$ graph, $\nu = 0.25$ (on the edge of the propagation cone)
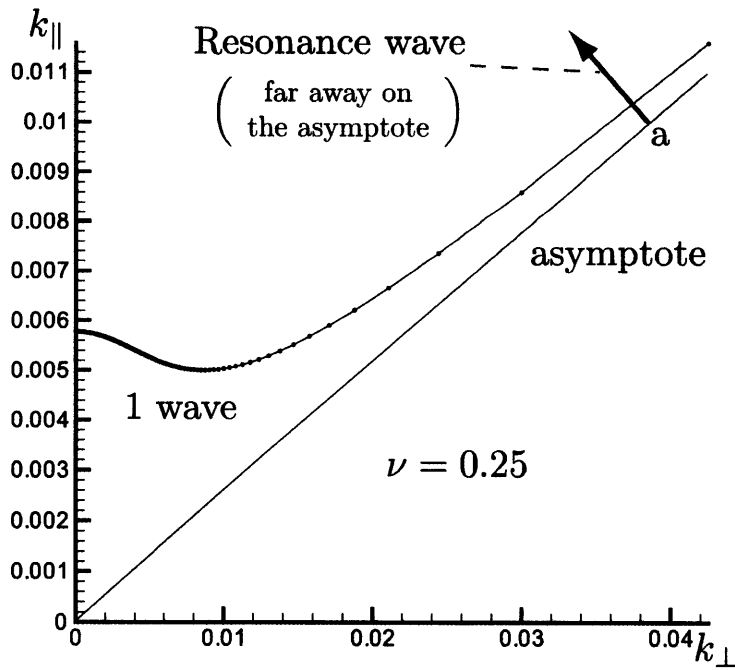
Figure 3-51: Region 5 $\vec{k}$ tip graph, $\nu = 0.25$ (on the edge of the propagation cone)
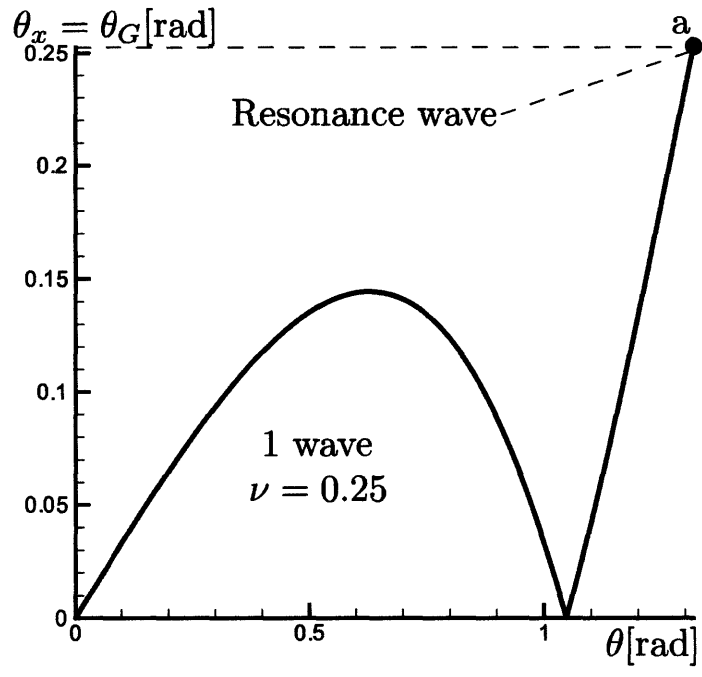
Figure 3-52: Region 5 θ vs θ_x graph, $\nu = 0.25$ (on the edge of the propagation cone)
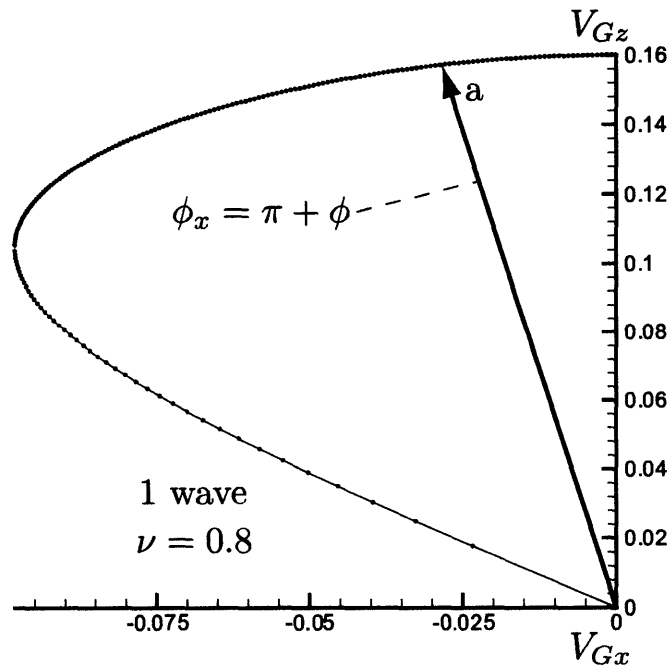
Figure 3-53: $\vec{V}_G$ graph, $\nu = 0.8$
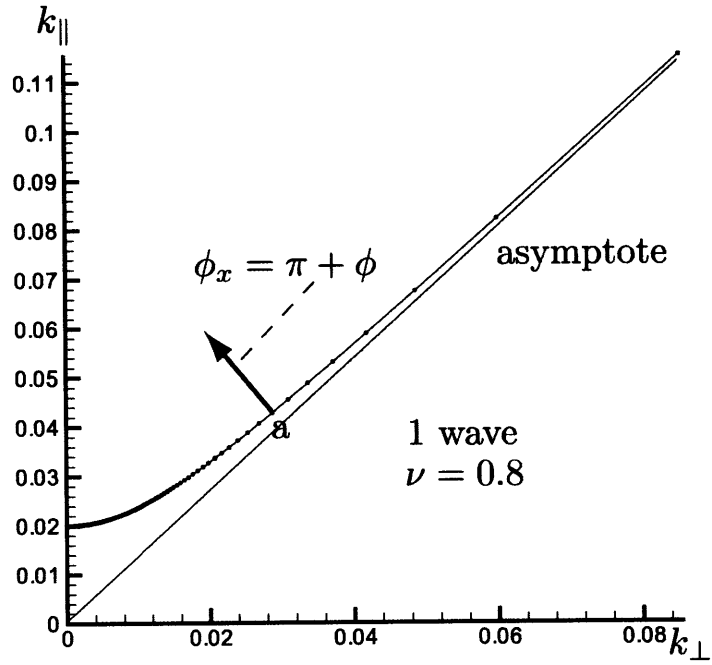
Figure 3-54: $\vec{k}$ tip graph, $\nu = 0.8$
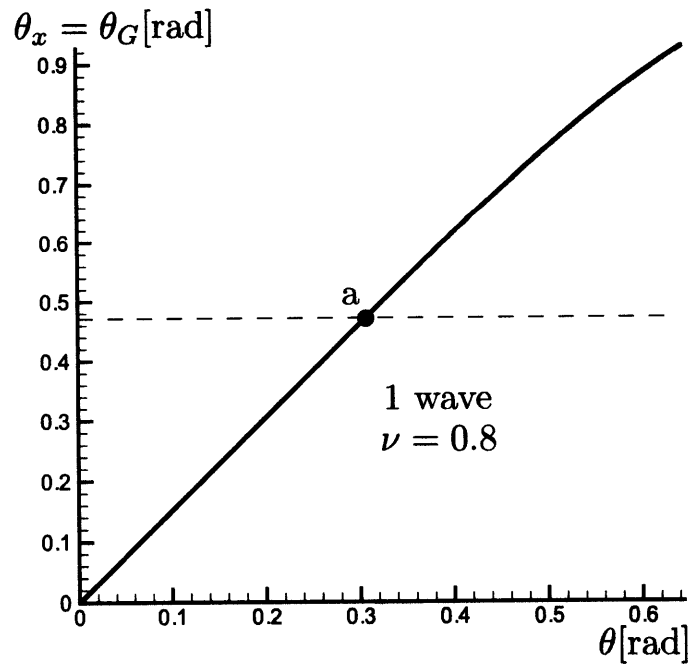
Figure 3-55: θ vs θ_x graph, $\nu = 0.8$

78
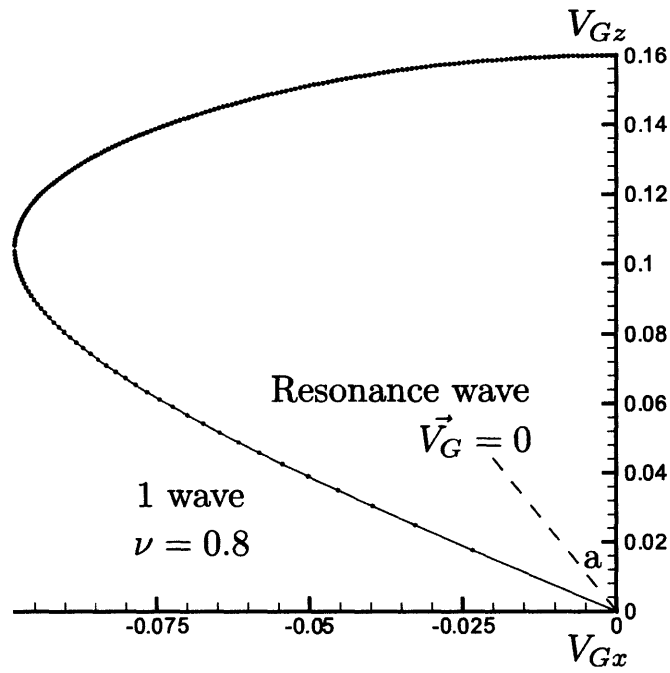
Figure 3-56: $\vec{V_G}$ graph, $\nu = 0.8$ (on the edge of the propagation cone)
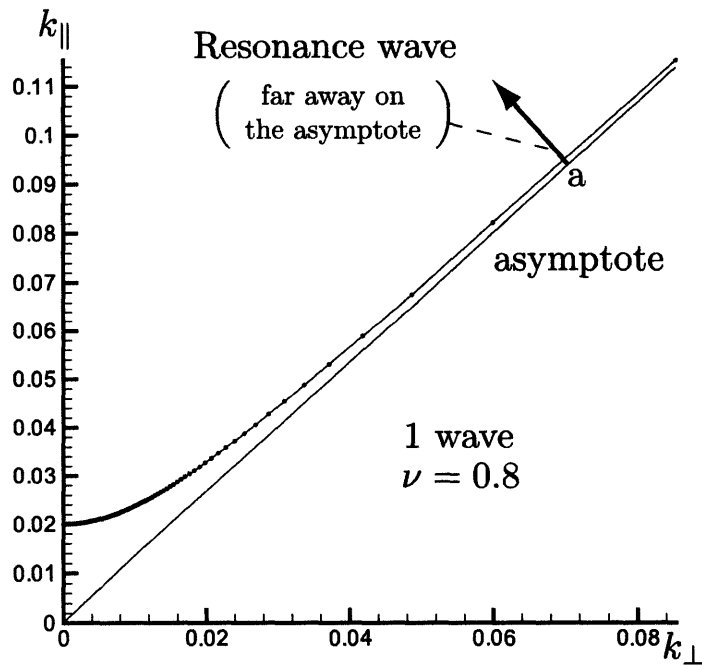
Figure 3-57: $\vec{k}$ tip graph, $\nu = 0.8$ (on the edge of the propagation cone)
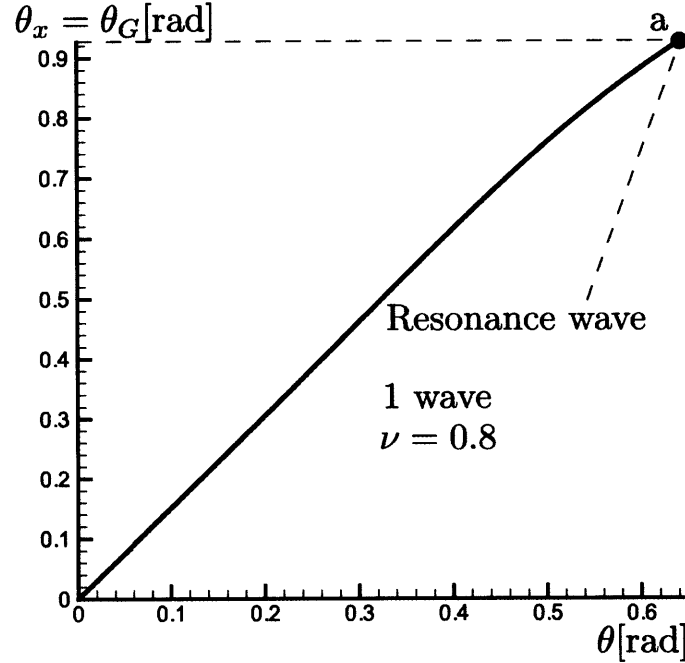
Figure 3-58: θ vs θ_x graph, $\nu = 0.8$ (on the edge of the propagation cone)

3.4 ϕ Integration Using Bessel's Function

For the antenna parallel to Earth's magnetic field ($\alpha = 0$), Bessel's functions can be used for an exact ϕ Integration. We use

$$\int_0^{2\pi} e^{-ix\cos(\phi-\phi_x)} = 2\pi J_0(x) \tag{3.26}$$

$$\int_0^{2\pi} \cos\phi e^{-ix\cos(\phi-\phi_x)} = -2\pi i \cos\phi_x J_1(x) \tag{3.27}$$

$$\int_0^{2\pi} \sin\phi e^{-ix\cos(\phi-\phi_x)} = -2\pi i \sin\phi_x J_1(x) \tag{3.28}$$

Notice the asymptotic behavior of these expressions: when $x \gg 1$, each of the above integrals contain mainly the contributions from ϕ values near ϕ_x and $\phi_x + \pi$. At other ϕ values, the rapid oscillations of the exponential produce cancellations.

80

The electric field made by the wave is then found to be

$$\vec{E}\,(\vec{r}) = \int_{\theta=0}^{\frac{\pi}{2}} -\frac{2\pi i}{\sigma_{ce}} \quad \frac{\sqrt{\nu\,(\cos\theta - \nu)}}{4\cos\theta l}\frac{4Il}{(2\pi)^3}\frac{1 - \cos\left(\frac{k_\parallel L}{2}\right)}{\left(k_\parallel L\right)^2}\left(\frac{K}{l}\right)^2 \sin\theta e^{-iK\frac{r}{l}\cos\theta\cos\theta_x}$$

$$\begin{bmatrix} -2\pi i J_1\,(x)\,K^2\sin\theta\cos\theta\,(\sin\phi_x - p\cos\phi_x) \\ 2\pi i J_1\,(x)\,K^2\sin\theta\cos\theta\,(p\sin\phi_x + \cos\phi_x) \\ 2\pi J_0\,(x)\,\{-pK^2\cos^2\theta + i\nu\,(1+K^2)\} \end{bmatrix} d\theta \qquad (3.29)$$

where

$$x = \frac{r}{l}\sqrt{\nu}\,\frac{\sin\theta\sin\theta_x}{\sqrt{\cos\theta - \nu}} \qquad (3.30)$$

Also the magnetic field made by the wave is found to be

$$\vec{B}\,(\vec{r}) = \int_{\theta=0}^{\frac{\pi}{2}} -\frac{2\pi i}{\sigma_{ce}\nu\omega_{ce}} \quad \frac{\sqrt{\nu\,(\cos\theta - \nu)}}{4\cos\theta l}\frac{4Il}{(2\pi)^3}\frac{1 - \cos\left(\frac{k_\parallel L}{2}\right)}{\left(k_\parallel L\right)^2}\left(\frac{K}{l}\right)^3 \sin\theta e^{-iK\frac{r}{l}\cos\theta\cos\theta_x}$$

$$\begin{bmatrix} -2\pi i J_1\,(x)\,K^2\sin\theta\cos\theta\,(\sin\phi_x - p\cos\phi_x) \\ 2\pi i J_1\,(x)\,K^2\sin\theta\cos\theta\,(p\sin\phi_x + \cos\phi_x) \\ 2\pi J_0\,(x)\,\{-pK^2\cos^2\theta + i\nu\,(1+K^2)\} \end{bmatrix} d\theta \qquad (3.31)$$

If $x \gg 1$, we can use the asymptotic expansions

$$J_0\,(x) \simeq \sqrt{\frac{2}{\pi x}}\cos\left(x - \frac{\pi}{4}\right) = \sqrt{\frac{2}{\pi x}}\frac{1}{2}\left[\exp\left\{i\left(x - \frac{\pi}{4}\right)\right\} + \exp\left\{-i\left(x - \frac{\pi}{4}\right)\right\}\right]$$
$$(3.32)$$

$$J_1\,(x) \simeq \sqrt{\frac{2}{\pi x}}\cos\left(x - \frac{3\pi}{4}\right) = \sqrt{\frac{2}{\pi x}}\frac{1}{2}\left[\exp\left\{i\left(x - \frac{3\pi}{4}\right)\right\} + \exp\left\{-i\left(x - \frac{3\pi}{4}\right)\right\}\right]$$
$$(3.33)$$

Then, from Eq.(3.32)

$$\int_{\theta=0}^{\frac{\pi}{2}} 2\pi J_0\left(x\right) e^{-i\frac{r}{l}\sqrt{\nu}\frac{\cos\theta\cos\theta_x}{\sqrt{\cos\theta-\nu}}} d\theta$$

$$= \int_{\theta=0}^{\frac{\pi}{2}} 2\pi\sqrt{\frac{1}{2\pi x}}\left[e^{-i\frac{\pi}{4}}e^{-i\frac{r}{l}\sqrt{\nu}\frac{-\sin\theta\sin\theta_x+\cos\theta\cos\theta_x}{\sqrt{\cos\theta-\nu}}} + e^{i\frac{\pi}{4}}e^{-i\frac{r}{l}\sqrt{\nu}\frac{\sin\theta\sin\theta_x+\cos\theta\cos\theta_x}{\sqrt{\cos\theta-\nu}}}\right]$$

$$= \sum_{\mathrm{StationaryPoints}}\left(\frac{1}{\sqrt{2}}+\frac{i}{\sqrt{2}}\right)\sqrt{\frac{1}{2\pi x}}e^{-i\frac{r}{l}\sqrt{\nu}\Phi(\theta_s,\ \phi_x)}\sqrt{\frac{\pi}{i\frac{r}{l}\frac{\sqrt{\nu}}{2}\frac{\partial^2\Phi}{\partial\theta^2}}}2\pi$$

$$+ \left(\frac{1}{\sqrt{2}}-\frac{i}{\sqrt{2}}\right)\sqrt{\frac{1}{2\pi x}}e^{-i\frac{r}{l}\sqrt{\nu}\Phi(\theta_s,\ \phi_x+\pi)}\sqrt{\frac{\pi}{i\frac{r}{l}\frac{\sqrt{\nu}}{2}\frac{\partial^2\Phi}{\partial\theta^2}}}2\pi$$

$$= \sum_{\mathrm{StationaryPoints}}\frac{\pi}{i\frac{r}{l}\frac{\sqrt{\nu}}{2}\sqrt{\frac{\partial^2\Phi}{\partial\theta^2}\frac{\partial^2\Phi}{\partial\phi^2}}}e^{-i\frac{r}{l}\sqrt{\nu}\Phi(\theta_s,\ \phi_s)} \tag{3.34}$$

where we used

$$x = -\left.\frac{\partial^2\Phi}{\partial\phi^2}\right|_{\phi_x}\frac{r}{l}\sqrt{\nu} = \left.\frac{\partial^2\Phi}{\partial\phi^2}\right|_{\phi_x+\pi}\frac{r}{l}\sqrt{\nu}$$

$$\frac{1}{\sqrt{2}}+\frac{i}{\sqrt{2}} = \frac{1}{\sqrt{-i}},\quad \frac{1}{\sqrt{2}}-\frac{i}{\sqrt{2}} = -\frac{1}{\sqrt{i}} \tag{3.35}$$

In the same way, from Eq.(3.33)

$$\int_{\theta=0}^{\frac{\pi}{2}} 2\pi i J_1\left(x\right) e^{-i\frac{r}{l}\sqrt{\nu}\frac{\cos\theta\cos\theta_x}{\sqrt{\cos\theta-\nu}}} d\theta$$

$$= \sum_{\mathrm{StationaryPoints}}\frac{\pi}{i\frac{r}{l}\frac{\sqrt{\nu}}{2}\sqrt{\frac{\partial^2\Phi}{\partial\theta^2}\frac{\partial^2\Phi}{\partial\phi^2}}}e^{-i\frac{r}{l}\sqrt{\nu}\Phi(\theta_s,\ \phi_s)} \tag{3.36}$$

Comparing with Eq.(3.15) and Eq.(3.17), we can see that the wave field calculated using the (θ,ϕ) Stationary Phase Method and using the θ Stationary Phase Method with ϕ integration using Bessel's functions are mathematically identical, as long as $\frac{r}{l}\sqrt{\nu}\frac{\sin\theta\sin\theta_x}{\sqrt{\cos\theta-\nu}} \gg 1$. Clearly, this inequality is violated and the stationary phase method cannot be used for propagation near $\vec{B}_0$ ($\theta_x \ll 1$), so that region needs to be examined separately.

3.5 Propagation near $\vec{B}_0$

If the observation point is very near the magnetic field line from the antenna, there is an interesting phenomenon about wave propagation. For this analysis, θ_x in Fig.(3-59) needs to be very small. The Stationary point should satisfy Eq.(3.9) and Eq.(3.11).
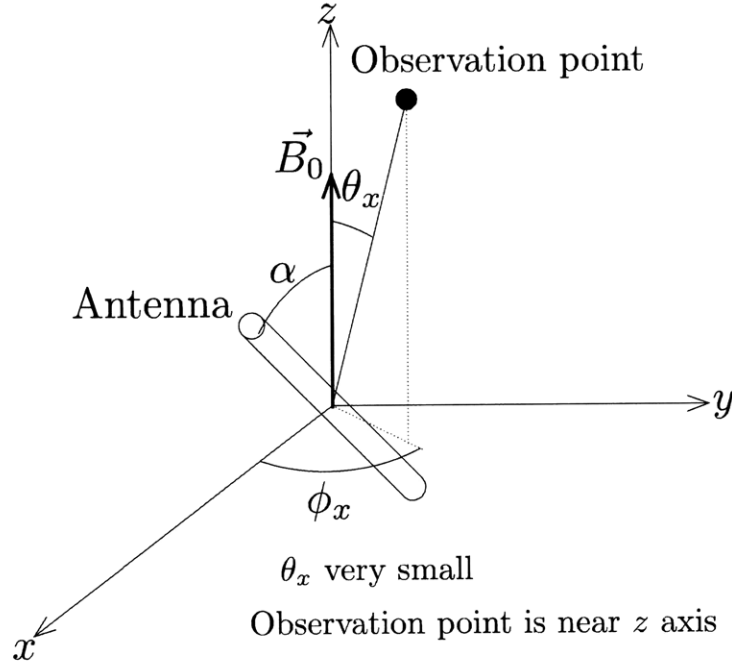
Figure 3-59: Observation point near $\vec{B}$ line

However, if $\theta_x \simeq 0$, $\frac{\partial \Phi}{\partial \phi} \simeq 0$ for any ϕ. Then, the oscillation frequency of the integrand in Eq.(3.5) with respect to ϕ is not high enough to produce cancellations in the integration. A modified mathematical procedure is needed for calculating the wave field at observation points very near the magnetic field. If the antenna is set parallel to Earth's magnetic field, ϕ integration can be done with Bessel's functions as in Eq.(3.29) and Eq.(3.31). If x in the Bessel's functions is not large ($x \simeq 1$ that is, $\theta_x \simeq \frac{l}{r}$) the oscillation of Bessel's functions are not high compared with the exponential term, and they can be moved out of the integral. With K integration using residue theorem, the phase of the exponential term in the integrand is

$$\Phi' = \frac{\cos\theta \cos\theta_x}{\sqrt{\cos\theta - \nu}} \tag{3.37}$$

83

and with this phase,

$$\frac{\partial \Phi'}{\partial \theta} = \frac{\nu \cos \theta_x \sin \theta - \frac{1}{2} \cos \theta_x \sin \theta \cos \theta}{(\cos \theta - \nu)^{\frac{3}{2}}} \tag{3.38}$$

Then, the stationary points $\left(\frac{\partial \Phi'}{\partial \theta} = 0\right)$ are $\theta = 0$ or $\cos^{-1} 2\nu$. On these stationary points,

$$\frac{\partial^2 \Phi'}{\partial \theta^2} = \frac{\cos \theta_x \left(\nu \cos \theta - \frac{\cos 2\theta}{2}\right)}{(\cos \theta - \nu)^{\frac{3}{2}}} \tag{3.39}$$

With the Stationary Phase Method for θ integration, we obtain

$$\vec{E}(\vec{r}) = \sum_{\text{Stationary Points}} -\frac{2\pi i}{\sigma_{ce}} \quad \frac{\sqrt{\nu(\cos\theta-\nu)}}{4\cos\theta l} \frac{4Il}{(2\pi)^3} \frac{1-\cos\left(\frac{k_\| L}{2}\right)}{\left(k_\| L\right)^2} \left(\frac{K}{l}\right)^2 \sin\theta \sqrt{\frac{\pi}{i\frac{r}{l}\frac{\sqrt{\nu}}{2}\frac{\partial^2\Phi'}{\partial\theta^2}}}$$

$$\begin{bmatrix} -2\pi i J_1(x) K^2 \sin\theta \cos\theta (\sin\phi_x - p\cos\phi_x) \\ 2\pi i J_1(x) K^2 \sin\theta \cos\theta (p\sin\phi_x + \cos\phi_x) \\ 2\pi J_0(x) \{-pK^2 \cos^2\theta + i\nu(1+K^2)\} \end{bmatrix} d\theta \tag{3.40}$$

where $x = \frac{r}{l}\sqrt{\nu}\frac{\sin\theta\sin\theta_x}{\sqrt{\cos\theta-\nu}}$. Also Magnetic field made by the wave is found to be

$$\vec{B}(\vec{r}) = \int_{\theta=0}^{\frac{\pi}{2}} -\frac{2\pi i}{\sigma_{ce}\nu\omega_{ce}} \quad \frac{\sqrt{\nu(\cos\theta-\nu)}}{4\cos\theta l} \frac{4Il}{(2\pi)^3} \frac{1-\cos\left(\frac{k_\| L}{2}\right)}{\left(k_\| L\right)^2} \left(\frac{K}{l}\right)^3 \sin\theta \sqrt{\frac{\pi}{i\frac{r}{l}\frac{\sqrt{\nu}}{2}\frac{\partial^2\Phi'}{\partial\theta^2}}}$$

$$\begin{bmatrix} -2\pi i J_1(x) K^2 \sin\theta \cos\theta (\sin\phi_x - p\cos\phi_x) \\ 2\pi i J_1(x) K^2 \sin\theta \cos\theta (p\sin\phi_x + \cos\phi_x) \\ 2\pi J_0(x) \{-pK^2 \cos^2\theta + i\nu(1+K^2)\} \end{bmatrix} d\theta \tag{3.41}$$

Because of the $\sin\theta$ term in Eq.(3.40) and Eq.(3.41), $\theta = 0$ has no contribution to the integral, so we only have to include a stationary point $\theta = \cos^{-1} 2\nu$. This mathematical procedure should be used only when $x \leq 1$ $\left(\theta_x \leq \frac{l}{r}\right)$. This boundary is a thin cylinder along Earth's magnetic field on the antenna as in Fig.(fig:NearBRegion.eps). This cylinder is very thin in our case ($l \simeq 50\,\text{m}$, $r \simeq 1000\,\text{km}$) and the radiation in this cylinder has small influence on radiation power integration.
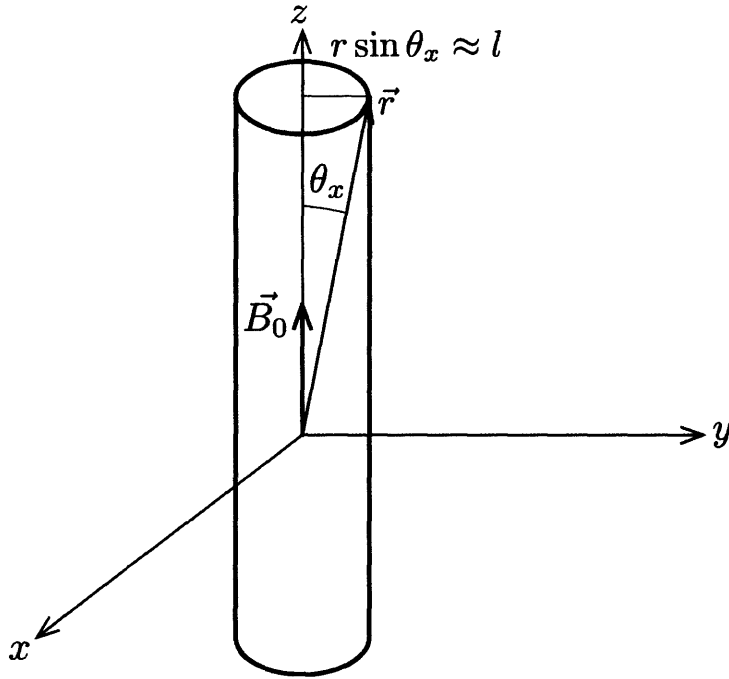
Figure 3-60: A "cylinder" along $\vec{B}_0$ line

This mathematical procedure is for the antenna parallel to Earth's magnetic field and the ϕ integration for the antenna perpendicular to Earth's magnetic field is much more complicated because $k_{\parallel}$ in the antenna term includes ϕ. However we judged that a more refined mathematical procedure for the antenna perpendicular to Earth's magnetic field is not necessary for the radiation power integration because the contribution of the near $\vec{B}_0$ to the radiation power integration is small. We compared the result of the radiation power integration for the parallel antenna using this refined mathematical procedure and without this procedure and found that the difference is small.

Chapter 4

Radiation Pattern Analysis

4.1 Radiation Pattern

With the calculation methods shown in Chapter 2 and Chapter 3, the radiation fields $\vec{E}$ and $\vec{B}$ can be acquired. Fig.(4-1) through Fig.(4-6) are the plots of these radiation fields for some representative cases. Fig.(4-7) and Fig.(4-8) give the value of the energy flux away from the antenna. The energy flux is the $\vec{r}$ component of the time-averaged Poynting's vector. The time-averaged Poynting's vector $\left\langle \vec{\vec{S}} \right\rangle$ can be calculated as follows[15]

$$\left\langle \vec{\vec{S}} \right\rangle = \mathrm{Re}\left(\frac{\vec{E} \times \vec{B}^*}{2\mu_0} \right) \qquad (4.1)$$

The parameters in this calculation are $\nu = 0.1$, L(antenna length)$= 100$m, n_e(electron density)$= 10^{10}$m^{-3}, I(antenna current)$= 10A$, B_0(Earth's magnetic field)$= 10^{-5}$T, α(antenna angle, Section 2.5)$= \frac{\pi}{2}$. There are three intense radiation zones (conical lobes), and they are Near $\vec{B}_0$ zone ($\theta_x \simeq o$)(see Section3.5), Resonance point zone ($\theta_x \simeq 0.100$) and Inflection point zone as in Fig.(4-8) ($\theta_x \simeq 0.259$). The radiation in the Inflection point zone is weak compared to the other two intense lobes. For θ_x other than these special values, we see rapid spatial oscillations of the field values. and to a lesser extent, of the power flux as well. It can be shown that these so-called "interference patterns" are due to interactions between $\vec{E}$ from one of the waves observed at θ_x and $\vec{B}$ from one of the other waves.
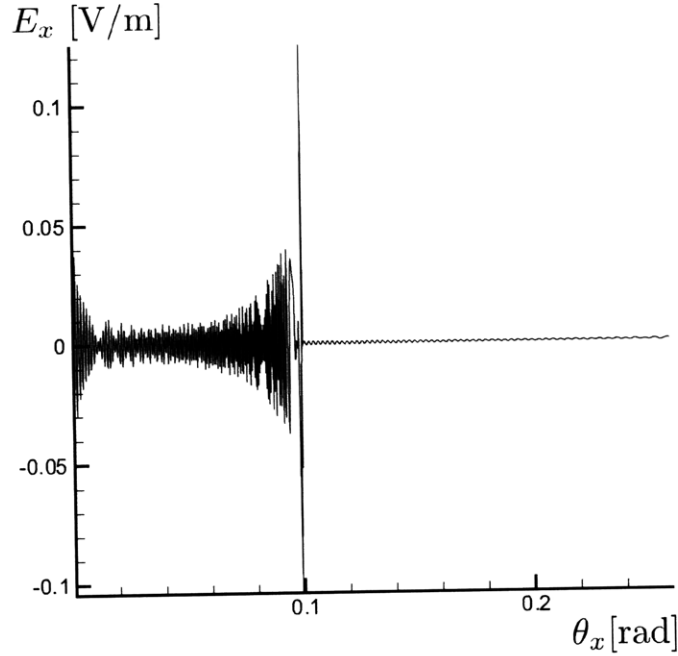
87

Figure 4-1: x-component of $\vec{E}$ ($\nu = 0.1$, $\alpha = \frac{\pi}{2}$) (the antenna direction)

The radiation pattern varies with calculation parameters. Fig.(4-9) shows the radiation pattern (Poynting's vector) for $\alpha = 0$ with the same parameters as the energy flux calculation for Fig.(4-7). For the $\alpha = 0$ case, the radiation in near-$\vec{B}_0$ direction is weaker than the near-resonance radiation, compared with the radiation pattern for $\alpha = \frac{\pi}{2}$. This is because the electromagnetic waves in the dipole antenna direction is weak.

Figs.(4-10) through (4-13) show the radiation pattern of perpendicular antenna and parallel antenna for $\nu = 0.25$ with the same parameters as the Energy flux calculation for Fig.(4-7). The near $\vec{B}_0$ point, the Resonance point and the Inflection point are shown in Figs.(4-11) and (4-13).

Figure 4-2: y-component of $\vec{E}$ ($\nu = 0.1$, $\alpha = \frac{\pi}{2}$) (direction perpendicular to $\vec{B}_0$ and to the antenna)
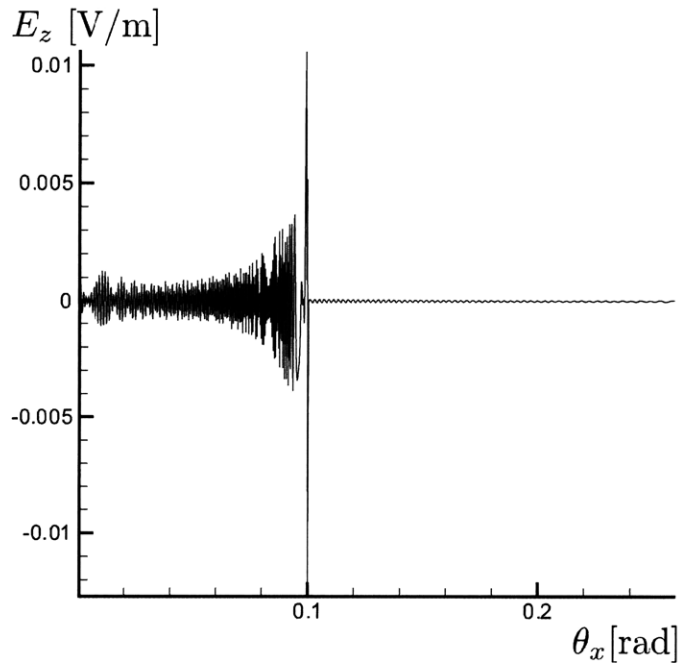
Figure 4-3: z-component of $\vec{E}$ ($\nu = 0.1$, $\alpha = \frac{\pi}{2}$) (direction of $\vec{B}_0$)

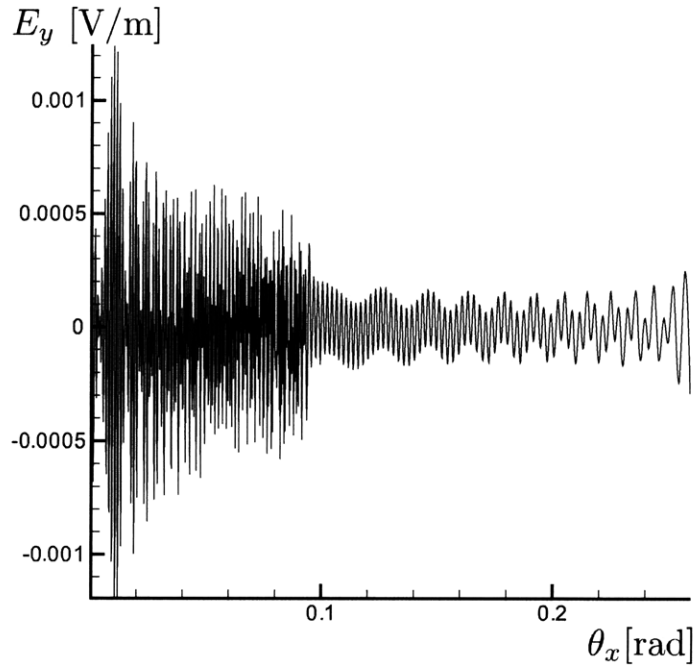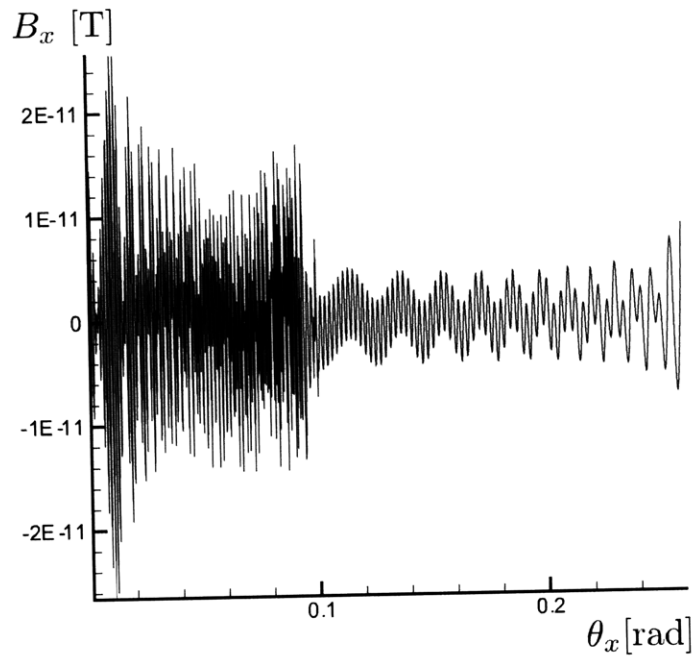Figure 4-4: x-component of $\vec{B}$ ($\nu = 0.1$, $\alpha = \frac{\pi}{2}$) (antenna direction)
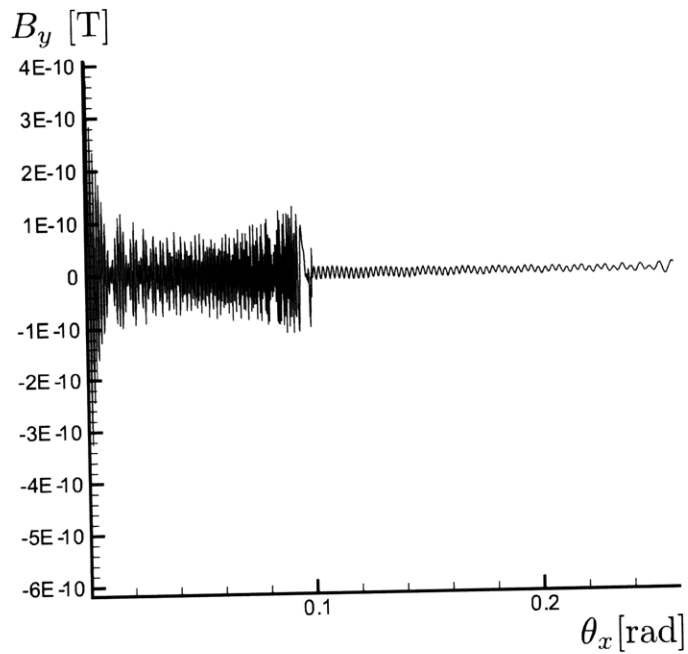
Figure 4-5: y-component of $\vec{B}$ ($\nu = 0.1$, $\alpha = \frac{\pi}{2}$) (direction perpendicular to $\vec{B}_0$ and to the antenna)
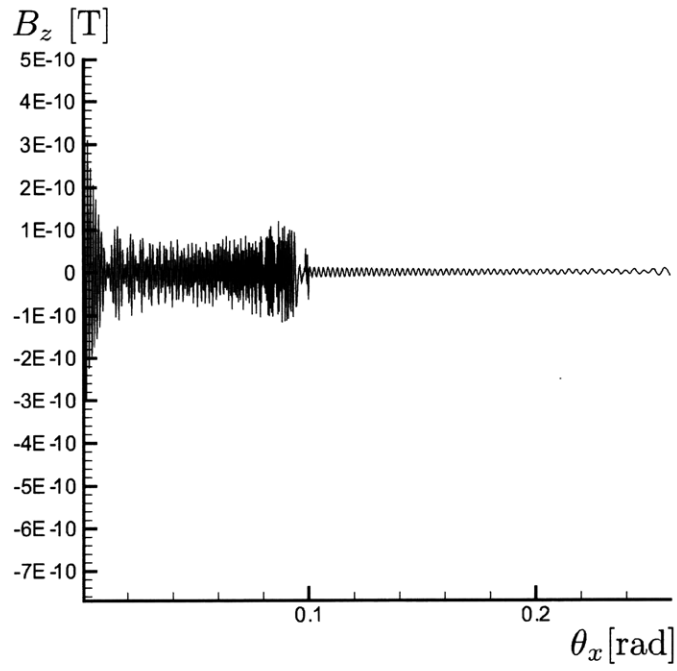
Figure 4-6: z-component of $\vec{B}$ ($\nu = 0.1$, $\alpha = \frac{\pi}{2}$) (direction of $\vec{B_0}$)
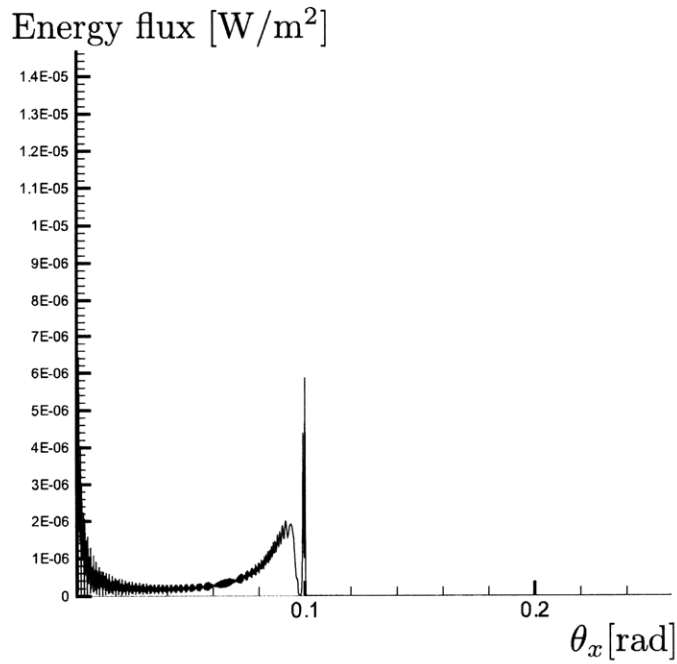
Figure 4-7: Energy flux ($\nu = 0.1$, $\alpha = \frac{\pi}{2}$)

91
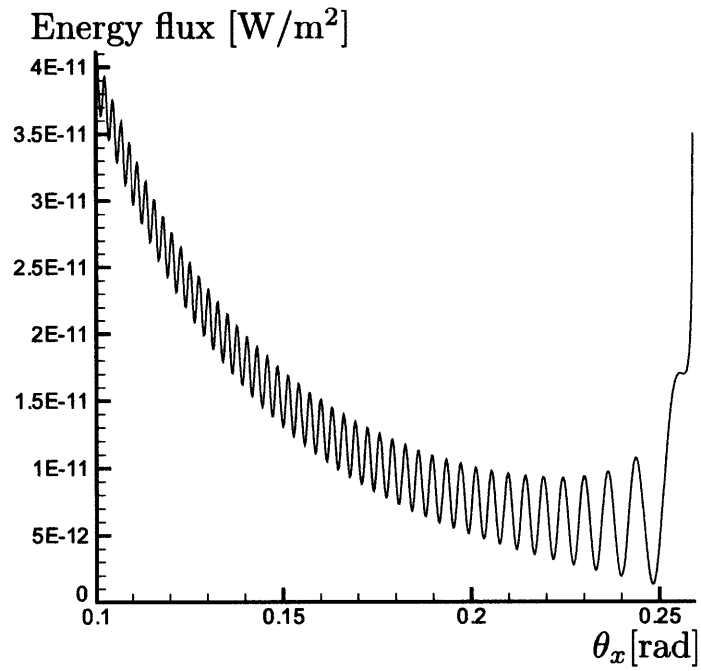
Figure 4-8: Zoomed view of the energy flux graph ($\nu = 0.1$, $\alpha = \frac{\pi}{2}$). Showing the resonance ($\theta_x = 0.1$) and the inflection point ($\theta_x = 0.259$)
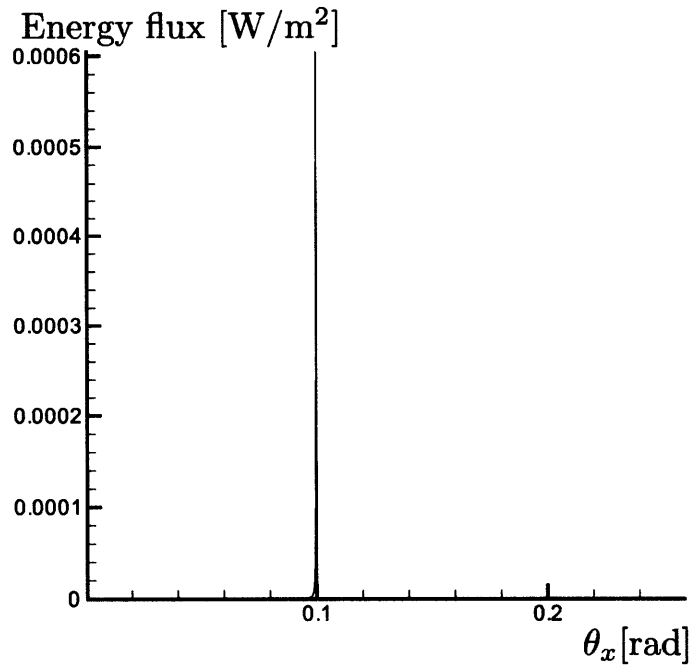
Figure 4-9: Energy flux ($\nu = 0.1$, $\alpha = 0$)

Energy flux [W/m²]

Figure 4-10: Energy flux graph ($\nu = 0.25$, $\alpha = \frac{\pi}{2}$)

Energy flux [W/m²]

Figure 4-11: Zoomed view of energy flux graph ($\nu = 0.25$, $\alpha = \frac{\pi}{2}$)

93

Figure 4-12: Energy flux graph ($\nu = 0.8$, $\alpha = \frac{\pi}{2}$)

Figure 4-13: Zoomed view of energy flux graph ($\nu = 0.8$, $\alpha = \frac{\pi}{2}$)

As seen in Fig.(4-7) through Fig.(4-13), time-averaged Poynting's vector are spatially oscillating. This is because the wave field at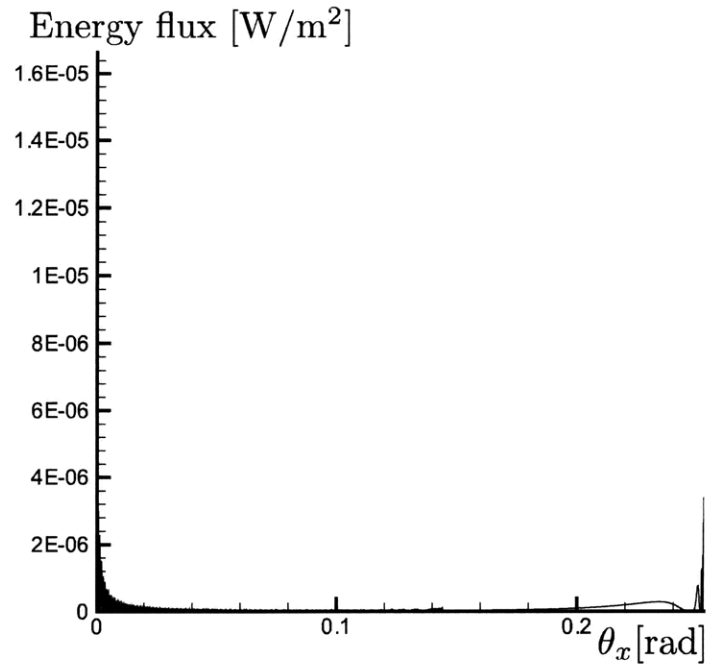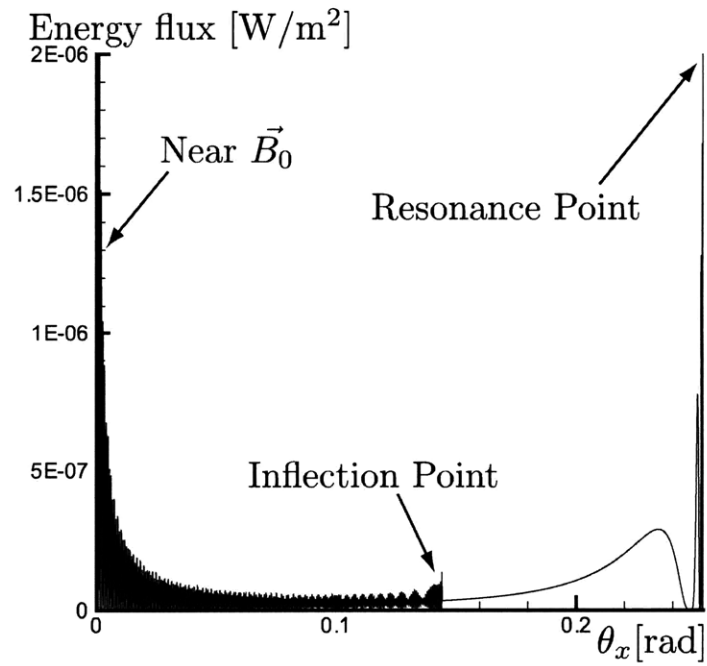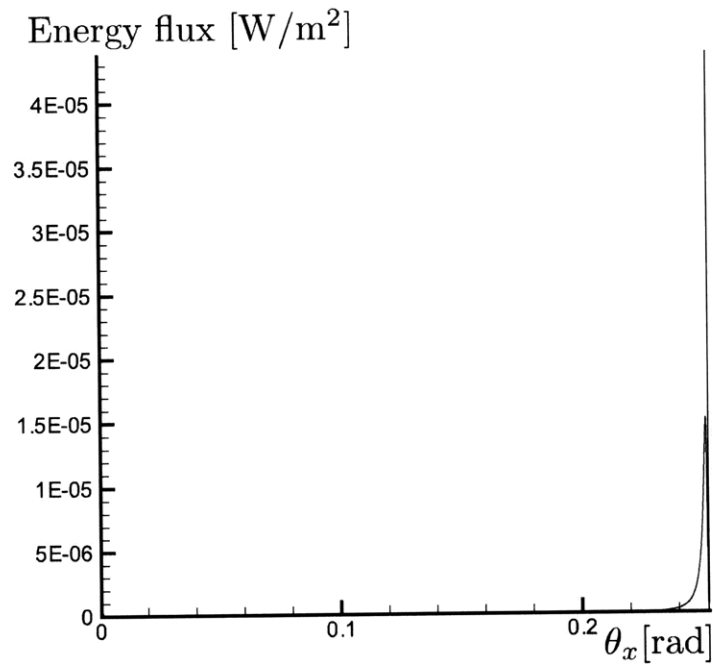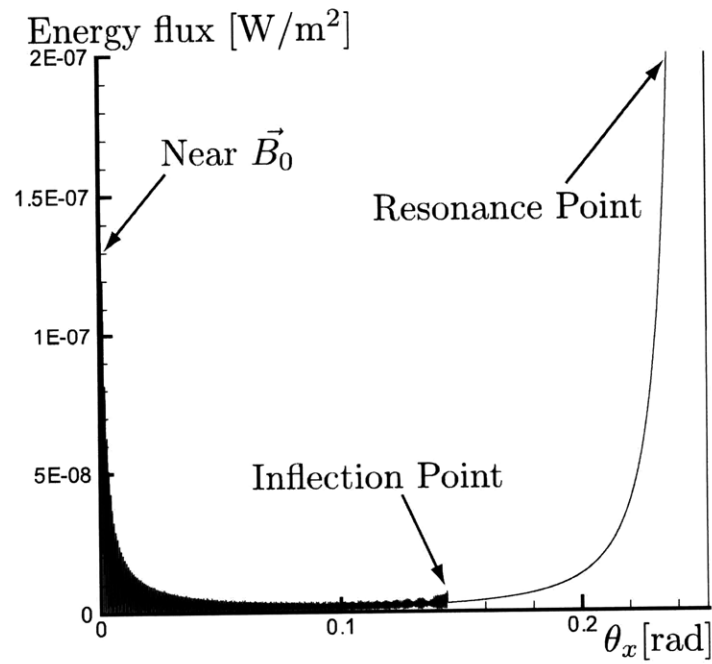 one observation point is the sum of more than one $\vec{k}$ wave as shown in Chapter 3. In vacuum (and in some Whistler cases), the electromagnetic wave at one observation point consists of just one $\vec{k}$ wave, so from Eq.(4.1) the time-averaged Poynting's vector $\left(\text{putting } X = E, \ Y = \frac{B}{\mu_0}\right)$ is

$$
\begin{aligned}
\left\langle \vec{S} \right\rangle &= \frac{1}{2}\left(Xe^{-ik_1x}\right) \times \left(Ye^{-ik_1x}\right)^* \\
&= \frac{1}{2}X \times Y^*
\end{aligned}
\tag{4.2}
$$

which has no rapid spatial dependence. However, in our case the electromagnetic wave at one observation point is the sum of more than one $\vec{k}$ wave in plasma; then the time-averaged Poynting's vector is obtained from the sum of up to three $\vec{k}$ waves:

$$
\begin{aligned}
2\left\langle \vec{S} \right\rangle &= \mathrm{Re}\left[\left(X_1e^{-ik_1x} + X_2e^{-ik_2x} + X_3e^{-ik_3x}\right) \times \left(Y_1e^{-ik_1x} + Y_2e^{-ik_2x} + Y_3e^{-ik_3x}\right)^*\right] \\
&= \mathrm{Re}\left[X_1 \times Y_1^* + X_2 \times Y_2^* + X_3 \times Y_3^* + X_1 \times Y_2^*e^{i(k_2-k_1)x} + X_2 \times Y_1^*e^{i(k_1-k_2)x}\right. \\
&\quad +X_1 \times Y_3^*e^{i(k_3-k_1)x} + X_3 \times Y_1^*e^{i(k_1-k_3)x} + X_2 \times Y_3^*e^{i(k_3-k_2)x} \\
&\quad \left.+X_3 \times Y_2^*e^{i(k_2-k_3)x}\right]
\end{aligned}
\tag{4.3}
$$

Therefore high frequency oscillation terms $(e^{i(k_2-k_1)x}, \ e^{i(k_1-k_2)x} \ \cdots)$ remain in the time-averaged Poynting's vector because x in Eq.(4.3) is large (far field). These spatial oscillations are not shown in previous works such as [12, 13, 1].

T. N. C. Wang and T. F. Bell calculated the radiation pattern in a different way.[1] Fig.(4-14) and (4-15) are their radiation pattern of perpendicular and parallel antenna for $\nu = 0.25$. The Near $\vec{B}_0$ radiation for the parallel antenna is much weaker than the resonance point radiation in the same way as in our result. The resonance occurs at $13.9°$ in their calculation as in Fig.(4-14) and (4-15), but in our calculation, the resonance occurs at $\theta_x \simeq 14.5°$. The reason of this difference is because of the fact that they took the ion effect into account. Our radiation pattern has spatial oscillations, but their radiation pattern is a "filtered" pattern without spatial oscillations. One possible reason of this difference is that they calculated the wave energy flux directly

unlike our calculation way which is to calculate electric field and magnetic field first, then calculate the Poynting's vector. It could also be due to lack of resolution in their integration; no information was given on this point in their paper.
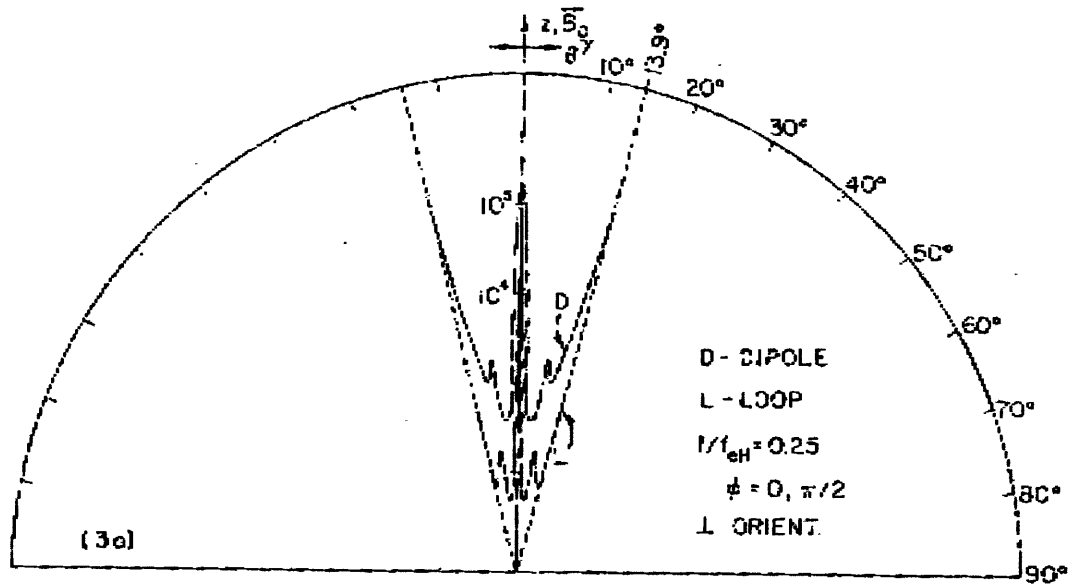

Figure 4-14: Radiation pattern for perpendicular antenna, $\nu = 0.25$ by Wang and Bell[1]
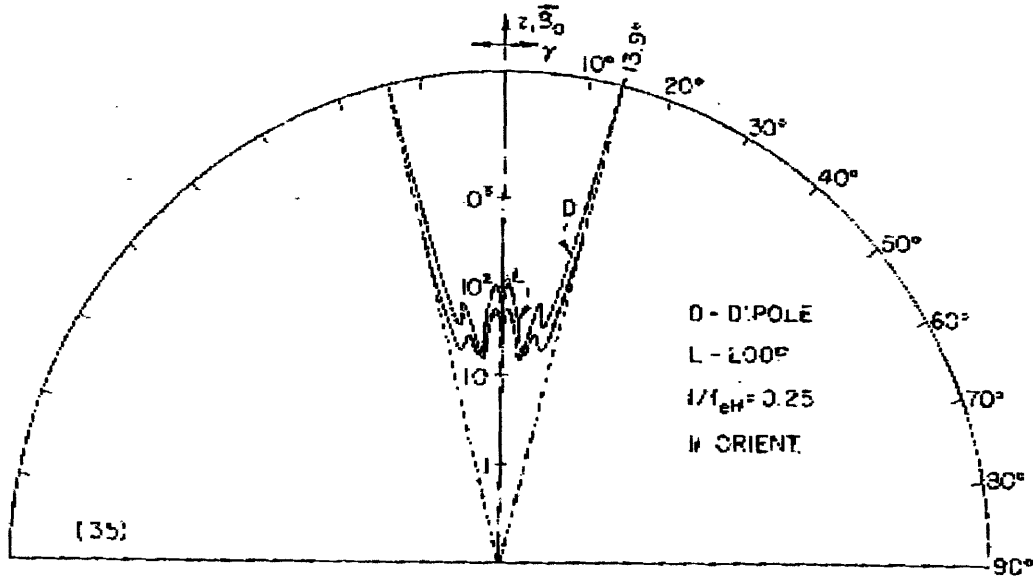
Figure 4-15: Radiation pattern for parallel antenna, $\nu = 0.25$ by Wang and Bell[1]

Laboratory experimental results for $\nu = 0.6$ have been presented in [2]. In this experiment, radiation from a dipole antenna in a uniform magnetized plasma in the laboratory is observed. By changing the plasma density, this paper showed the trend that if the plasma density is low, then the Near $\vec{B}_0$ radiation is strong, and when the plasma density goes higher, the calculated Resonance point radiation gets stronger. Fig.(4-16) through Fig.(4-40) are the calculated radiation patterns for various electron densities with parameters chosen to be the same as in one of the experiments and the radiation pattern of the experimental data. The receiver antenna in his experiment has finite length, so we took the antenna average over the radiation pattern assuming that the sensitivity of the receiving antenna is triangular. The trend of our results matches well with the radiation trend in the experiment. For long antenna (4.5cm antenna), the shape of the radiation pattern of our calculation is very close to that of the experimental data with the same plasma density as in Fig.(4-28). However, for short antenna (1.1cm antenna), the radiation pattern is different from that of the experimental data if we calculate with the same plasma density as in the experiment.

97

If we use higher plasma density than that in the experiment (two or three times higher density), the radiation pattern is very close at all density levels to that of the experimental data.

Energy flux [W/m²]

Figure 4-16: Radiation pattern $(\omega_p/\omega = 57$, antenna length is 4.5cm). Highest density for this sequence.

Figure 4-17: Radiation pattern of the experimental data $(\omega_p/\omega = 57$, antenna length is 4.5cm).[2]

Figure 4-18: Radiation pattern $(\omega_p/\omega = 33$, antenna length is 4.5cm). Density is lower than in Fig.(4-16)

Figure 4-19: Radiation pattern of the experimental data $(\omega_p/\omega = 33$, antenna length is 4.5cm). [2]
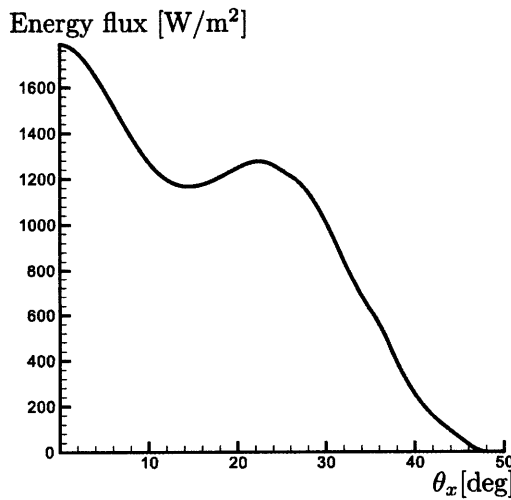
Figure 4-20: Radiation pattern $(\omega_p/\omega = 28$, antenna length is 4.5cm). Density decreased again.

Figure 4-21: Radiation pattern of the experimental data $(\omega_p/\omega = 28$, antenna length is 4.5cm).[2]

Figure 4-23: Radiation pattern of the experimental data ($\omega_p/\omega = 23$, antenna length is 4.5cm).[2]

Figure 4-22: Radiation pattern ($\omega_p/\omega = 23$, antenna length is 4.5cm). Density decreased again. Note the emerging resonance peak.

Figure 4-25: Radiation pattern of the experimental data ($\omega_p/\omega = 16$, antenna length is 4.5cm).[2]

Figure 4-24: Radiation pattern ($\omega_p/\omega = 16$, antenna length is 4.5cm). Density decreased further.

Energy flux [W/m^2]
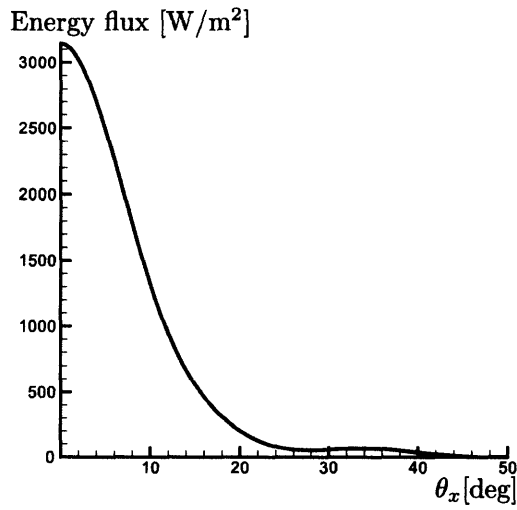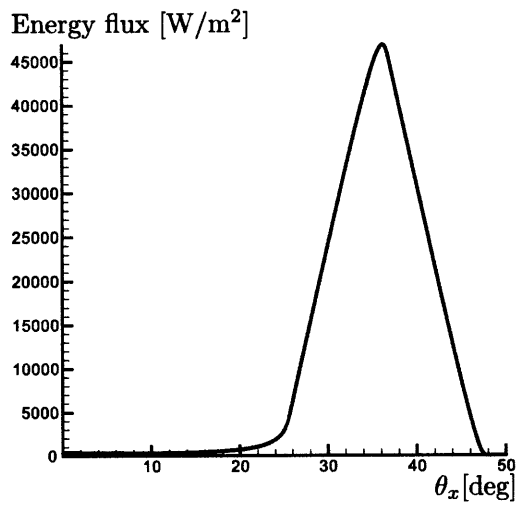

Figure 4-26: Radiation pattern $(\omega_p/\omega = 5.7$, antenna length is 4.5cm). Lowest density.
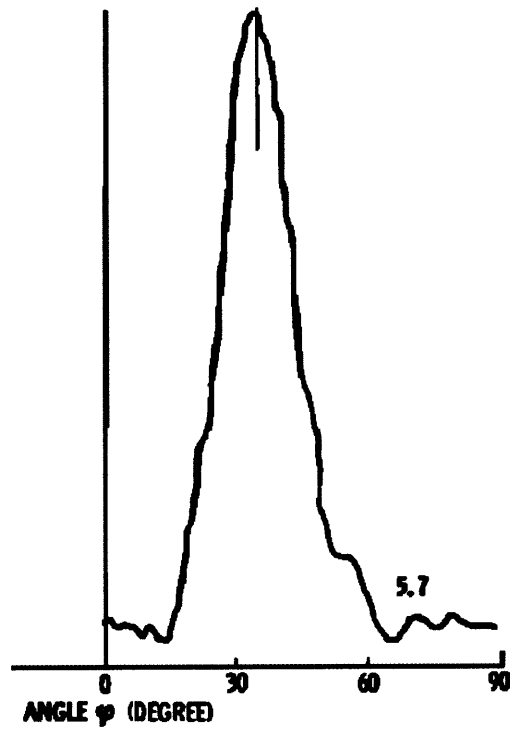
Figure 4-27: Radiation pattern of the experimental data $(\omega_p/\omega = 5.7$, antenna length is 4.5cm).[2]

101
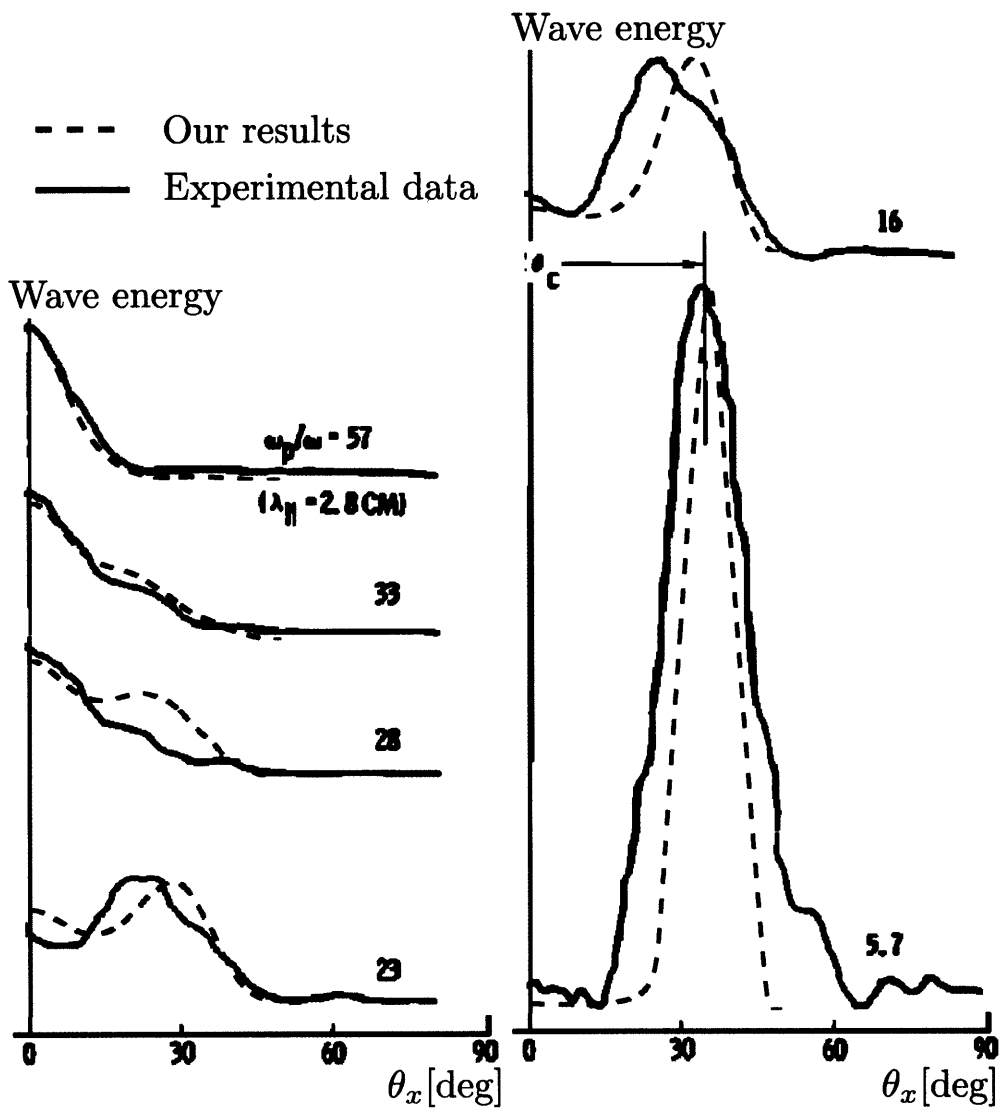
Figure 4-28: Radiation patterns of our result and experimental data.
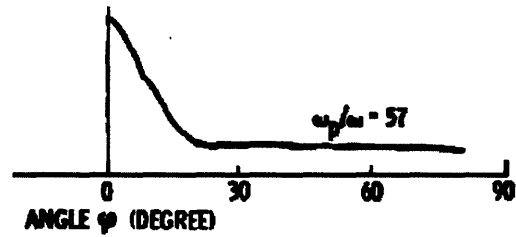
Energy flux [W/m²]

Figure 4-30: Radiation pattern of the experimental data $(\omega_p/\omega = 60$, antenna length is 1.1cm).[2]
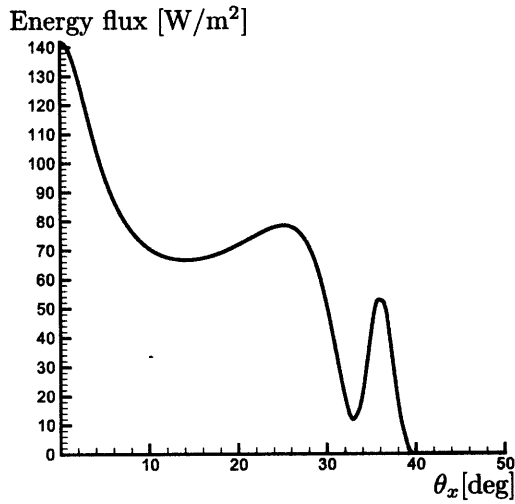
Figure 4-29: Radiation pattern $(\omega_p/\omega = 120$, antenna length is 1.1cm). Highest density for this sequence.

Energy flux [W/m²]

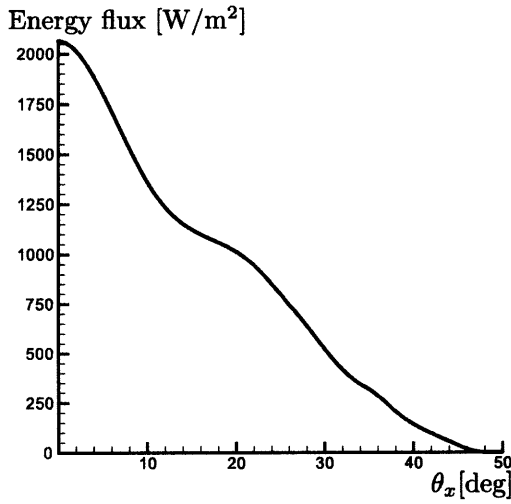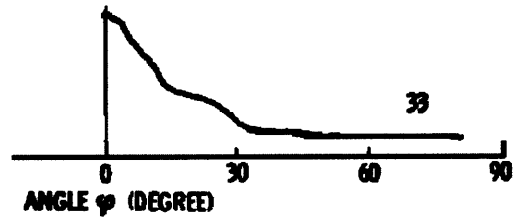Figure 4-32: Radiation pattern of the experimental data $(\omega_p/\omega = 57$, antenna length is 1.1cm).[2]
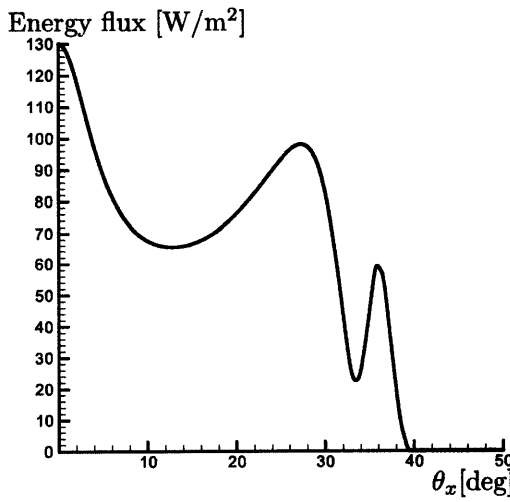
Figure 4-31: Radiation pattern $(\omega_p/\omega = 110$, antenna length is 1.1cm)

103

Energy flux [W/m²]
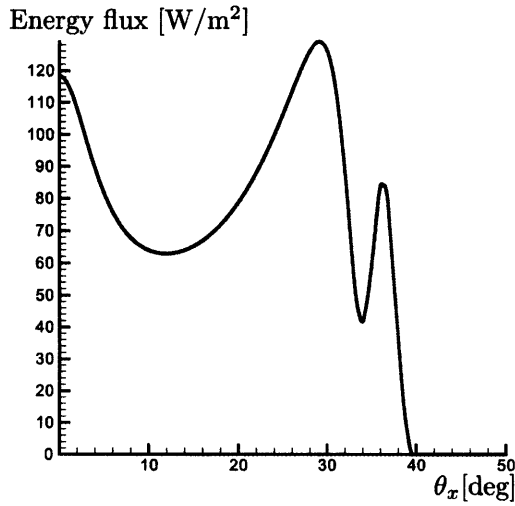
Figure 4-33: Radiation pattern (ω_p/ω = 100, antenna length is 1.1cm)
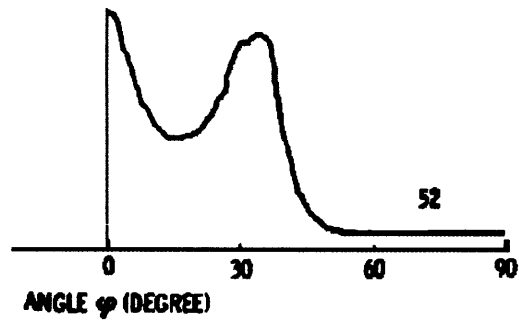
Figure 4-34: Radiation pattern of the experimental data (ω_p/ω = 52, antenna length is 1.1cm).[2]

Energy flux [W/m²]
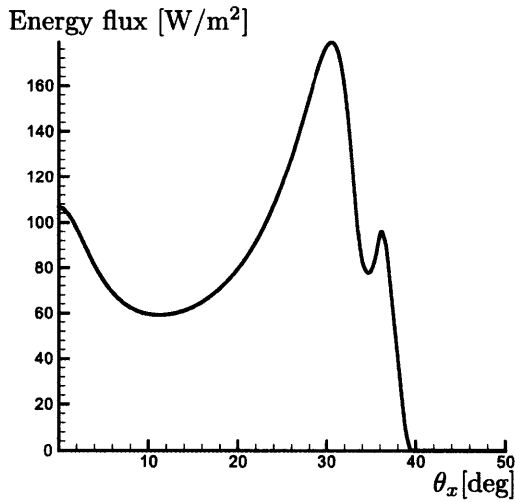
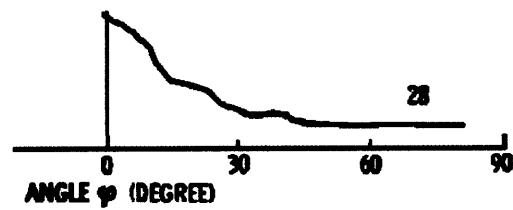Figure 4-35: Radiation pattern (ω_p/ω = 90, antenna length is 1.1cm)
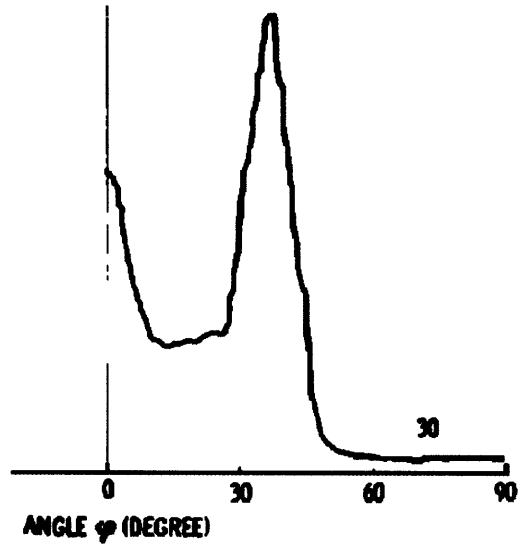
Figure 4-36: Radiation pattern of the experimental data (ω_p/ω = 30, antenna length is 1.1cm).[2]
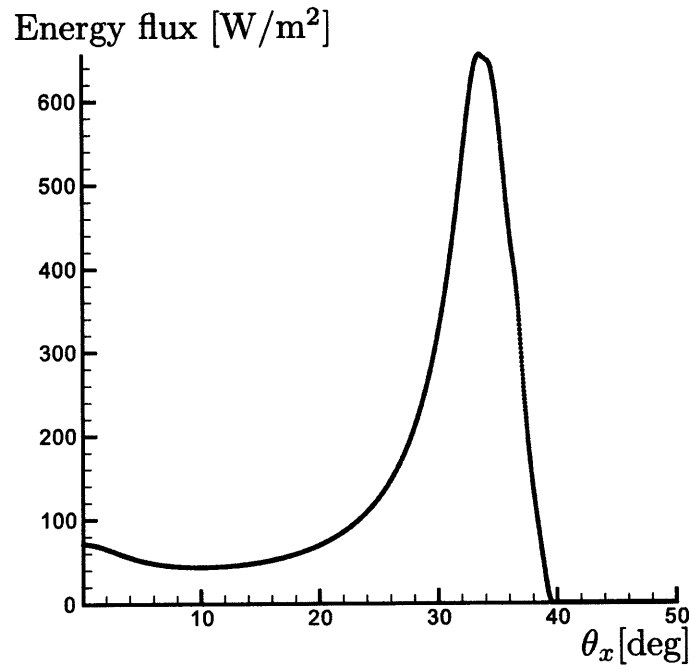
Figure 4-37: Radiation pattern ($\omega_p/\omega = 60$, antenna length is 1.1cm)
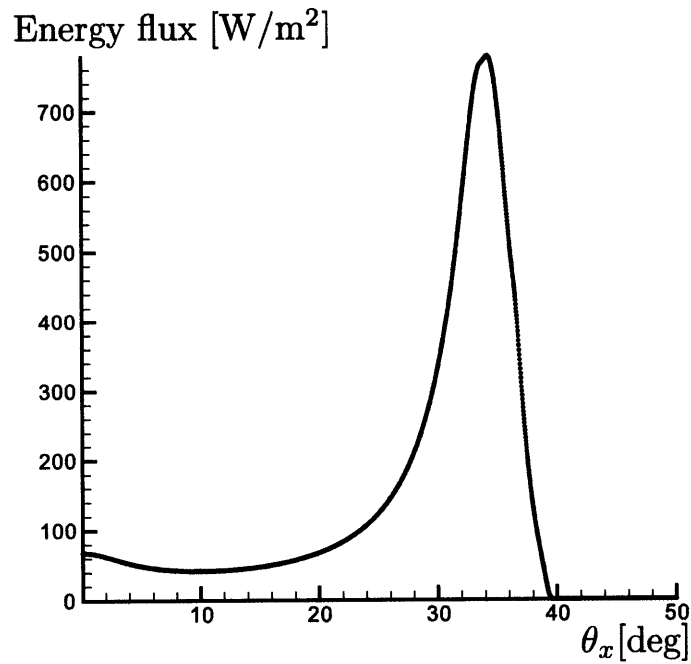
Figure 4-38: Radiation pattern ($\omega_p/\omega = 57$, antenna length is 1.1cm)
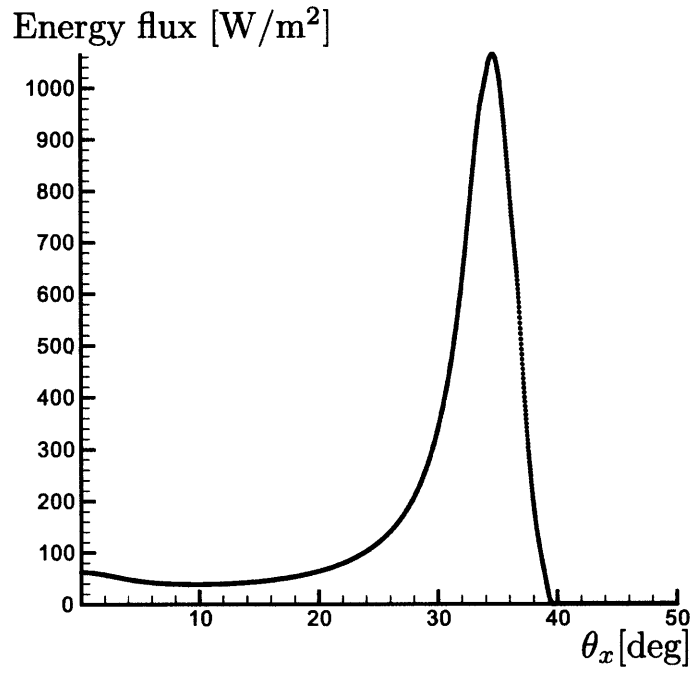
Figure 4-39: Radiation pattern ($\omega_p/\omega = 52$, antenna length is 1.1cm)
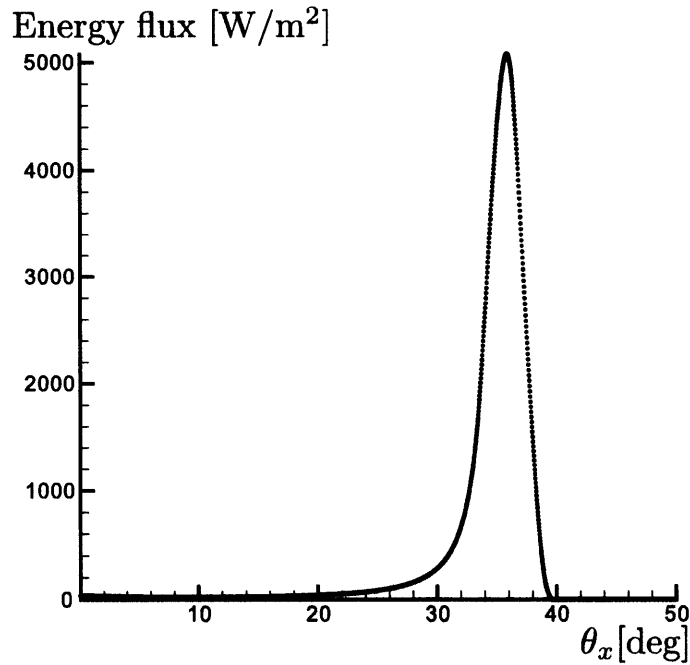
Figure 4-40: Radiation pattern ($\omega_p/\omega = 30$, antenna length is 1.1cm). Lowest density for this sequence.
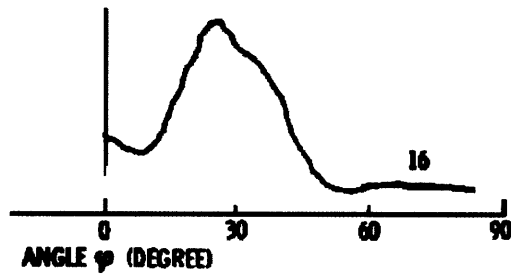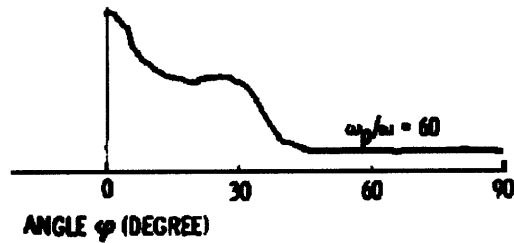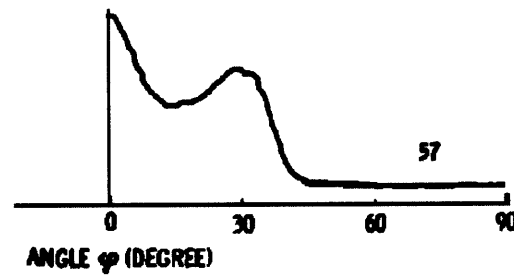
4.2 Resonance

Formally, resonance occurs when k goes to infinity. From Eq.(2.20), $\theta = \cos^{-1}\nu$ at resonance. Using group velocity analysis, for example Eq.(3.23), $\theta_G = \sin^{-1}\nu$ at resonance. Therefore there is a resonance cone around the magnetic field, and this cone has an angle $\theta_x = \sin^{-1}\nu$ to magnetic field line. As in figures in Section 3.3, resonance occurs at the wave branch which propagates with $\phi = \pi + \phi_x$.

4.2.1 Stationary Phase Method and Resonance

From Eq.(3.15),

$$
\vec{E} = \sum_{\text{StationaryPoints}} -\frac{Il\sin\theta\left(1 - \cos\frac{k_\parallel L}{2}\right)e^{-i\frac{r}{l}\sqrt{\nu}\Phi\nu^2}}{\sqrt{2\pi}\sigma_{ce}\cos\theta\left(\sin\theta\cos\phi\sin\alpha + \cos\theta\cos\alpha\right)^2 Lr}
$$

$$
\frac{1}{\sqrt{\pm\cos\theta_x\sin\theta\sin\theta_x \mp 2\left(\cos\theta - \nu\right)\cos\left(\theta \pm \theta_x\right)\sin\theta\sin\theta_x}\sqrt{\cos\theta - \nu}}
$$

$$
\begin{bmatrix}
\left[\frac{i}{\nu}\left(\cos\theta - \nu\right)\left(\cos\theta - \frac{1}{\nu}\right) + \left(-\frac{i}{\nu} + i\cos\theta\right)\sin^2\theta\cos^2\phi\, i\frac{\cos\theta-\nu}{\nu^2}\sin^2\theta\sin^2\phi\right]\sin\alpha \\
\left[-\frac{(\cos\theta-\nu)^2}{\nu^2} - \frac{\cos\theta-\nu}{\nu}\sin^2\theta + \left(-i\frac{\cos\theta}{\nu^2} + i\cos\theta\right)\sin^2\theta\sin\phi\cos\phi\right]\sin\alpha \\
\left[-\frac{\cos\theta-\nu}{\nu}\sin\theta\cos\theta\sin\phi + \left(-\frac{i}{\nu} + i\cos\theta\right)\sin\theta\cos\theta\cos\phi\right]\sin\alpha \\
\left[\frac{\cos\theta-\nu}{\nu}\sin\theta\cos\theta\sin\phi + \left(-\frac{i}{\nu} + i\cos\theta\right)\sin\theta\cos\theta\cos\phi\right]\cos\alpha \\
\left[-\frac{\cos\theta-\nu}{\nu}\sin\theta\cos\theta\cos\phi + \left(-\frac{i}{\nu} + i\cos\theta\right)\sin\theta\cos\theta\sin\phi\right]\cos\alpha \\
\left[\left(-i\frac{i}{\nu} + i\cos\theta\right)\cos^2\theta + i\cos\theta\right]\cos\alpha
\end{bmatrix}
\tag{4.4}
$$

107

From Eq.(3.17),

$$\vec{B} = \sum_{\text{StationaryPoints}} -\frac{I \sin\theta \left(1 - \cos\frac{k_\parallel L}{2}\right) e^{-i\frac{r}{7}\sqrt{\nu}\Phi\sqrt{\nu}}}{\sqrt{2\pi}\sigma_{ce}\cos\theta \left(\sin\theta\cos\phi\sin\alpha + \cos\theta\cos\alpha\right)^2 Lr\omega_{ce}}$$

$$\frac{1}{\sqrt{\pm\cos\theta_x \sin\theta\sin\theta_x \mp 2\left(\cos\theta - \nu\right)\cos\left(\theta \pm \theta_x\right)\sin\theta\sin\theta_x}} \cdot$$

$$\begin{bmatrix} \left[\sin^2\theta\cos\theta\left(\cos^2\phi + \frac{i}{\nu}\sin\phi\cos\phi\right) + \frac{\cos\theta-\nu}{\nu}\cos\theta\right]\sin\alpha \\ \left[\cos\theta\left\{\sin^2\theta\sin\phi\left(\cos\phi + \frac{i}{\nu}\sin\phi\right) - \frac{i}{\nu} + i\nu\right\} + i\left(\cos\theta - \nu\right)\cos\theta\right]\sin\alpha \\ \left[-\sin^3\theta\left(\cos\phi + \frac{i}{\nu}\sin\phi\right) + \left(\frac{i}{\nu} - i\cos\theta\right)\sin\theta\sin\phi - \frac{\cos\theta-\nu}{\nu}\sin\theta\cos\phi\right]\sin\alpha \\ \left[i\sin\phi + \cos^2\theta\cos\phi\right]\sin\theta\cos\alpha \\ \left[\cos^2\theta\sin\phi - i\cos\phi\right]\sin\theta\cos\alpha \\ -\sin^2\theta\cos\theta\cos\alpha \end{bmatrix} \tag{4.5}$$

From Eq.(4.4) and Eq.(4.5), $\vec{E}$, $\vec{B}$, and Poynting's vector $\vec{S}$ have the following limiting dependence on the diverging term $\frac{1}{\cos\theta-\nu}$:

$$\vec{E} \propto \frac{1}{\sqrt{\cos\theta - \nu}} \tag{4.6}$$

$$\vec{B} \propto \left(\cos\theta - \nu\right)^0 \tag{4.7}$$

$$\vec{S} = \frac{1}{\mu_0}\vec{E} \times \vec{B} \propto \frac{1}{\sqrt{\cos\theta - \nu}} \tag{4.8}$$

Therefore $\vec{E}$ and $\vec{S}$ diverge to infinity at resonance,but the $\vec{S}$ divergence is integrable. The magnetic field of the wave doesn't diverge and has finite value at resonance. This analysis confirms that the wave at resonance is electrostatic, as was discussed in (2.3.1).

As previously noted, resonance occurs on the wave branch shown in Fig.(4-41). Any stationary point θ_s on this wave branch is always near to $\cos^{-1}\nu$. Therefore, the contribution of this wave branch to the integration in the wave field calculation is much larger than that of other wave branches.
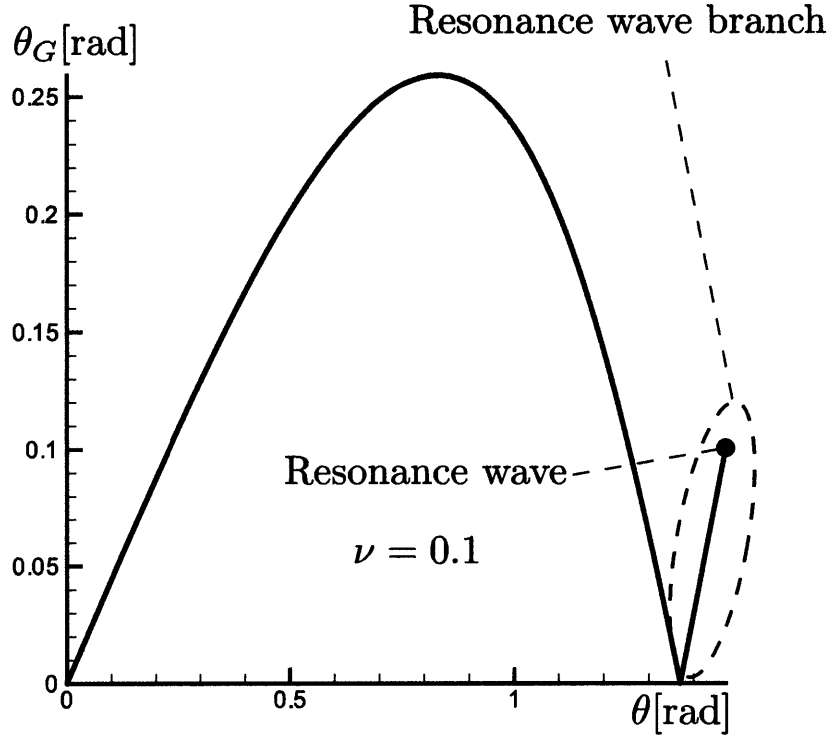
Figure 4-41: Resonance wave branch

4.3 Inflection Point

In the stationary points there is in some of the cases a point where $\frac{\partial^2 \Phi}{\partial \theta^2} = 0$. We call this point the inflection point. There is only one inflection point in our case, which is ⓑ in Fig.(3-7). On this point,

$$\theta = \cos^{-1}\left(\nu + \sqrt{\frac{1-\nu^2}{3}}\right) \qquad (4.9)$$

from Eq.(3.12) and Eq.(3.13). Two wave modes (two stationary point branches on the right side and left side in Fig.(3-7)) merge into one wave mode at the inflection point, then strong radiation occurs. $\frac{\partial^2 \Phi}{\partial \theta^2}$ terms in Eq.(3.15) and Eq.(3.17) are zero at the inflection point. Then the electric field and the magnetic field diverge weakly at this point if we calculate the wave field as in Eq.(3.15) and Eq.(3.17). If θ is near the inflection point, the second derivative $\frac{\partial^2 \Phi}{\partial \theta^2}$ is much smaller than the third derivative $\frac{\partial^3 \Phi}{\partial \theta^3}$. However the integration of the exponential term with a third order

109

assymptotic expansion is difficult, also the contribution to the radiation power in the neighborhood of this inflection point is small, so we calculate the radiation power integration without considering this inflection point effect, just using the stationary point method to very near the inflection point and skipping over the precise location of the singularity at $\frac{\partial^2 \Phi}{\partial \theta^2}$.

Chapter 5

Radiation Power and Resistance Analysis

5.1 Radiation Power

By integrating the time-averaged Poynting's vector on the sphere around the antenna, the power radiated by the antenna can be calculated. The radiated power P is

$$
\begin{aligned}
P &= \int_0^\pi \int_0^{2\pi} \left(\frac{\vec{r}}{|\vec{r}|} \cdot \left\langle \vec{S} \right\rangle \right) r^2 \sin \theta_x d\theta_x d\phi_x \\
&= 2 \int_0^{\frac{\pi}{2}} \int_0^{2\pi} \left(\frac{\vec{r}}{|\vec{r}|} \cdot \left\langle \vec{S} \right\rangle \right) r^2 \sin \theta_x d\theta_x d\phi_x
\end{aligned}
\tag{5.1}
$$

This integration can be done by trapezoidal integration of the Poynting's vector results in Section 4.1.

At the resonance point, the time-averaged Poynting's vector diverges to ∞. However, as shown by Eq.(4.6), by the Poynting's vector near the resonance point is propotional to and dominated by $\frac{1}{\sqrt{\cos\theta-\nu}}$, and integration of $\frac{1}{\sqrt{\cos\theta-\nu}}$ results in a finite value.

The radiated power to the region θ_{x1} to θ_{x2} in Fig.(5-1) (very near the resonance) is

$$
P_{\text{res1}} = \int_{\theta_{x1}}^{\theta_{x2}} \frac{C}{\sqrt{\cos\theta - \nu}} d\theta_x
\tag{5.2}
$$

Where C is approximately a constant in the integration. From eq.(3.11), at the
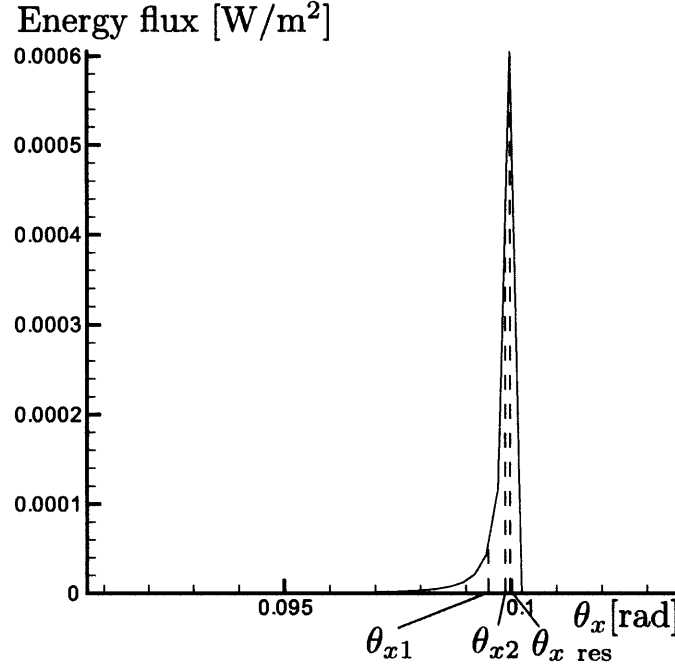
Figure 5-1: Energy flux near resonance point

stationary points on the resonance wave branch

$$\cos\theta - \nu = \frac{\sin\theta}{2\tan(\theta + \theta_x)} \qquad (5.3)$$

Now, if θ_{x1} and θ_{x1} are very near to $\theta_{x\ res}$ (at the resonance point), by using Taylor series expansion $\cos\theta - \nu$ can be expressed as

$$
\begin{aligned}
\cos\theta - \nu &= (\cos\theta - \nu)_{\text{at resonance}} + \left.\frac{d(\cos\theta - \nu)}{d\theta_x}\right|_{\text{at resonance}} (\theta_x - \theta_{x\ res}) \\
&\quad + \left.\frac{d^2(\cos\theta - \nu)}{d\theta_x^2}\right|_{\text{at resonance}} (\theta_x - \theta_{x\ res})^2 \\
&= \frac{\sqrt{1 - \nu^2}}{2}(\theta_x - \theta_{x\ res}) + 0 \times (\theta_x - \theta_{x\ res})^2 \qquad (5.4)
\end{aligned}
$$

Third or higher terms are neglected. Then, Eq.(5.2) becomes

$$
\begin{aligned}
P_{\text{res1}} &= \int_{\theta_{x2}}^{\theta_{x1}} \frac{C'}{\sqrt{\theta_x - \theta_{x\ res}}} d\theta_x \\
&= 2C'\left(\sqrt{\theta_{x\ res} - \theta_{x1}} - \sqrt{\theta_{x\ res} - \theta_{x2}}\right) \qquad (5.5)
\end{aligned}
$$

112

Where C' is a constant different from C. Also, the radiated power to the region from θ_{x2} to $\theta_{x\ res}$ in Fig.(5-1) is

$$P_{res2} = 2C' \left(\sqrt{\theta_{x\ res} - \theta_{x2}} \right) \tag{5.6}$$

Then, using the trapezoidal integration result of P_{res1}, P_{res2} can be calculated as

$$P_{res2} = \frac{P_{res1} \left(\sqrt{\theta_{x\ res} - \theta_{x2}} \right)}{\sqrt{\theta_{x\ res} - \theta_{x1}} - \sqrt{\theta_{x\ res} - \theta_{x2}}} \tag{5.7}$$

By add P_{res2} to radiation power integration to θ_{x2}, radiation power near the resonance point can be calculated.

5.2 Radiation Resistance

The radiation power from the antenna P can be calculated as in 5.1. The radiation resistance R can be calculated by the radiation power P and the antenna current $I = 0$ as follows.

$$R = \frac{2P}{I_0^2} \tag{5.8}$$

T. N. C. Wang and T. F. Bell calculated the radiation resistance in a different way.[16] K. G. Balmain[17] also calculated the radiation impedance of the short dipole antenna in the same way as Wang and Bell. They calculated the radiation power by integrating the product of the current and the electric field. Then they calculated the radiation resistance for an antenna parallel to $\vec{B}_0$ as follows.

$$R_{\parallel} = \frac{Z_0}{2\epsilon_s h\beta} \left[1 - \frac{2\pi + 1}{6\pi} \epsilon_s (h\beta)^2 - \frac{2\pi}{3} \left(\frac{X}{Y-1} \right)^{1/2} \frac{Y-2}{Y^3} (h\beta)^3 \right] \tag{5.9}$$

where $Z_0 = 377\text{ohm}$, h:half of the antenna length, $\beta = \frac{\omega}{c}$, $\epsilon_s = \frac{X}{Y^2-1}$, $X = \frac{\omega_{pe}^2}{\omega^2}$, $Y = \frac{\omega_{ce}}{\omega}$.

Fig.(5-2) shows the radiation resistance for various antenna lengths L. In this calculation, $\nu = 0.1$. In these figures, our calculation results match well with the
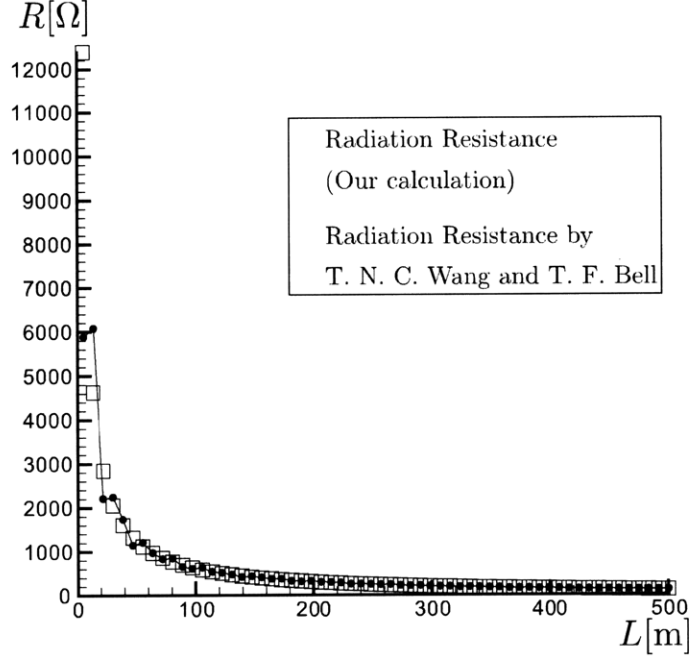
Figure 5-2: Radiation resistance and antenna length (Antenna parallel to $\vec{B}_0$)

results by Wang and Bell, but our results have oscillations in the short antenna region. These oscillations could be a numerical artifact, due to the high resolution needed for resolving the spatial oscillation of the Poynting's vector during its integration. The results by Wang and Bell are near to the average value of this oscillation of our results. The radiation resistance diverge as the antenna gets smaller. From these results, it seems that the radiation power is larger for the shorter antenna, for fixed antenna current. However, we also should look at the imaginary part of the impedance of the antenna. If the AC amplitude of the antenna voltage is high, the sheath around the antenna is thick. In this thesis research, we do not take the effect of the sheath into account, but the sheath covers the antenna and can weaken the radiation.

This thesis has not computed the imaginary part of the radiation impedance, $X_{\parallel}$, but in view of the good agreement found with the "short antenna" thesis of Balmain[17] and Wang/Bell[14][16] for $R_{\parallel}$, we can with confidence use their results for $X_{\parallel}$:

$$X_{\parallel} = -\frac{Z_0}{\pi \epsilon_s h \beta} \left[\log\left(\frac{2h}{\gamma a}\right) - 1 \right] \qquad (5.10)$$

114

where a is the radius of the antenna,

$$\gamma = \sqrt{\frac{P}{S}}, \quad P = 1 - \frac{\omega_{pe}^2}{\omega^2}, \quad S = 1 - \frac{\omega_{pe}^2}{\omega^2 - \omega_{ce}^2} \tag{5.11}$$

$X_{||}$ is inversely proportional to the antenna length in the same way as $R_{||}$.

Chapter 6

Conclusions and Future Work

6.1 Conclusions

In this thesis, we analyzed how low-frequency Electromagnetic waves propagate in the Ionosphere. In this analysis, we assumed the following:

- The frequency of the EM wave is so low that only electrons react to the wave field and ions do not react.

- The plasma temperature and the plasma density are not high. The collision term in the electron equation of motion is very small.

- The current distribution of the antenna is triangular.

- The plasma is homogeneous. There is no sheath around the antenna.

Chapter 2 presents how the wave field in the magnetized plasma can be calculated. We used Maxwell's equations and electron equations of motion. By using the Fourier transform and the Inverse Fourier transform, the wave field at an observation point can be calculated. The Inverse Fourier transform is a complicated integration, but we can caluculate this integration analytically with residue theorem and the Stationary Phase Method.

The calculation method of the Inverse Fourier transform using residue theorem and the Stationary Phase Method is shown in Chapter 3. Also this chapter presents the

group velocity analysis. By analyzing the group velocity of the EM wave, we can understand how EM waves propagate to the observation point. We used the $\vec{V_G}$ graph, the $\vec{k}$ tip graph and the θ vs θ_x graph to show which $\vec{k}$ wave propagates to the observation point and which $\vec{k}$ wave does not. We can see that more than one $\vec{k}$ wave propagates to one observation point, and there is a resonance wave; also two wave modes merge into one wave mode at the inflection point. Also, the propagation ways of these $\vec{k}$ waves are different with the frequency of the wave.

Chapter 4 presents the calculated wave field. The radiation pattern has some characteristics. There are intense radiation directions which are the near $\vec{B_0}$ zone, the Resonance zone and the Inflection point zone. We also compared our results with past experimental work. The trend of the radiation pattern of our results matches with the experimental data. This chapter also presents that radiation pattern has spatial oscillation that comes from the superpopsition of $\vec{k}$ waves. Finally, in this chapter, we analyzed the intense radiation zones in more detail. Near $\vec{B_0}$ intense radiation occurs in a thin cylinder. At the resonance point, the wave is an electrostatic wave. Only the magnetic field is finite and electric field diverges.

In Chapter 5, we calculated the radiated power and the radiation resistance. By integrating the Poynting's vector around the antenna, we can calculate the radiated power by the antenna. In this calculation, computational integration is used. At the resonance point, the Poynting's vector diverges, but we calculated the Poynting's vector integration at this point by approximating the Poynting's vector as a function of θ_x. Then we also compared the radiation resistance with the past work. Our results reproduce the radiation power of Bell and of Balmain, and show that antenna of 100m length can still be regarded as simple dipoles.

6.2   Future Work

Possible future researches are listed in the following.

1. Antenna design work.

118

The radiation power for various antenna length can be calculated using our theory in this thesis. We can estimate the optimum antenna size in aspects of the mass of the antenna, the antenna dynamism, the antenna input voltage which has a large influence on the sheath, the heat issue of the antenna, and so on.

2. More detailed analysis on intense radiation zones.

   - For the near $\vec{B}_0$ zone, we analyzed for the parallel antenna case using Bessel's functions. However, this analysis is not valid for the perpendicular antenna case. For the perpendicular antenna case, the integration in the Inverse Fourier transform is much more complicated, and we need another kind of approximation for this calculation.

   - For the Inflection point zone, if we just use the Stationary Phase Method and calculate the wave field, then the wave field diverges. However, we decided that the influence of this wave field is small to the whole radiation. More precise analysis is possible.

3. Sheath around the antenna

   In this research, we considered only the far field. However there should be a sheath around the antenna, and strong interactions between the antenna and the charged particles occur in the near field. Except for the dipole limit, we calculated only the radiation resistance which is the real part of the antenna impedance, but the antenna input voltage is affected also by the imaginary part of the antenna impedance. The sheath shape is influenced by this input voltage. Therefore, the imaginary part of the antenna impedance is necessary for the more detailed simulation.

4. Inhomogeneous plasma simulation

   Our analysis is for the wave propagation in homogeneous plasma. The analysis on the wave propagation in inhomogeneous is left to a more advanced research.

5. Nonlinear duct-forming effect analysis

This nonlinear effect in the plasma may guide Whistler waves close to the $\vec{B}_0$ direction of at high power.

6. Experiments

Only a few experiments on the wave propagation in magnetized plasma has been done in the past. To compare the result of analysis with other data, we need some experiments.

Bibliography

[1] T. F. Bell T. N. C. Wang. Vlf/elf radiation patterns of arbitrarily oriented electric and magnetic dipoles in a cold lossless multicomponent magnetoplasma. *J. Geophys. Res.*, 7:1174–1189, March 1972.

[2] R. L. Stenzel. Antenna radiation patterns in the whistler wave regime measured in a large laboratory plasma. *Radio Sci.*, 11:1045–1056, December 1976.

[3] R.J. Hynds J.J. Quenby A.C. Durney, H. Elliot. The artificial radiation belt produced by the starfish nuclear explosion. *Proc. Roy. Soc. (London)*, 281:565–583, October 1964.

[4] D. Nunn M. A. Clilverd, C. J. Rodger. Radiation belt electron precipitation fluxes associated with lightning. *J. Geophys. Res.*, 109, December 2004.

[5] W. B. Peter J. A. Sauvaud M. Parrot U. S. Inan, D. Piddyachiy. Demeter satellite observations of lightning-induced electron precipitation. *Geophys. Res. Lett.*, 34, April 2007.

[6] R. J. M. Fry. Radiation effects in space. In *Committee on Space Research meeting, (Toulouse, France)*, June 1986.

[7] James M. McGarrity Joseph R. Srour. Radiation effects on microelectronics in space. *IEEE, Proceedings*, 76:1443–1469, November 1988.

[8] Nasa spinoff, 2008.

[9] A.L. Vampola H.C. Koons, B.C. Edgar. Precipitation of inner zone electrons by whistler mode waves from the vlf transmitters ums and nwc. *J. Geophys. Res.*, 86:640–648, February 1981.

[10] C. Jacquey M. Parrot J.-J. Berthelier R. J. Gamble Craig J. Rodger J.-A. Sauvaud, R. Maggiolo. Radiation belt electron precipitation due to vlf transmitters: Satellite oobservations. *Geophys. Res. Lett.*, 35, May 2008.

[11] W. J. Burke S. P. Kuo M. P. Sulzer R. J. Riddolls A. X. Zhang M. C. Lee, M. J. Starks. Whistler wave interactions with space plasmas during hf heating of the ionosphere at arecibo.

[12] H. H. Kuehl. Electromagnetic radition from an electric dipole in a cold anisotropic plasma. *Phys. Fluids*, 5:1095, September 1962.

[13] J. E. Bergeson D. P. GiaRusso. Studies of vlf radiation patterns of a dipole immersed in a slightly lossy magnetosphere. *Radio Science*, 5:745–756, April 1970.

[14] U. S. Inan T. F. Bell and T. Chevalier. Current distribution of a vlf electric dipole antenna in the plasmasphere. *Radio Sci.*, 41, 2006.

[15] John David Jackson.

[16] T. N. C. Wang and T. F. Bell. Radiation resistance of a short dipole immersed in a cold magnetoionic medium. *Radio Sci.*, 4:167–177, 1969.

[17] K. G. Balmain. The impedace of a short dipole antenna in a magnetoplasma. *IEEE Transactions on Antennas and Propagation*, 12:605–617, 1964.